AN ENERGY CONFINEMENT STUDY OF THE MST REVERSED FIELD PINCH

USING A THOMSON SCATTERING DIAGNOSTIC

BY

DANIEL JOHN DEN HARTOG

A thesis submitted in partial fulfillment of the

requirements for the degree of

DOCTOR OF PHILOSOPHY

(Physics)

at the

UNIVERSITY OF WISCONSIN-MADISON

1989



AN ENERGY CONFINEMENT STUDY OF THE MST REVERSED FIELD PINCH

USING A THOMSON SCATTERING DIAGNOSTIC

Daniel John Den Hartog

Under the supervision of Professor Richard N. Dexter

ABSTRACT

Thomson scattering measurements of the central electron temperature and density during the plasma current peak have been performed on the MST Reversed Field Pinch (RFP). This Thomson scattering diagnostic was calibrated for absolute electron density measurements. These measurements of $T_e$ and $n_e$, when combined with profile assumptions, were used to calculate estimates of energy confinement time ($\tau_E$) and poloidal beta ($\beta_\theta$). A standard discharge with $I_p \approx 400$ kA, $F \approx -0.1$, and $\theta \approx 1.6$ typically exhibited $T_e \approx 275$ eV, $n_e \approx 2.0 \times 10^{13}$ cm$^{-3}$, $\tau_E \leq 1$ ms, and $\beta_\theta \leq 8\%$. The results of a limited plasma current scaling study did not indicate a strong scaling of $T_e$ or $\tau_E$ with $I_p$.

The Thomson scattering diagnostic was used in conjunction with a bolometer, VUV radiation monitor, and edge magnetic coils to study the loss of energy from the plasma.

Results indicate that thermal transport from stochastic magnetic fields, particle loss, and radiation are important energy loss processes. The experiments done for this study included an F-scan, a paddle limiter insertion series, and an argon doping series. The plasma maintained a constant $\beta_\theta$ during these perturbation experiments, suggesting that increases in one energy loss channel are compensated by drops in other channels and increases in input power to the plasma.



## ACKNOWLEDGEMENTS

My advisor, Professor Richard Dexter has been a continual source of inspiration, insight, and encouragement. I have appreciated the opportunity to work and study as his student. I am especially grateful for his willingness to spend time discussing results, analyzing data, and solving problems.

I also wish to thank Professor Sam Hokin for his individual efforts toward the success of the Thomson scattering diagnostic. Thanks also to Professor Stewart Prager and Professor Clint Sprott for their willingness to answer questions and their support of this project. Thanks to Professor Jim Lawler for sharing his knowledge and loaning his equipment.

I have been, and continue to be, always thankful for the skill and dedication of the engineering and technical staff of this plasma physics group. The labors of Glenn Fleet, Don Holly, John Laufenberg, Tom Lovell, and Jim Morin have been instrumental in the success of MST and this diagnostic. Many hourly workers have contributed to this project; I would like to thank Mark Thomas in particular for ingenious solutions to electronic problems. Thanks also to Matt Dexter and Ammar Rabbat for help dealing with Athena and MDS. Thanks to Jon

Kranz for help navigating the pitfalls of purchasing and bureaucracy. I greatly appreciate the secretarial skills of Kay Shatrawka, whose efficiency and timeliness are matched only by her good cheer.

Many of my fellow graduate students have labored on my behalf and toward the success of this project. These fine people include Abdulgader Almagri, Saeed Assadi, Jeff Beckstead, George Chartas, and Weimin Shen. Thanks also to postdocs Dave Kortbawi, Trudy Rempel, and John Sarff. Krzysztof Melzacki did much of the initial design of this diagnostic while he was a postdoc here. Peter Brooker and Peter Trost were always willing to share their Thomson scattering knowledge and experience.

I have had many fruitful contacts with experienced Thomson scattering workers. J. Casey, R. Kindsfather (who loaned us a set of ruby filters), and M. Pickrell each shared their knowledge. The MST Thomson scattering system also has much in common with the system on Torus II developed by F.M. Levinton and G.A. Navratil.

The Physics Department has a marvelously capable Instrument Shop staff. Their skills and craftsmanship are evident in each piece of Thomson scattering equipment.



Particular thanks go to Vernon Herr, Mike Humphry, Lloyd Ochalla, and Ed Vasiukevicius. Throughout these years I have also benefited from the patient instruction of John Thompson and Art Fritsche in the Student Shop.

Finally, I express my deepest gratitude to my family and my wife Betsy. I have not lacked love and encouragement. Each day I am thankful for you and the special graces you possess. The fine hand-inked figures in this thesis were drawn by Betsy.

This work was financially supported by the U.S. Department of Energy.

"When I consider Thy heavens, the work of Thy fingers,
The moon and the stars, which Thou has ordained;
What is man, that Thou art mindful of him?
And the son of man, that Thou visitest him?
For Thou hast made him a little lower than the angels,
And hast crowned him with glory and honour.

"O Lord our Lord,
How excellent is Thy name in all the earth!"

Psalm 8:3-5,9 (KJV)

TABLE OF CONTENTS


| | Page |
|---|---|
| ABSTRACT | ii |
| ACKNOWLEDGEMENTS | iv |
| TABLE OF CONTENTS | vii |
| I. Introduction | 1 |
| A) The MST RFP | 2 |
| B) Purpose and goal of confinement studies | 3 |
| C) Purpose and use of the Thomson scattering diagnostic | 5 |
| D) The Poloidal Divertor RFP Thomson scattering diagnostic | 6 |
| 1) RFP electron temperature and density | 7 |
| a) $T_e$ and $n_e$ versus time | 7 |
| b) $T_e$ versus plasma current | 8 |
| 2) Non-reversed Pinch electron temperature and density | 9 |
| 3) Summary | 10 |
| E) PLP reports | 10 |
| II. Thomson Scattering Theory | 26 |
| A) Basic principles | 26 |
| 1) Thomson scattering from a low temperature plasma | 27 |
| 2) Thomson scattering from a high temperature plasma | 37 |
| B) Signal to noise ratio of the Thomson scattering diagnostic | 41 |





| | |
|---|---|
| III. Thomson Scattering Apparatus | 50 |
| A) Thomson scattering system | 50 |
| 1) Laser cart and detector platform | 50 |
| 2) Laser and focussing optics | 51 |
| 3) Beam dump and stray light reduction | 54 |
| 4) Collection optics | 56 |
| 5) Spectrograph and detector | 57 |
| 6) Data acquisition system | 60 |
| B) Alignment of Optical systems | 63 |
| C) Calibration of spectrograph and detector | 70 |
| D) Other diagnostics | 75 |
| 1) Bolometer | 75 |
| 2) VUV impurity radiation | 76 |
| 3) Plasma current | 77 |
| IV. Experimental Procedure | 88 |
| A) Data acquisition | 88 |
| B) Data reduction | 90 |
| C) Electron density calibration coefficient | 94 |
| V. Introduction to RFP confinement | 107 |
| A) Global parameters describing confinement | 107 |
| B) Anomalous resistivity of the RFP | 117 |
| C) Scaling of energy confinement time | 129 |

VI. The MST plasma 141

A) Electron temperature and density fluctuations 142

B) Experimental approach to energy confinement 150

C) F-scan experiment 153

D) Paddle insertion experiment 159

E) Argon doping experiment 168

F) MST scaling of confinement parameters 176

G) Summary of energy confinement observations 181

VII. Summary 273



# CHAPTER I: INTRODUCTION

The Madison Symmetric Torus (MST) is a toroidal reversed field pinch (RFP) device whose purpose is the magnetic confinement of high temperature plasmas. The RFP is characterized as a relaxed state system; many of the aspects of its configuration can be explained with the use of relaxation theory. The RFP is distinct from other toroidal magnetic confinement devices in that the magnitude of the poloidal ($B_\theta$) and toroidal ($B_\phi$) components of the magnetic field is comparable, and the toroidal component is reversed near the plasma edge. This reversed field equilibrium is thought to be a minimum energy state to which the plasma relaxes. Current belief is that this reversed field equilibrium is sustained against classical resistive diffusion by a "dynamo" mechanism. Complete reviews of these subjects can be found in references 1-4. It will be sufficient here to quote some of the theoretical and experimental results.

For a pressureless plasma with a small but finite resistivity, bounded by a perfectly conducting wall, there exists a set of minimum energy equilibrium states described by[1]

$$\underline{\nabla} \times \underline{B} = \lambda \underline{B} \qquad (I.1)$$

where $\lambda$ is constant. These states were obtained by constraining to invariance the total magnetic helicity, defined as

$$K = \int \underline{A} \cdot \underline{B} dV \quad . \qquad (I.2)$$

$\underline{A}$ is the magnetic vector potential. Integration is over the entire volume of the plasma. The solutions of Eq. (I.1) in a cylinder are $B_\phi = B_0 J_0(\lambda r)$, $B_\theta = B_0 J_1(\lambda r)$, $B_r = 0$, where $J_0$ and $J_1$ are Bessel functions and $\lambda = \underline{J} \cdot \underline{B}/B$. See Figure I.1 for graphs of these functions. The magnetic field equilibria in MST have not been measured, but the equilibria given by the above equations have been shown to fit the measured profiles of other RFP devices remarkably well, even in light of the fact that $\lambda$ is not constant but falls to zero at the boundary of the plasma.[4]

A) The MST RFP

Parameters of the MST RFP are listed in Table 1. The diagnostics that have become available since the MST commenced operation in June 1988 are listed in Table 2. The MST itself is shown in Figures I.2 and I.3. The MST is unusual in that the aluminum vacuum vessel acts as the



toroidal field winding coil and the stabilizing conducting shell (see Figure I.4).[5] Vacuum pumping is done through a manifold connected to the vacuum vessel by 193 1-1/2" diameter holes.

Great care was taken in the design of MST to minimize magnetic field errors. The pumping system and toroidal field system are examples of this care. The poloidal field system was not in final form during the time period this data was taken. The DC bias winding was used both to bias the iron core and to obtain the pulsed poloidal field (plasma current). See Figure I.5. This system was not optimized to minimize field errors during the pulse. Consequently, radial magnetic fields of 20-30% were measured at the poloidal gap.[6] These were partially corrected with some positive results, but their full effect on the plasma or performance of the MST is not known.

B) Purpose and goal of confinement studies

The RFP is a potential magnetic fusion plasma confinement system. The RFP configuration has a number of potentially advantageous characteristics. For example, the RFP is inherently a high $\beta$ (ratio of plasma pressure to magnetic pressure) device because it has a low toroidal field; the configuration is stable because it has a large magnetic shear. It may also be possible to ohmically heat

the plasma to ignition conditions. An RFP fusion reactor may be able to operate economically as a high fusion power density device. However, the operational parameters of current RFP devices are far from fusion plasma conditions. Therefore, if the RFP is going to be accepted as a viable fusion plasma confinement system, we must understand the mechanisms underlying its energy and particle confinement characteristics.

The RFP exhibits a number of interesting characteristics that directly influence its global energy confinement performance. First is the observation that the RFP operates with a plasma resistivity that is anomalously large compared to classical Spitzer resistivity. This observed resistivity may actually spring from at least two or more distinct mechanisms, the first being classical collisions which heat electrons and the second being energy lost through helicity dissipation or fluctuations which heat the ions and/or drive the "dynamo." (In a sentence, the dynamo is the process whereby a poloidal plasma current is sustained by means of a toroidal electric field.)[7] Second is the observation that the poloidal beta ($\beta_\theta$) appears to be nearly constant over a wide variety of operating conditions. Poloidal beta remains constant even as the radiative energy loss from the plasma is increased to the point that almost all the energy flowing out of the plasma is lost via radiation. Third is the recent



observation of energetic (not runaway) electrons at the edge of RFP plasmas. These may come directly from the center of the plasma and may be a dominant energy loss channel. In sum, then, it is obvious that much work has been done in this area and much more remains to be done. The relationship of the above observations and results from MST to the topic of energy confinement will be discussed in detail in Chapters V and VI.

C) Purpose and use of the Thomson scattering diagnostic

The MST ruby laser Thomson scattering diagnostic was used to measure the electron temperature and density at the center of the plasma. This diagnostic provided local measurements of these quantities with a spatial resolution of three centimeters and a temporal resolution of about 30 nanoseconds. The Thomson scattering cross-section is small ($\sigma_T = (\frac{8\pi}{3}) r_0^2$, where $r_0$ is the classical radius of the electron), making this diagnostic completely nonperturbative. However, this double-edged sword cuts two ways, making the Thomson scattered signal extremely difficult to pull out of the noise.

This diagnostic was capable of measuring electron temperatures between 10 and 1000 eV at densities down to $3.0 \times 10^{12}$ cm$^{-3}$. These measurements were used on a shot-to-shot basis to track the performance of the MST and

its response to perturbations. These quantities are also, of course, integral to the calculation of poloidal beta and energy confinement time. Typically, this diagnostic was used in close conjunction with soft x-ray and visible detectors, a bolometer, and a variety of magnetic coils and electrostatic probes. Baseline performance of the plasma was established, and then the plasma was perturbed in a controlled fashion, and changes in parameters monitored. In this way, one can hope to reduce the highly non-linear RFP to a system that can be understood piece by piece. The particular emphasis of these experiments was to broaden understanding of the factors influencing energy confinement in an RFP plasma.

D) The Poloidal Divertor RFP Thomson scattering diagnostic

The Thomson scattering diagnostic on MST is the current incarnation of a diagnostic that was originally developed and built for the Poloidal Divertor RFP. This diagnostic was somewhat primitive, yet the data it produced are convincing and useful. The results from this device are recorded in detail in PLP 1023[8] and PLP 1061.[9] A short summary of these results is presented below in order to facilitate comparison to MST and other RFP devices.

The Poloidal Divertor RFP was constructed by installing small cross-section divertor rings in the Levitated Octupole vacuum vessel. A typical RFP discharge consisted of a plasma



current peak of 130 KA, peak electron temperature of about 70 eV, peak line-averaged electron density of about $1 \times 10^{13}$ $cm^{-3}$, and aided toroidal field reversal of about one-millisecond duration. Central electron temperature and density were recorded before, during, and after toroidal field reversal (an experiment that has not yet been done on MST). The same two quantities were also recorded at the plasma current peak as the plasma current was stepwise increased from 130 to 200 kA. This same machine was also operated with tokamak-like field programming; central electron temperature and density data will be presented for this case also.

1) RFP electron temperature and density

a) $T_e$ and $n_e$ versus time

As can be seen from the graphs in Figures I.6 and I.7, the raw data for the plots of central electron temperature and density were gathered on three separate days. Machine operation was the 'standard RFP discharge'[8] mode during the time these data were taken. Each temperature point is an average of about five shots. The density is in arbitrary units because the diagnostic was not absolutely calibrated. The significance, if any, of the dip in $T_e$ between 2.0 and 3.0 milliseconds is unclear. The dip may not even exist; the uncertainties in $T_e$ do not allow a definitive statement.

The electron density versus time behavior exhibited in Figure I.7 is not unexpected. Other gas puff fueled RFP devices have seen high initial density which dropped and then stabilized during the reversal period.[3,10] However, it is puzzling that the central chord line-averaged density does not show that density drop.[11] Perhaps an increase in the density of the plasma outside the divertor separatrix accounts for the nearly flat line-averaged density trace. Note that as the central density dropped, the error bars on the temperature points increased, owing to the smaller number of scattered photons.

b) $T_e$ versus plasma current

The results of a scaling of RFP electron temperature versus plasma current are shown in Figure I.8. Further information on how this scaling run was conducted can be found in PLP 1023.[8]

If we assume a linear relationship between electron temperature and plasma current as is indicated by constant beta scaling (see Chapter V), then for the Poloidal Divertor RFP:

$$T_e(eV) = 0.46 * I_p(kA) \quad .$$

In other words, this means that the electron temperature



increased 1/2 eV each kA increase in plasma current. This compares well with other scaling studies.[12] Note that, as shown in Figures I.9 and I.10, this scaling set was done at nearly constant $I_p/n_e$ (which is directly proportional to $I_p/N$, where N is the line density). Constant beta scaling is only applicable if $I_p/N$ is held constant during the scaling set. Note also that the point at 180 kA is slightly above the scaling line and has a slightly increased $I_p/n_e$. The congruence of these two observations is predicted by constant beta scaling.

2) Non-reversed Pinch electron temperature and density

The Poloidal Divertor RFP could be operated in a 'tokamak-like' mode by changing the toroidal field programming. Differentiating this machine from a true tokamak is the fact that the toroidal and poloidal fields were roughly comparable in magnitude. See PLP 1023[8] for further information on this mode of operation.

The graph of 'tokamak-like' electron temperature versus time is shown in Figure I.11. Peak temperature is roughly equivalent to that measured in RFP discharges. The electron density versus time graph (Figure I.12) indicates a steady decline in density as the discharge progressed. This is indicative of the presumed poor confinement of this device.

3) Summary

The Poloidal Divertor RFP exhibited electron temperature and density behavior that is characteristic of the RFP. For comparison purposes, the $T_e$ and $n_e$ versus time experiment should be done on MST. Somewhat surprisingly, the Poloidal Divertor RFP showed stronger evidence of a linear scaling of $T_e$ and $I_p$ than MST does. (See Chapter V for these results from MST.) However, this apparent disagreement may be due to the fact that the Poloidal Divertor RFP current scan ended at 200 kA; $T_e$ may scale linearly with $I_p$ when MST is operated below 300 kA. At currents above 300 kA, $T_e$ may not scale with $I_p$ in MST. The reason for this is not known at this time.

E) PLP reports

PLP reports are informal reports circulated internally within the University of Wisconsin-Madison Plasma Physics Group. They are available upon request from:

Plasma Physics Department

University of Wisconsin-Madison

1150 University Avenue

Madison, WI 53706.



References

[1] J.B. Taylor, Rev. Mod. Physics 58, 741 (1986).

[2] H.A.B. Bodin and A.A. Newton, Nucl. Fusion 20, 1255 (1980).

[3] H.A.B. Bodin, Nucl. Instrum. and Methods 207, 1 (1983).

[4] H.A.B. Bodin, in "Proceedings of the International School of Plasma Physics," Varenna, 1987 (Società Italiana di Fisica, Bologna, 1988), Vol. I, p. 3.

[5] J.A. Beckstead, et al., Bull. Am. Phys. Soc. 33, 2065 (1988).

[6] A.F. Almagri, et al., 16th IEEE International Conference on Plasma Science (Buffalo, 1989), Poster 2P53.

[7] K.F. Schoenberg, R.W. Moses, and R.L. Hagenson, Phys. Fluids 27, 1671 (1984).

[8] D.J. Den Hartog and R.N. Dexter, University of Wisconsin-Madison PLP 1023 (1987).

[9] D.J. Den Hartog and R.N. Dexter, University of Wisconsin-Madison PLP 1061 (1989).

[10] H. Dreicer, Physica Scripta T2/2, 435 (1982).

[11] J.S. Sarff, et al., Nucl. Fusion 29, 104 (1989).

[12] B. Alper, S. Martini, and S. Ortolani, Nucl. Fusion 26, 1256 (1986).

TABLE 1 - MST PARAMETERS

| | |
|---|---|
| Major radius | $R = 1.5$ m |
| Minor radius | $a = 0.52$ m |
| Shell thickness | $t = 0.05$ m |
| Plasma current | $I_p \leq 500$ kA |
| Toroidal magnetic field | $B_\theta \leq 1200$ gauss |
| Electron temperature | $T_e \leq 400$ eV |
| Line-average density | $\bar{n}_e \leq 2 \times 10^{19}$ m$^{-3}$ |
| Base pressure | $4 \times 10^{-7}$ Torr |



TABLE 2 - MST DIAGNOSTICS

Global electrical characteristics monitored with coils and probes

Thomson scattering for $T_{eo}$ and $n_{eo}$

Monochromator for Doppler line broadening

Shot integrated bolometer

Microwave interferometer for $\bar{n}_e$

Soft x-ray detector arrays

Visible light detector arrays

Electrostatic probes

Magnetic probes

Fast ion gauge

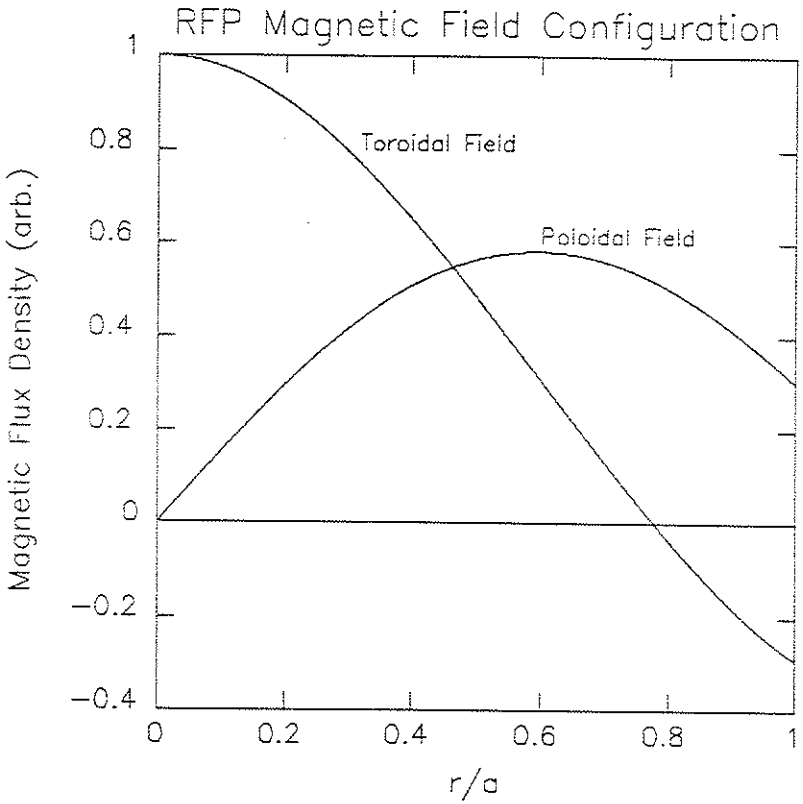


Figure I.1: Bessel function model (θ=1.55) of RFP magnetic field configuration.



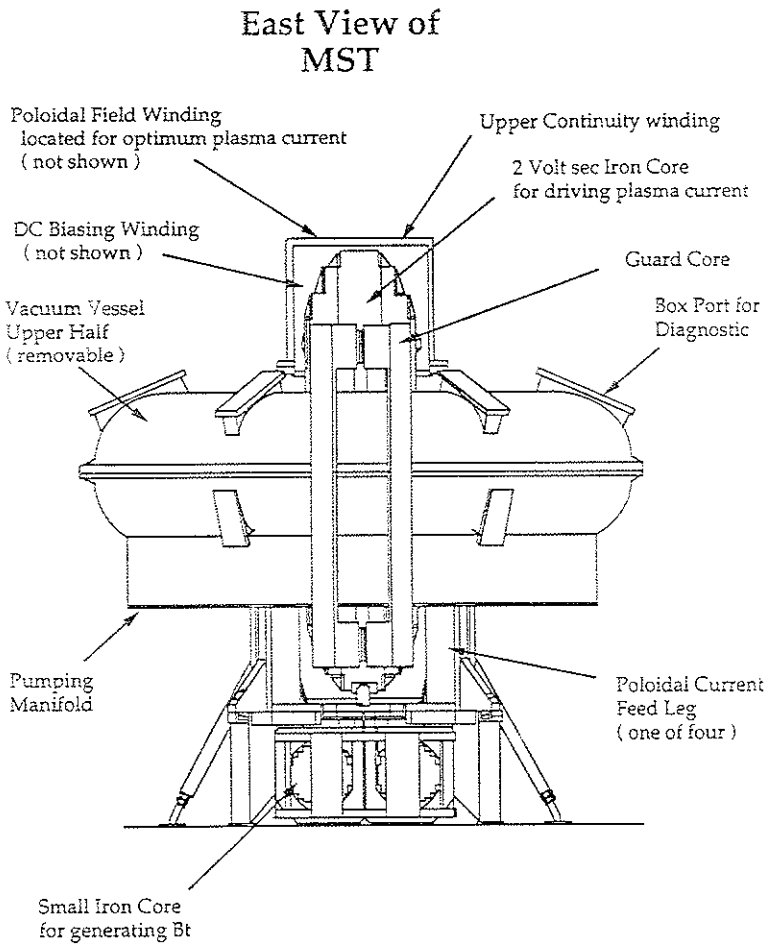


Figure I.2: The Madison Symmetric Torus. The guard core and poloidal field winding were not in place when data for this thesis were taken.

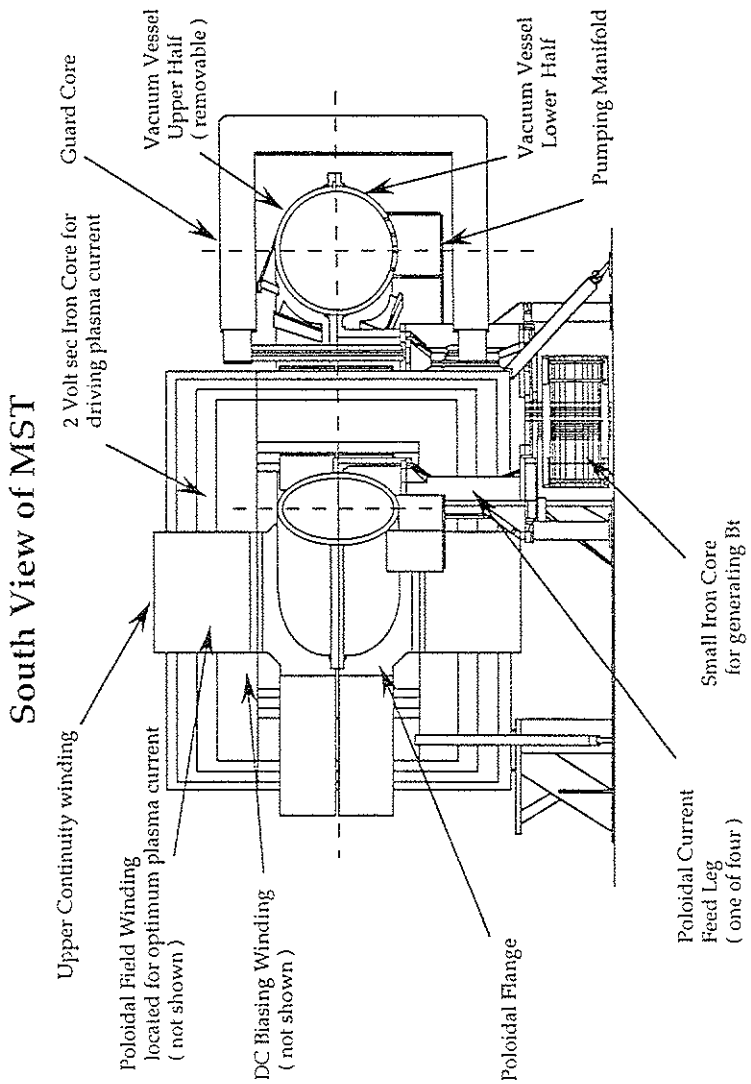


Figure I.3: The Madison Symmetric Torus. The guard core and poloidal field winding were not in place when data for this thesis were taken.



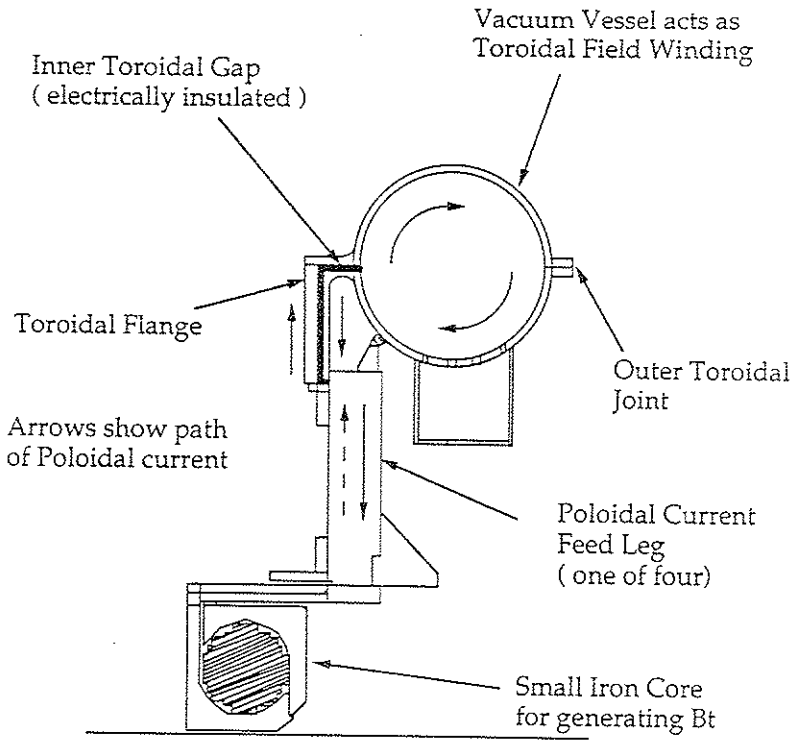


Figure I.4: The MST toroidal field system.

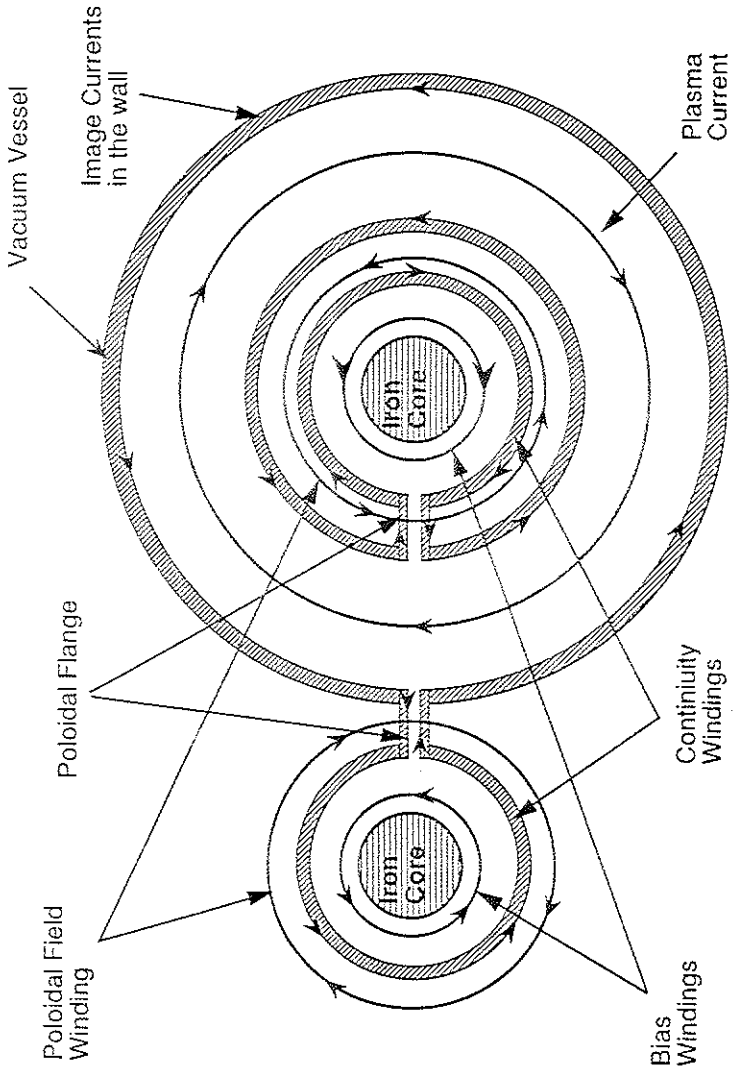


Figure I.5: The MST poloidal field system. The poloidal field windings were not in place when data for this thesis were taken.



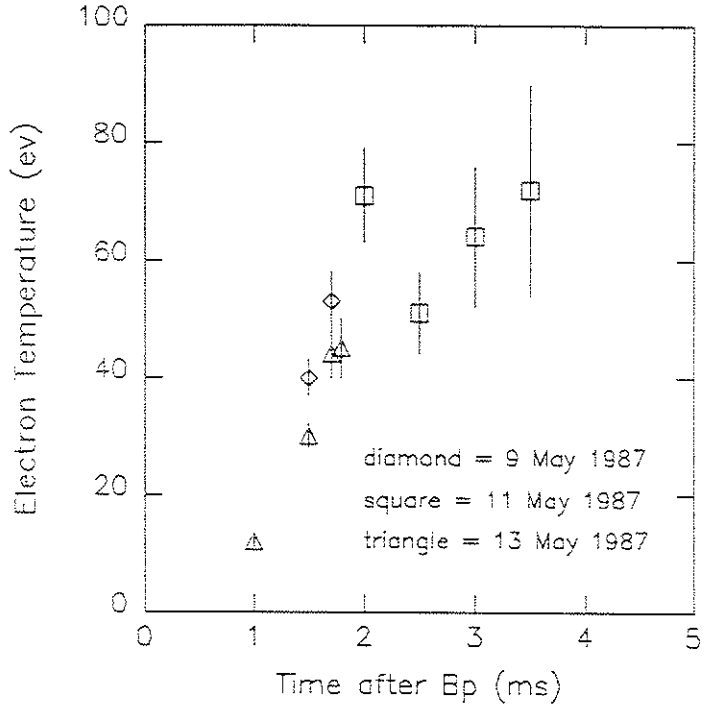


Figure I.6: Poloidal Divertor RFP central electron temperature versus time after initiation of discharge.

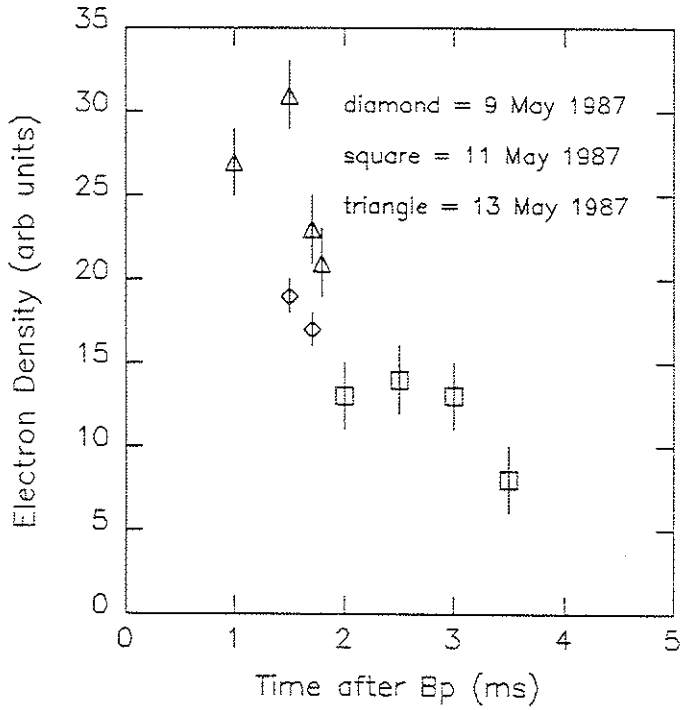


Figure I.7: Poloidal Divertor RFP central electron density versus time after initiation of discharge.



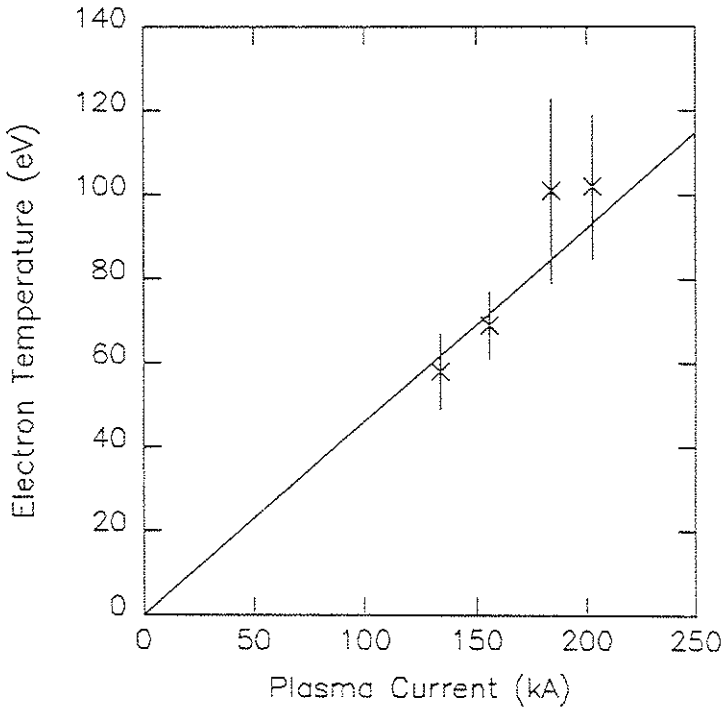


Figure I.8: Poloidal Divertor RFP central electron temperature versus plasma current (18 May 1987). The slope of the solid line is 0.46 eV/kA.

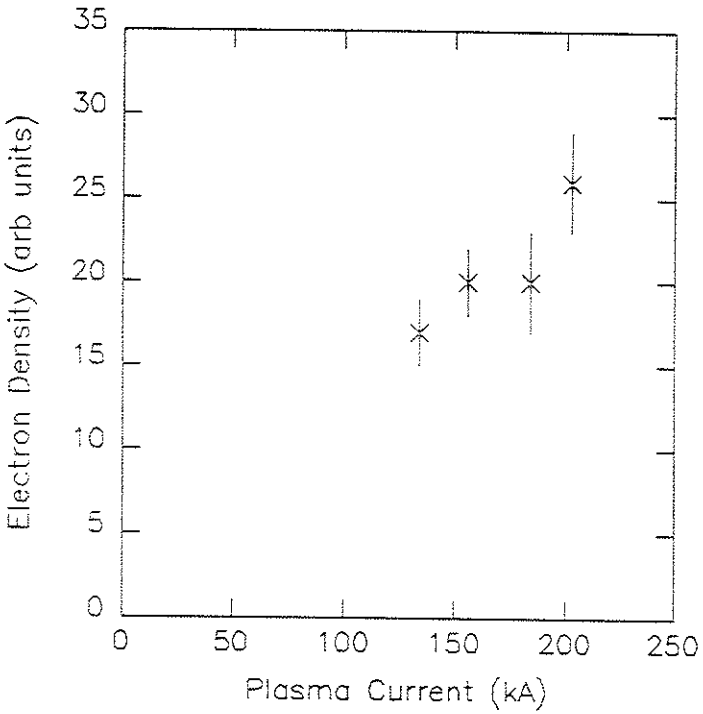


Figure I.9: Poloidal Divertor RFP central electron density versus plasma current (18 May 1987).



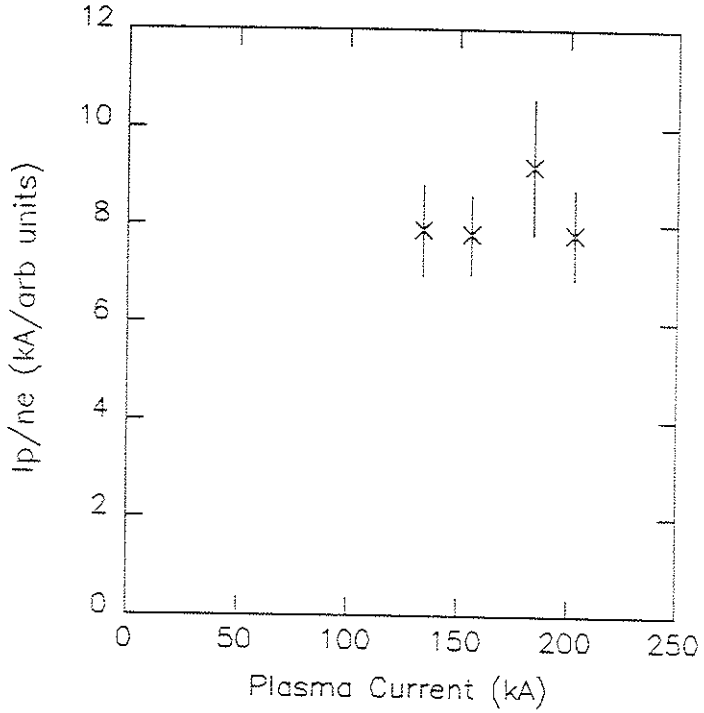


Figure I.10: Poloidal Divertor RFP $I_p/n_e$ versus plasma current (18 May 1987).

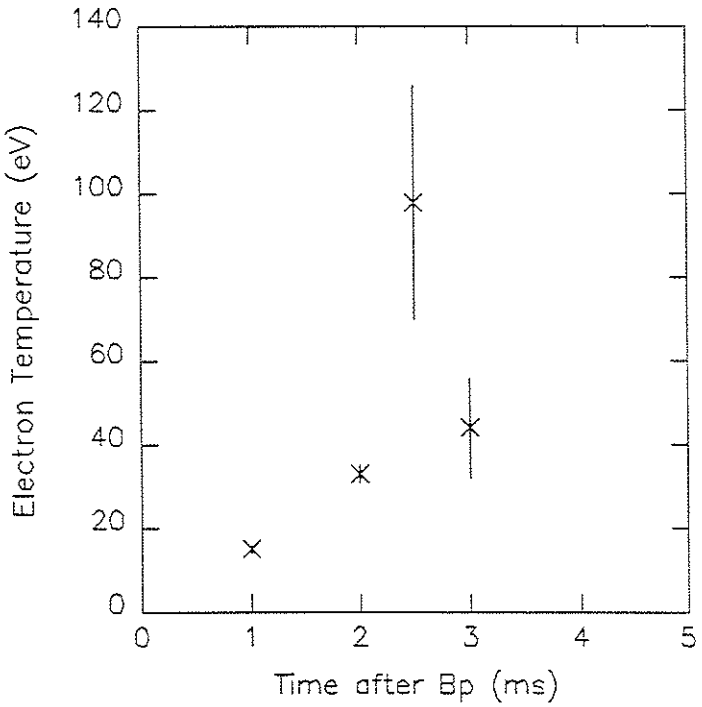


Figure I.11: 'Tokamak-like' central electron temperature versus time after initiation of discharge (14 May 1987).



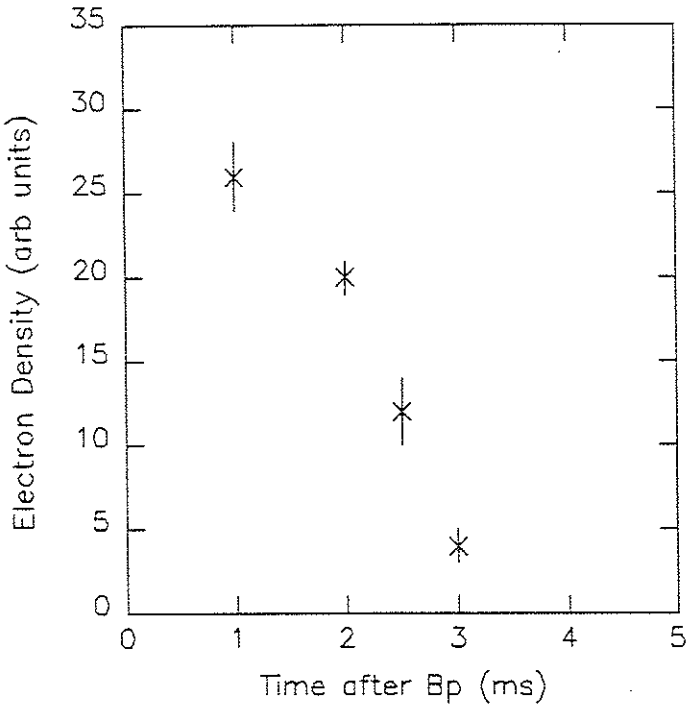


Figure I.12: 'Tokamak-like' central electron density versus time (14 May 1987).

## CHAPTER II: THOMSON SCATTERING THEORY

### A) Basic principles

Thomson scattering of electromagnetic radiation is simply the absorption and reradiation of a photon by a freely moving charge. The charge involved in the scattering process can be either an electron or an ion, although the Thomson scattering cross section for ions is much smaller than that for electrons. Most Thomson scattering diagnostics, including the one on the MST, are sensitive to electron scattered photons. Therefore, the rest of this section will concentrate on the dynamics of Thomson scattering of radiation by electrons.

If the electron involved in the scattering process is initially at rest, the Thomson scattered photon is of the same frequency as the incident photon. However, if the electron has an initial velocity, the scattered photon will be Doppler shifted in frequency. In particular, in a plasma the electrons have a distribution of velocities, usually assumed to be Maxwellian. The Thomson scattered spectrum reflects a Maxwellian distribution by appearing as a Gaussian profile centered on the laser line. The half-width of this



profile is directly related to the electron temperature, the area under the profile is related to the electron density.

#### 1) Thomson scattering from a low temperature plasma

This section is an attempt to put analytical flesh on the qualitative skeleton of the preceding two paragraphs. For the purposes of this discussion, a "low temperature plasma" is one with a $T_e$ less than 500 eV. This treatment follows that given by Sheffield;[1] other excellent references are Hutchinson,[2] McCool,[3] and Evans and Katzenstein.[4]

We must first determine what is meant by a "freely moving" electron in a plasma; we must specify the conditions for incoherent scattering. For incoherent scattering to occur, the "scattering wavelength" (defined by $\underline{k} = \underline{k}_s - \underline{k}_i$; more about this later) must be much smaller than the Debye length in the plasma. This is conveniently expressed by requiring that the parameter $\alpha = 1/k\lambda_D \ll 1$. If this is not the case then the incident wave interacts with groups of Debye shielded charges. The scattered spectrum then depends on the collective behavior of these groups and is no longer described by classical Thomson scattering. Sheffield[1] provides the formula

$$\alpha = \left(\frac{1.08 \times 10^{-11} \cdot \lambda_i(\text{nm})}{\sin(\theta/2)}\right)\left(\frac{n_e(\text{cm}^{-3})}{T_e(\text{eV})}\right)^{1/2} \qquad \text{(II.1)}$$

which uses an expression for the scattering wavelength $\lambda$ in terms of the incident wavelength $\lambda_i$ valid when $v_{th}/c \ll 1$. Typical parameters in the MST are $n_e = 1.5 \times 10^{13}/cm^3$ and $T_e = 300$ eV with $\lambda_i = 694.3$ nanometers and $\theta = 90^\circ$ (the scattering angle). This gives $\alpha = 0.0024$, well into the incoherent scattering regime.

The simplest way to begin to develop an understanding of Thomson scattering is to examine the scattering of radiation from a single free electron. Refer to Figure II.1. The incident wave is

$$\underline{E}_i(\underline{r},t) = \underline{E}_{io} \cos (\underline{k}_i \cdot \underline{r} - \omega_i t) \qquad \text{(II.2)}$$

$$\underline{B}_i(\underline{r},t) = \hat{i} \times \underline{E}_i \quad . \qquad \text{(II.3)}$$

When $v_j/c \ll 1$, the scattered electric field from the electron j is

$$\underline{E}_{sj}(\underline{R},t) = [e^2/c^2mR)(\hat{s} \times (\hat{s} \times \underline{E}_{io})]$$

$$\cos[\underline{k}_i \cdot \underline{r}_j(t_j') - \omega_i t_j'] \qquad \text{(II.4)}$$

where $t_j'$ is the retarded time and is given by

$$t_j' = t - (R - \hat{s} \cdot \underline{r}_j(t_j'))/c \qquad \text{(II.5)}$$



when $R \gg V^{1/3}$ where V is the scattering volume. In the derivation of Eq. (II.4) the assumptions are made that the incident electric field is the only force on the electron and that its orbit is unperturbed by the incident wave. Neither of these restrict application to electrons in the MST plasma; the magnetic field present in the MST can be ignored because the cyclotron frequency is much less than $\omega_i$ and, to first approximation, does not change the envelope of the scattered spectrum.[5] The condition of incoherent scattering insures that the plasma is collisionless over the scale length $V^{1/3}$. During the scattering process $\underline{v}_j$ is a constant and

$$\underline{r}_j(t_j') = \underline{r}_j(0) + \underline{v}_j t_j' \quad . \qquad \text{(II.6)}$$

Combination of these three equations gives

$$\underline{E}_{sj}(\underline{R},t) = (e^2/c^2mR)[\hat{s} \times (\hat{s} \times \underline{E}_{io})]$$

$$\cos[k_s R - \omega_s t - \underline{k} \cdot \underline{r}_j(0)] \qquad \text{(II.7)}$$

where

$$\omega_s = \omega_i + \omega = \omega_i + \underline{k} \cdot \underline{v}_j \qquad \text{(II.8)}$$

and

$$\underline{k} = \underline{k}_s - \underline{k}_i \qquad \text{(II.9)}$$

$$\underline{k}_s = (\omega_s/c)\hat{s} \qquad \text{(II.10)}$$

$$\underline{k}_i = (\omega_i/c)\hat{i} \quad . \qquad \text{(II.11)}$$

Refer to Figure II.2; the scattered frequency is Doppler-shifted by $\omega = \underline{k} \cdot \underline{v}_j$.

The Doppler shift occurring in the scattering process is much easier to understand if the problem is broken down into two parts. Assume a stationary source of radiation with wave vector $\underline{k}_i$. The first shift occurs when the electron "sees" the incident wave at the Doppler-shifted frequency $\omega' = \omega_i - \underline{k}_i \cdot \underline{v}_j$. The second comes about because the electron is moving with respect to the stationary observer. To make these statements quantitative, begin by combining Eq. (II.5) and Eq. (II.6):

$$t_j' = t - (R - \hat{s} \cdot (\underline{r}_j(0) + \underline{v}_j t_j'))/c \quad . \qquad \text{(II.12)}$$

Solve for $t_j'$:



$$t_j' = t/(1 - \hat{s} \cdot \underline{v}_j/c) -$$

$$[R - \hat{s} \cdot \underline{r}_j(0)]/[c(1 - \hat{s} \cdot \underline{v}_j/c)] \quad . \qquad \text{(II.13)}$$

The differential is

$$\Delta t_j' = \Delta t/(1 - \hat{s} \cdot \underline{v}_j/c) \quad . \qquad \text{(II.14)}$$

Inversion of this result gives the relationship between the frequency $\omega'$ radiated by the electron and the frequency $\omega_s$ received by the observer:

$$\omega_s = \omega'/(1 - \hat{s} \cdot \underline{v}_j/c) =$$

$$\omega_i(1 - \hat{i} \cdot \underline{v}_j/c)/(1 - \hat{s} \cdot \underline{v}_j/c) \quad . \qquad \text{(II.15)}$$

This is equivalent to

$$\omega_s - \underline{k}_s \cdot \underline{v}_j = \omega_i - \underline{k}_i \cdot \underline{v}_j \qquad \text{(II.16)}$$

or

$$\omega_s = \omega_i + \underline{k} \cdot \underline{v}_j \qquad \text{(II.17)}$$

where $\underline{k}$ is the "scattering vector" and is defined by $\underline{k} = \underline{k}_s - \underline{k}_i$.

The scattered intensity at $\underline{R}$ with frequency $\omega_s$ from the electron j is proportional to the time average of the scattered electric field squared. The scattered power within the solid angle $d\Omega$ at $\omega_s$ is[1]

$$P_{sj}(\underline{R},\omega_s)d\Omega = (P_i/A)r_o^2 d\Omega[\hat{s} \times (\hat{s} \times \hat{\underline{E}}_{io})_2 \qquad \text{(II.18)}$$

where the incident power is

$$P_i = c(E_{io}^2/8\pi)A \qquad \text{(II.19)}$$

and the classical electron radius is

$$r_o = e^2/mc^2 = 2.82 \times 10^{-13} \text{ cm} \quad . \qquad \text{(II.20)}$$

The element of solid angle $d\Omega$ is centered on the angle $\theta$ in the plane at angle $\phi_o$ to the incident electric vector $\underline{E}_{io}$. The cross-sectional area of the incident beam of radiation is A. For polarized radiation,

$$[\hat{s} \times (\hat{s} \times \underline{E}_{io})]^2 = 1 - \sin^2\theta \cos^2\phi_o \quad . \qquad \text{(II.21)}$$



Completion of this analysis requires extension of the single electron theory presented above to the distribution of electrons present in the plasma. The amount of scattered power in the frequency range $\omega_s$ to $\omega_s + d\omega_s$ is proportional to the number of electrons which have velocity $v_k = \underline{v} \cdot \underline{k}/k$ such that $\omega_s = \omega_i + v_k k$. The number of electrons in the scattering volume V in the range $\underline{v}$ to $\underline{v} + d\underline{v}$ is $Nf(\underline{v})d\underline{v}$ where

$$\int_{-\infty}^{\infty} f(\underline{v})d\underline{v} = 1 \qquad \text{(II.22)}$$

and N is the number of electrons in V. Thus, the total scattered power in $d\Omega$ in the direction $\hat{s}$ and in the frequency range $\omega_s$ to $\omega_s + d\omega_s$ is[1]

$$P_s(\underline{R},\omega_s)d\omega_s d\Omega = N(P_i/A)r_o^2 d\Omega[\hat{s} \times (\hat{s} \times \underline{E}_{io})]^2 d\omega_s$$

$$\iiint_{-\infty}^{\infty} dv_x dv_y dv_z f(\underline{v})\delta[(\omega_s - \omega_i) - \underline{k} \cdot \underline{v}] \quad . \qquad \text{(II.23)}$$

This result contains two assumptions. First, $f(\underline{v})$ cannot change during the laser pulse. Second, it is assumed that the same N charges remain within V during the laser pulse. This is not strictly true, but the correction may be neglected for a low temperature plasma.

For non-relativistic electrons in a plasma in thermodynamic equilibrium,

$$f(\underline{v}) = 1/(\pi a^2)^{3/2} \exp\{-(v_x^2 + v_y^2 \times v_z^2)/a^2\} \quad \text{(II.24)}$$

where $a = (2k_B T_e/m)^{1/2}$. This should be substituted into Eq. (II.23). The result can be presented in a number of ways, two of which are useful to experimentalists. Experimental results are often expressed in terms of the wavelength shift of the scattered radiation, $\Delta\lambda$, where $\lambda_s = \lambda_i + \Delta\lambda$. Because $a/c \ll 1$, it is appropriate to approximate

$$|\underline{k}| = \text{constant} = 2|\underline{k}_i| \sin(\theta/2) \quad . \quad \text{(II.25)}$$

Then the scattered power in the range $\lambda_s$ to $\lambda_s + d\lambda_s$ and in the solid angle $d\Omega$ is

$$P_s(\underline{R},\lambda_s)d\lambda_s d\Omega = \frac{P_i r_o^2 d\Omega n_e L}{2\sqrt{\pi}\sin(\theta/2)} [\hat{s} \times (\hat{s} \times \underline{E}_{io})]^2 (\frac{c}{a})$$

$$\exp\left(\frac{-c^2\Delta\lambda^2}{4a^2\lambda_i^2 \sin^2(\theta/2)}\right) \frac{d\lambda_s}{\lambda_i} \quad \text{(II.26)}$$

where L is the length of the scattering volume. The Gaussian



shape of the velocity distribution has been transformed into a Gaussian scattered power spectrum. Since the wavelength shift of the scattered radiation is small for a low temperature plasma, an expression for the time-averaged number of photons scattered per unit time in the range $\lambda_s$ to $\lambda_s + d\lambda_s$ and within $d\Omega$ can be written as

$$\frac{dN_p(\underline{R},\lambda_s)}{dt} d\lambda_s d\Omega = \frac{P_i r_o^2 d\Omega n_e L}{h\gamma_i \lambda_i^2 \sin^2(\theta/2)} [\hat{s} \times (\hat{s} \times \underline{E}_{io})]^2$$

$$(\frac{c}{a}) \exp\left(\frac{-c^2\Delta\lambda^2}{4a^2\lambda_i^2 \sin^2(\theta/2)}\right) \frac{d\lambda_s}{\lambda_i} \quad . \quad \text{(II.27)}$$

Of course, if the plasma is not in thermodynamic equilibrium then the above equations are not applicable. In fact, it is not, in theory, necessary to assume an *a priori* electron velocity distribution; inversion of the experimental Thomson scattered spectrum should define the velocity distribution. In practice, however, this is very difficult because the Thomson scattering cross section is extremely small. Only a few researchers have attempted to measure the velocity distribution with a Thomson scattering diagnostic.[6,7,8,9] The success of such endeavors is limited by the fact that every reasonable velocity distribution

differs strongly from a Maxwellian only in the high-energy tail. There are usually not enough electrons in the scattering volume to make the differences observable in the spectrum. The obverse of this situation is, of course, that it is almost always reasonable to assume a Maxwellian when analyzing Thomson scattering data.

As a final example to help illuminate the geometry of the Thomson scattering process, superimpose on the regular Maxwellian velocity distribution an electron drift velocity

$$v_o = (v_{ox}^2 + v_{oy}^2 + v_{oz}^2)^{1/2} \quad . \tag{II.28}$$

This produces the distribution

$$f(\underline{v}) = (\pi a^2)^{-3/2} \exp\{((v_x - v_{ox})^2 + (v_y - v_{oy})^2 + (v_z - v_{oz})^2)/a^2\} \quad . \tag{II.29}$$

With no loss in generality assume that

$$\underline{k}_i = (k_i/\sqrt{2})(\hat{x} - \hat{y}) \tag{II.30}$$

and

$$\underline{k}_s = (k_s/\sqrt{2})(\hat{x} + \hat{y}) \quad . \tag{II.31}$$



(This corresponds to the usual $90^o$ Thomson scattering arrangement.) These assumptions translate into $\underline{k} = k\hat{y}$ with $k = 2k_i \sin(\pi/4)$. Also, as in most experiments, make the polarization of the incident wave perpendicular to the plane formed by $\underline{k}_i$ and $\underline{k}_s$. Then, with the use of Eq. (II.23),

$$P_s(\omega_s)d\omega_s d\Omega = \frac{P_i r_o^2 d\Omega n_e L}{\sqrt{\pi}\, a} \left(\frac{d\omega_s}{k}\right) \exp\left\{\frac{-(\omega/k - v_{oy})^2}{a^2}\right\} \quad . \tag{II.32}$$

The scattered power spectrum for this particular experimental arrangement is affected by the drift $v_{oy}$ which is in the direction of $\underline{k}$. This result should have been expected; measurements taken at one particular combination of $\underline{k}_i$ and $\underline{k}_s$ measure the electron velocity distribution in only one direction.

2) Thomson scattering from a high temperature plasma

This section contains an examination of the effect that the relativistic electrons in the electron velocity distribution have on the Thomson scattered spectrum. The corrections are fairly small for $T_e$ under 500 eV, although they can have an impact on the experimental derivation of temperatures as low as 100 eV. Even in plasmas with $T_e = 100$ eV, $v_{th}/c = 0.025$. This means that many of the electrons in the tail of the velocity distribution function

are relativistic and violate the assumption that v/c << 1. These relativistic electrons affect the shape of the entire scattered spectrum, not just the wings.

The following derivation and examples are from Gondhalekar and Kronast[6] and Sheffield.[1] In the derivation of the low temperature results, the implicit assumption was made that the motion of a single free electron in the field of an incident electromagnetic wave could be approximated by

$$\frac{d}{dt}\underline{p} = m\frac{d}{dt}\underline{v} = e\underline{E}(t) \quad . \tag{II.33}$$

Completeness, however, requires the inclusion of the effect of the incident magnetic field and the dependance of the mass of the electron on its velocity:

$$\frac{d}{dt}\underline{p} = \frac{d}{dt}\left(\frac{m\underline{v}}{(1-(v/c)^2)^{1/2}}\right) = e(\underline{E}(t) + \frac{\underline{v}}{c} \times \underline{B}(t)) \quad . \tag{II.34}$$

The expression for the electric field of a wave scattered by one electron must then be modified from that given in Eq. II.4 to[1]



$$\underline{E}_s(\underline{R},t) = \frac{ve^2}{mc^2R}(1-\beta^2)^{1/2}$$

$$\left\{\frac{\hat{s} \times [(\hat{s}-\underline{\beta}) \times (\underline{E}_{io} + \underline{\beta} \times (\hat{i} \times \underline{E}_{io}) - \underline{\beta}(\underline{\beta} \cdot \underline{E}_{io}))}{(1-\hat{s}\cdot\underline{\beta})^3}\right\}$$

$$\cos(k_i r(t') - \omega_i t') \tag{II.35}$$

where $\underline{\beta} = \underline{v}/c$ and $\underline{r}(t')$ is again calculated ignoring the effect of the incident wave. If the electrons have a Maxwellian velocity distribution and $\underline{E}_{io}$ is perpendicular to the scattering plane, then[1]

$$P_s(\underline{R},\lambda_s)d\lambda_s d\Omega = \frac{P_i r_o^2 d\Omega n_e L}{2\sqrt{\pi}\sin(\theta/2)}$$

$$\left\{1 - \frac{3.5\Delta\lambda}{\lambda_i} + \frac{c^2\Delta\lambda^2}{4a^2\lambda_i^3\sin^2(\theta/2)}\right\} \cdot \frac{cd\lambda_s}{a\lambda_i}$$

$$\exp\left\{\frac{-c^2\Delta\lambda^2}{4a^2\lambda_i^2\sin^2(\theta/2)}\right\} \quad . \tag{II.36}$$

Implicit in this derivation is the fact that $|\underline{k}|$ is not

approximately constant for scattering from a high temperature plasma.

The extra terms in Eq. (II.36) shift the peak of the spectrum toward the short wavelength side of $\lambda_i$. The shift $\Delta\lambda_m$ of the peak can be obtained by taking the derivation of Eq. (II.36) and setting the derivative equal to zero. The result is[1]

$$\Delta\lambda_m = -(7a^2 \sin^2(\theta/2)/c^2)\lambda_i$$

$$= -2.8 \times 10^{-5} T_e(eV) \sin^2(\theta/2)\lambda_i \quad . \qquad (II.37)$$

For $\theta = 90^\circ$, $T_e = 300$ eV and $\lambda_i = 694.3$ nm, $\Delta\lambda_m = 2.9$ nm. This is a substantial shift and is subject to misinterpretation unless relativistic effects are taken into account in the analysis of Thomson scattering data. To first order, this shift in the peak of the spectrum has the same form as the shift caused by an anisotropic electron drift velocity added to the velocity distribution function (see Eq. (II.32).

There is one other pitfall awaiting the experimentalist unaware of relativistic corrections to the scattered spectrum. On the MST, as is done elsewhere, only one-half of the Thomson scattered spectrum is collected by the detector. If the relativistic shift of the spectrum is not taken into account, interpretation of the data is done under the assumption that the spectrum is a Gaussian symmetric about $\Delta\lambda = 0$. Subsequent deduction of the temperature from the half-width of the Gaussian fitted to the data underestimates the temperature if only the long wavelength side of the spectrum has been collected, and vice versa. The errors that are engendered by such an incorrect analysis of raw data are not insubstantial. The errors range in size from a few percent at 100 eV to greater than 10% at 1 keV.[1] The range of temperatures encountered in the MST justify a relativistic analysis of the Thomson scattered data.



B) Signal to noise ratio of the Thomson scattering diagnostic

The Thomson scattering cross section is small. In order to ascertain the demands on the experimental apparatus, it is useful to calculate the number of photons that should appear in each channel of the spectrograph. This calculation follows that done by Freese, et al.[10] Eq. (II.38) below is an analog of Eq. (II.27).

The number of scattered photons in the range $\lambda_s \to \lambda_s + d\lambda_s$ and in the solid angle $d\Omega$ is

$$N_p(\lambda_s)d\Omega d\lambda_s = \frac{N_I n_e r_o^2 L d\Omega d\lambda_s}{\lambda_i \delta\sqrt{\pi}} \exp\left\{-\frac{(\lambda_s-\lambda_i)^2}{\lambda_i^2\delta^2}\right\} \qquad (II.38)$$

where

$N_I$ = number of incident photons

$n_e$ = electron density

$r_o$ = classical electron radius = $2.82 \times 10^{-15}$ m

L = length of scattering volume observed

$\Omega$ = observation solid angle

$\lambda_i$, $\lambda_s$ = incident and scattered wavelengths

$\delta = [8k_B T_e/mc^2]^{1/2} \sin(\theta/2)$

$k_B$ = Boltzmann's constant

$T_e$ = electron temperature

m = electron mass

c = speed of light

$\theta$ = angle between incident and scattered photons.

The number of photoelectrons produced at each channel of a multichannel spectrograph can be estimated as

$$N_{pe} = N_p \eta T(\lambda_{ch}) \Delta w \Delta\Omega \qquad \text{(II.39)}$$

where



$\lambda_{ch}$ = mean wavelength of channel

$\eta$ = quantum efficiency of detector

$T(\lambda_{ch})$ = spectral transmission function of the optical train at $\lambda_{ch}$

$\Delta w$ = spectral width of channel

$\Delta\Omega$ = observation solid angle

In our experiment we observed roughly the following condition:

$n_e = 1.5 \times 10^{13}$ cm$^{-3}$

$T_e$ = 300 eV

L = 0.032 m

$\theta_s = 90^o$

$\Delta\Omega$ = 0.0060 sr

$\Delta w$ = dependent on channel

$\eta$ = 0.065

$N_I = 1.75 \times 10^{19}$ (5J)

$\delta = 4.85 \times 10^{-2}$

The transmission function T is in general dependent upon the wavelength of the light passing through the optical system. Since the transmission function is difficult to estimate, it is usually directly measured. We were not able to measure it, so we must rely on a rough estimate that is assumed to be independent of wavelength. The following table illustrated the sources of loss within the system.

| Optical Component | Transmission |
|---|---|
| Two coated glass surfaces | $0.99^2$ |
| Two uncoated glass surfaces | $0.96^2$ |
| Three mirror surfaces | $0.85^3$ |
| Polarizer | 0.80 |
| Grating efficiency | 0.70 |
| PMT surface | 0.96 |
| TOTAL TRANSMISSION | 0.30 |

Carrying out the calculation of Eq. (II.39) gives

$$N_{pe}(\lambda_{ch},\Delta w) = 131\ \Delta w(\text{nm})\ \exp\left[-\frac{(\lambda_{ch} - \lambda_i)^2}{(33.6\ \text{nm})^2}\right] \quad . \text{(II.40)}$$

When the expression is applied to the channel central wavelengths $\lambda_{ch}$ and channel widths $\Delta w$ applicable to the MST Thomson scattering diagnostic, the following results are obtained.



| Ch# | $\lambda_{ch}$(nm) | $\Delta w$(nm) | Expected Photoelectron Count |
|---|---|---|---|
| 1 | 704.9 | 5.2 | 617 |
| 2 | 712.0 | 9.0 | 893 |
| 3 | 721.0 | 9.0 | 627 |
| 4 | 730.0 | 8.9 | 377 |
| 5 | 742.2 | 15.5 | 266 |
| TOTAL NUMBER OF PHOTOELECTRONS | | | 2780 |

The actual number of photoelectrons collected during a typical shot (see Figure II.3) is

| Ch# | $\lambda_{ch}$(nm) | $\Delta\lambda$(nm) | Actual Photoelectron Count |
|---|---|---|---|
| 1 | 704.9 | 5.2 | 67 |
| 2 | 712.0 | 9.0 | 112 |
| 3 | 721.0 | 9.0 | 65 |
| 4 | 730.0 | 8.9 | 29 |
| 5 | 742.2 | 15.5 | 37 |
| TOTAL NUMBER OF PHOTOELECTRONS | | | 310 |

The actual photoelectron count is about an order of magnitude less than the expected photoelectron count. The figures in the actual photoelectron count have not been normalized for channel efficiencies, but this would not markedly change the comparison. This situation will be discussed in more detail in Chapter IV.

## References


[1] J. Sheffield, Plasma Scattering of Electromagnetic Radiation, (Academic Press, New York, 1975).

[2] I.H. Hutchinson, Principles of Plasma Diagnostics, (Cambridge University Press, Cambridge, 1987).

[3] S.C. McCool, "Thomson Scattering on the Pretext Tokamak," Ph.D. Thesis, University of Texas at Austin (1982).

[4] D.E. Evans and J. Katzenstein, Rep. Prog. Phys. 32, 207 (1969).

[5] T.S. Brown and D.J. Rose, J. Appl. Phys. 37, 2709 (1966).

[6] A.M. Gondhalekar and B. Kronast, Phys. Rev. A 8, 441 (1973).

[7] H. Ringler and R.A. Nodwell, Phys. Letters 29A, 151 (1969).

[8] D.E. Evans, M.J. Forrest, and J. Katzenstein, Nature 221, 23 (1966).

[9] K. Hayase and T. Okuda, J. Phys. Soc. Japan 30, 1768 (1971).

[10] K.B. Freese, R.S. Massey, Rita Gribble, and J.D. Smith, SPIE 288, 280 (1981).




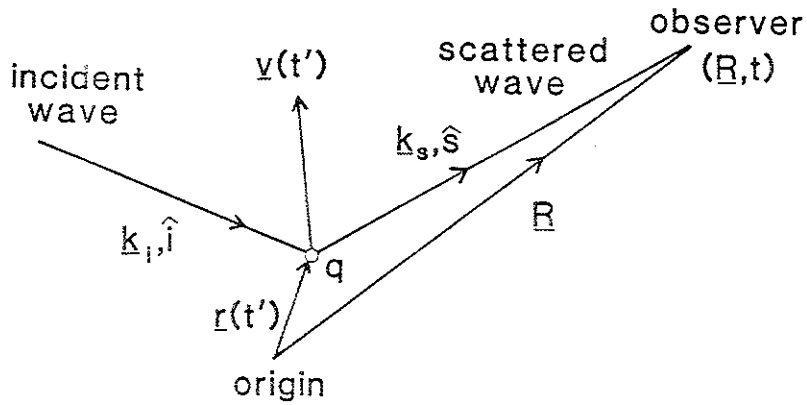


Figure II.1: The Thomson scattering coordinate system.[1]

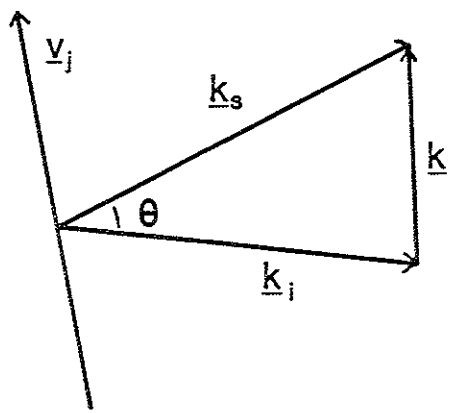


Figure II.2: Wavevector diagram.[1]



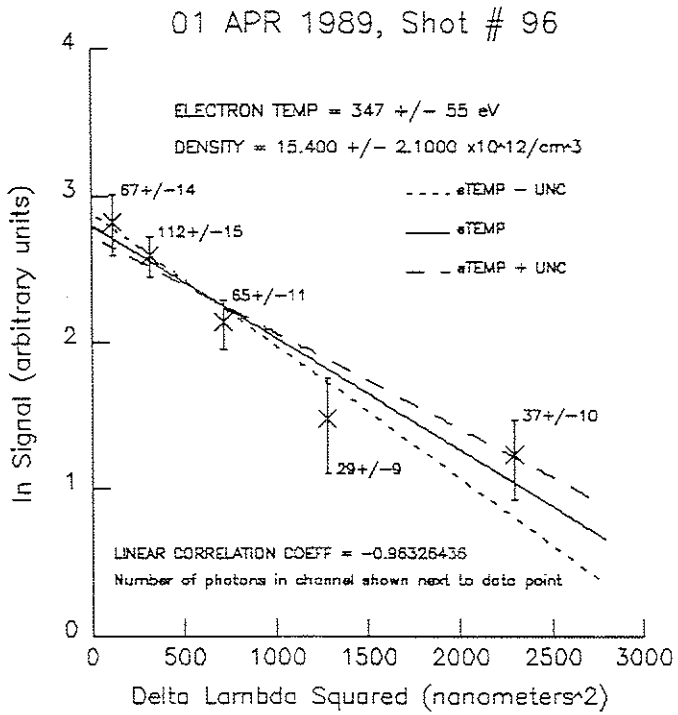


Figure II.3: Thomson scattering data from a typical shot.

# CHAPTER III: THOMSON SCATTERING APPARATUS

Much of the equipment for this Thomson scattering system was designed and constructed within the UW-Madison Physics Department. Many of the pieces were "made to order" and are unique to this device. This device is not, however, an original creation. Many of the design principles originated elsewhere; when possible, credit will be given to the source.

The Thomson scattering diagnostic is a system of distinct components. The relation of each component to the whole is depicted schematically in Figure III.1. Reference to this diagram will facilitate comprehension of the material below.

## A)Thomson scattering system

### 1) Laser cart and detector platform

Most of the Thomson scattering equipment was mounted on a specially constructed portable aluminum cart. Notice that the cart and detector platform are a single mechanical structure; the laser system and detection system were coupled by this rigid structure. Neither the cart nor the detector platforms were directly coupled to the vacuum vessel. The cart was rolled up to the side of the vacuum vessel and fixed in place with leveling jacks and feet mounted on neoprene



damping pads. This aspect of portability and adaptability has proved to be important as MST has evolved (and is evolving).

The laser and most of the laser beam input optics are mounted on the top shelf of the cart. The lower shelves and floor of the cart hold the laser power supply, cooling system, and control unit. Both the cart and detector platform were covered by sets of easily-removable and light-tight 1/16" aluminum panels. The purpose of these panels was two-fold. First, they enhanced the safety of personnel working in the range of a high-power laser. Second, they cut down on the amount of radio-frequency noise reaching the detector electronics.

The flexibility of the cart and platform system is advantageous. The height of the cart and platform are independently adjustable. The position of each component within the system can be adjusted and then firmly clamped down. And, when the need arises, disassembly and removal of the system from the MST area is relatively easy.

### 2) Laser and focusing optics

The Q-switched ruby laser system was manufactured by JK Lasers. The rods are linear flashlamp pumped. The system contains an oscillator rod and one amplifier rod.

Q-switching is done with a Pockels cell. The specifications of the ruby laser are

| | |
|---|---|
| Wavelength | 694.3 nm |
| Maximum output energy | 10 Joules |
| Output beam diameter | 16 mm |
| Pulse duration (FWHM) | 30 ns |
| Polarization | Horizontal |
| Beam divergence | 90% within 1.2 mR |

The straight-through configuration of the laser head allowed a HeNe alignment laser to be mounted such that its beam is coincident with the ruby laser beam.

As can be seen in Figure III.1, the ruby laser beam entered the vacuum vessel 22$^{o}$ below the horizontal split of the toroid. (The Thomson scattering system is 90$^{o}$ toroidally from the poloidal gap of MST.) For most of the experiments described in this thesis, the laser beam was focused such that the waist (the point from which the scattered light is collected) was at the estimated position of the plasma current axis. The position of the beam waist may, in the future, be scanned across the diameter of the vacuum vessel.

The laser beam, immediately after exiting the laser, passes through a 16 millimeter diameter aperture. This aperture removes stray and rapidly diverging light that might



otherwise inadvertently bounce into the collection optics. The beam is then folded back into the reversed Galilean collimator by a kinematically mounted mirror. The collimator, shown in Figure III.2, produces a scattering volume that is matched onto the entrance slit of the spectrograph by the collection optics. The collimator lenses are mounted such that the plane of the lens is slightly off perpendicular to the optical axis. This prevents potentially damaging back reflection of the beam into the laser. The position of each lens is x, y, and z adjustable since each is rod mounted on its own translation stage that moves perpendicular to the shared optical rail. The optical rail runs parallel to the optical axis.

The laser beam, once through the collimator, passes into the vacuum vessel through an input window. The input window is mounted on a valve and is 10$^{o}$ off perpendicular to the laser beam. All of the optical elements in the laser beam delivery system are UV grade fused silica and "V-line" anti-reflection coated to minimize reflection at the ruby laser wavelength. The optics in the laser beam line have high-power coatings and are very expensive. The optical surfaces are checked for dust daily and are cleaned only with a puff from the "dust-off" can of high-purity freon. In addition, HEPA filtered air flows into the laser and beam optics enclosure. The enclosure is kept at a slight positive

pressure in order to prevent dust from migrating into the enclosure.

3) Beam dump and stray light reduction

The beam diverging from the waist at the scattering volume must be efficiently dumped. At most, only $10^5$ of the $10^{19}$ photons in the laser beam are Thomson scattered into the collection optics. The rest of the photons must be dumped, otherwise they will overwhelm the rejection of the spectrograph and bury the Thomson scattered signal in the noise.

The most important element of the stray light reduction system is the laser beam dump, shown in Figure III.3. This dump is similar to the one installed on TNT-A.[1] The ruby laser beam coming into the dump is horizontally polarized. It strikes the first set of absorptive blue and green filter glasses at Brewster's angle. The small reflected beam is absorbed by the second piece of filter glass and the razor blade dump. This design is extremely compact and robust, having survived thousands of high power shots without visible damage.

As the laser beam exits the vacuum vessel it passes through an aperture beam dump that picks off the widely diverging rays of the beam that are created by imperfections in the input optics and are not absorbed by the main beam



dump. This aperture beam dump consists of an annular opening through which the laser beam passes. The annulus is surrounded by closely spaced V-grooves cut into an aluminum substrate. The peaks of the grooves are sharp edges separated by about 1.6 mm. The grooves are approximately 3.2 mm deep. The exposed aluminum surfaces of this dump and the main beam dump are coated with a layer of black graphite applied in an isopropyl alcohol solution.

The other important stray light reduction component is the viewing dump mounted opposite the collection lens in the vacuum vessel. There are two sources of stray light in the vacuum vessel. The first, and overwhelming, source is simply laser line light that has, for some reason, diverged from the main beam path far enough to end up bouncing around inside the reflective walls of the vacuum vessel. The second source is Thomson scattering that occurs outside of the scattering volume at the beam waist. This light is not very harmful, but should be prevented from entering the collection optics in order to preserve the spatial resolution of the diagnostic. In either case, this stray light can only enter the collection optics by bouncing into the collection solid angle. It can only do this by bouncing off the equivalent area of wall exactly opposite the collection port. The viewing dump covers this area and absorbs most of the light that hits it. The viewing dump itself is simply a set of

integrated circuit cooling blocks mounted on the wall of the VCV. The blocks are black anodized aluminum and consist of 4 mm high vertical fins spaced 3 mm apart. This viewing dump is close enough to the wall that it doesn't interact with the plasma, yet is cheap and fairly efficient.

4) Collection optics

The system of collection optics is shown in Figure III.1. The collection lens has a focal length of 200 mm and a clear aperture of 67 mm. It was ground from BK-7 glass and "V-line" coated at 694.3 nm. The collection lens focuses the approximately 1.0 x 32.0 mm cylindrical scattering volume on the 0.5 x 16.0 mm entrance slit of the spectrograph. This magnification of one-half is achieved with an object distance of 636 mm and an image distance of 292 mm.

The collection lens is mounted in a flange which is bolted to the boxport on MST. The lens forms the vacuum seal and looks at the scattering volume through a 50 mm diameter hole in the vacuum vessel. This is the aperture that limits the solid angle of the collection optics to 0.0060 steradians; if the diameter of the collection lens were the limiting factor the solid angle would be 0.0087 steradians.

Although not shown in Figure III.1, provision has been made to mount a set of eight collection lenses in the boxport flange. These will look through the eight 50 mm holes in the



vacuum vessel and may be used to obtain future radial scans of electron temperature and density. With the presently available equipment, such scans would have to be done position by position. This would require full realignment of the optics at each position and would be very tedious.

There are some other elements in the collection system. The front-silvered mirror rotates and is height adjustable. The polarizer is a high quality dichroic sheet. It transmits the horizontally polarized Thomson scattered light and blocks half the randomly polarized background light ("noise") from the plasma. The RG-645 color filter passes wavelengths longer than 690 nm. This is the side of the Thomson scattered spectrum that is collected. The short wavelength side of the spectrum is rejected because it contains the hydrogen alpha line at 656 nm.

5) Spectrograph and detector

The Jarrel-Ash MonoSpec 27 spectrograph is pictured in Figure III.4. It is of the cross Czerny-Turner design and has a 275 mm focal length. The throughput is effectively f/4.4 in the wavelength range of the Thomson scattered light. This matches the f/4.4 of the collection optical system. A 1200 g/mm classically ruled grating with a blaze wavelength of 500 nm has been used for all data taken on MST up to this point.

The detector at the exit plane of the spectrograph is an ITT F4149 microchannel plate PMT and has the following characteristics:

| | |
|---|---|
| Response time: | ~1 ns |
| Photocathode type: | MA-4 |
| Photocathode quantum efficiency: | ~6.5% @700 nm |
| Nominal gain: | $7 \times 10^5$ @2300 V |
| Anode configuration: | 10x10 multiple anode array |

The photocathode of the MCP PMT is coincident with the exit plane of the spectrograph. The photoelectrons from the photocathode cascade down the microchannel plates (this is where the electron gain occurs) and are collected at the output anode array. The 10 x 10 anode array on the MCP PMT is wired such that it consists of one vertical row of ten anode pins, three vertical rows of twenty anode pins each, and one vertical row of thirty anode pins. The Thomson scattered spectrum is imaged by these five bands of pins ("channels").

This particular pin configuration was chosen for a number of reasons. The digitizer limit is six channels. Computer simulations of various band configurations (the simulations are described in detail in PLP 1023[2]) suggested that the one chosen leads to the truest and most robust



reconstruction of the scattered spectrum. This is the case for this configuration largely because each channel ends up collecting a roughly equivalent number of photons (see Chapter II). This helps to insure that each section of the spectrum is fairly well defined.

The MCP PMT is mounted in a brass electrostatic shield. The electrostatic shield is the piece that is actually bolted to the exit flange of spectrograph. Electrical isolation between the shield and the spectrograph is guaranteed by a viton gasket. Grounding protocol requires that the detection system be at computer ground. The laser, cart, and spectrograph are held at machine ground by a single strap connected directly from the cart to the vacuum vessel. This grounding configuration minimizes inductive noise that occurs when the MST magnetic fields are pulsed.

The MCP PMT is powered by a gateable power supply built in-house. The design of this power supply was based on one designed for the Thomson scattering system on the Tara tandem mirror.[3] This power supply performs a number of functions. It provides the high voltage for the MCP assembly. This high voltage is continuously on while the diagnostic is in operation. The photocathode is normally biased 33 volts positive with respect to the entrance of the microchannel plates; this rejects light from the plasma that would saturate the MCP. The MCP PMT is gated on by swinging the

photocathode 133 volts negative with respect to the entrance of the MCP. The gateable power supply does this in less than 100 nanoseconds, although the MCP PMT requires a few microseconds to stabilize after being gated on. Finally, the power supply also provides the 100 volts necessary between the exit of the microchannel plates and anode pins. The anode pins remain close to ground through 50 ohms.

6) Data acquisition system

The equipment and interconnections in the data acquisition system are shown in Figure III.5. This is a complex system; in order to facilitate understanding a time line detailing the progression of pulses and data through the system is shown in Figure III.6. The explanation below will follow this same chronological progression.

The main timing panel module provides the initial trigger pulse. This module is part of the sequence of pulsers that control all MST operations. The module delivers a pulse to the laser 1.25 ms before the laser actually fires. During this time interval the flashlamps pump the ruby rods. When the rods have reached a population inversion, the internal timing circuitry of the laser produces a pulse that opens the Pockels cell. This produces a Q-switched pulse of 30 ns FWHM which proceeds to travel through the optical



train. The laser timing circuitry also produces a 15 μs Pockels cell sync pulse.

The leading edge of the Pockels cell sync pulse triggers the MCP PMT gate section of the Thomson scattering timing box. After a delay of 2.8 μs, this box begins a 2.5 μs MCP PMT photocathode gate pulse. This gate pulse travels to the MCP gateable power supply which gates the MCP PMT on as described in the previous section. The MCP PMT needs about 2 μs to stabilize before it is ready to receive the Thomson scattered photons.

The above sequence of gate pulses happens on a relatively slow time scale. A much faster timing sequence is required to control the digitizer that records the Thomson scattering data. This sequence begins at the fast photodiode output of the ruby laser. The laser optical train contains a picosecond rise time photodiode that follows the shape of the laser light pulse. The photodiode pulse triggers the digitizer gate section of the Thomson scattering timing box. This produced a 100 ns wide digitizer gate that begins before the pulse of Thomson scattered data reaches the digitizer. Initial synchronization of these events was done by the "cut and try" method. The pulse of Thomson scattered data reaches the digitizer approximately 80 ns behind the fast photodiode output. The approximately 40 ns delay between the fast

photodiode pulse and beginning of the digitizer gate is achieved with the following components:

23 ns of RG-58 coaxial cable between the photodiode output and the time box

10 ns intrinsic delay in the timing box

8 ns of RG-58 coaxial cable between the timing box and the digitizer.

The digitizer is ready to receive data 2 ns after the leading edge of the digitizer gate pulse.

The data from a spectrograph wavelength channel reaches the digitizer in the following manner. The photons registered at the photocathode of the MCP PMT produce a pulse of current at the anode pins of the MCP PMT. This pulse of current follows the shape of the laser pulse. The current pulse flows through about 1 meter of coaxial cable and into the 50 ohm input of the voltage amplifier. This low impedance input keeps the anode pins of the MCP PMT near ground; this is essential for proper operation of the MCP PMT. The amplifier drives the pulse through about 9 meters of coaxial cable to the 50 MHz low pass filter on the input of the time-delay box. This filter removes the 80 MHz Pockels cell switching noise that the MCP PMT picks up. The bandwidth of this passive filter is wide enough to pass the current pulse containing the data without distortion. Ignore



the delay line for the moment. The current pulse moves from the filter to the digitizer input through about 2 meters of coaxial cable. The digitizer integrates the current pulse and produces a number of counts proportional to the amount of charge that has flowed into its input. The gain of the MCP PMT and amplifiers has been adjusted so that one photon is approximately three-quarters of digitizer count (the measurement of this conversion factor will be described later in this chapter).

Return to the delay line that follows the 50 MHZ filter. This delay line is a coil of 25 meters of RG-58 coaxial cable. The effect of this delay line is to pass the plasma background light which preceded the pulse of Thomson scattered photons into the digitizer when it is gated on to accept the Thomson scattered data pulse. The plasma background light can then be subtracted from the light collected during the Thomson scattered data pulse. The signal remaining after this subtraction is Thomson scattered light.

B) Alignment of optical systems

The key to a functional Thomson scattering diagnostic is successful alignment of the optical systems. Alignment of this system is a craft that is best learned by experience. This section contains an outline of the procedures used to

align the laser focusing system and the collection optics. Note how tedious and time-consuming it would be to repeat these alignment procedures position-by-position for a radial scan of $T_e$ and $n_e$. This listing is perhaps one of the best arguments for the development of a true multi-point Thomson scattering diagnostic on MST (assuming, of course, that radial scans of $T_e$ and $n_e$ are desired).

The procedures listed below are simply suggestions; they must be implemented with forethought and care. The steps below are listed in roughly chronological order. See Figure III.1 for the positions of the various components.

a) Insure that the HeNe alignment laser beam follows the ruby laser beam. This is best done by placing a piece of thermal burn paper ("Zap-it" paper) in the path of the laser beam, firing the laser, and then adjusting the tri-point mounts of the HeNe laser as necessary to bring the HeNe spot to the center of the burn pattern. Remember that the ruby laser, especially when Q-switched, has tremendous destructive potential, both to humans and to inanimate objects. See the book by D.C. Winburn[4] for laser safety procedures.

b) Shut down the ruby laser system. Leave the HeNe laser on. Insert the exit alignment target to the stop mark on the shaft. This is the block of aluminum cut at 45° and mounted in a cross just before the beam dump. The



position of the alignment laser on the target may be observed through the window mounted on the top arm of the cross. Remove the laser focusing lenses from the optical train. Adjust the kinematic mount of the turning mirror until the alignment laser beam passes through the center of the input window and hits the center of the exit alignment target. If the system is badly out of alignment, the position or height of the ruby laser system may have to be adjusted before the turning mirror is adjusted.

c) Replace the laser focusing lenses. The position of the lenses on the optical rail can be calculated with the use of Figure III.2 and a knowledge of where the scattering volume is to be located. The scattering volume must be located directly below the hole in the boxport through which the Thomson scattered light is to be collected. The position of the scattering volume cannot be set by eye; the focusing lenses in the collimator must be set in the positions on the optical rail that place the scattering volume in the desired position.

d) Iteratively adjust the position of the focusing lenses perpendicular to the optical rail. The lenses are mounted on fine translation stages that move perpendicular to the optical rail. The position of the lenses should be adjusted until the alignment laser beam passes through the

center of each lens and hits the center of the exit target. Do not forget to tilt the lenses $10^{o}$ off perpendicular to the laser beam; this prevents back reflection from destroying the ruby laser. The back-reflected beams should be dumped in a strategically placed piece of black felt.

e) Check for possible obstructions in the path of the ruby laser beam. Remember that it needs a clear aperture of at least 16 mm, preferably more. Check to see that the aperture that defines the beam before the turning mirror is properly centered.

f) Now that the laser optical train has been aligned the collection optics may be aligned. The first order of business is to insert the moveable alignment target. This target, which is not shown in Figure III.1, is at the same poloidal azimuth as the laser entrance window, but is just to the side of the window at a slightly smaller toroidal angle. The alignment target is mounted on a rod that, when inserted into the vacuum vessel, travels nearly parallel to the path of the ruby laser beam. The target itself is simply a small block of aluminum cut at $45^{o}$. The target, when inserted to the center scattering volume, is $45^{o}$ off perpendicular to both the laser beam axis and the collection optics axis.



g) The alignment target is now intercepting the alignment laser beam at the center of the scattering volume. The beam spot formed on the face of the target needs to be imaged on the entrance slit of the spectrograph by the collection optics. Preliminary to the alignment of the collection optics a few things must be done. The polarizer and the RG-645 color filter must be removed from their mounts in front of the entrance slit. The 0.5 mm entrance slit must be installed. The large mirror must be positioned directly over the collection lens. The spectrograph mounting plate must be loosened from the detector platform in order to allow adjustment of the position of the spectrograph parallel to collection optical axis.

h) The scattering volume is an object 636 mm from the f = 200 mm collection lens. This means that the image of the scattering volume will be 296 mm from the collection lens. The angle of the large mirror and the position of the spectrograph must be adjusted until the alignment laser beam spot on the alignment target is imaged on the horizontal and vertical center of the entrance slit. The position of the spectrograph parallel to the collection optical axis should be adjusted first and then fixed. Then the translation stage upon which the spectrograph is mounted can be moved to adjust the position of the

spectrograph perpendicular to the collection optical axis. Once the beam spot has been centered on the entrance slit all the adjustments should be fixed in place by tightening the appropriate screws.

i) Carefully replace the polarizer and RG-645 color filter. Remove the alignment target from the vacuum vessel by first rotating it 180° out of the beam path and then retracting it to the wall of the vacuum vessel. It must be retracted into its limiter protected area on the wall when MST is being operated.

j) Make a final check to see that the alignment laser beam is still centered on the exit alignment target. Remove this target from the beam path. Turn off the HeNe laser. Turn on the ruby laser system. Make sure that no bystanders will be injured by unexpected reflections of the ruby laser beam. Check the laser optics for dust. Fire the ruby laser, first producing low power non-Q-switched pulses. If nothing appears damaged, fire the laser producing Q-switched pulses. If everything is properly aligned and working correctly, the only sound produced by the laser when it fires should be a dull thump. Any other sound, particularly any sharp snaps, indicate that something is being damaged. If everything sounds alright, turn the laser off and make a final inspection of the optics. Replace the panels removed from the laser cart



and detector platform enclosure. Restart the laser enclosure filtered air system.

k) Turn on the data acquisition system. (The procedure for accomplishing this will be covered in the next chapter.) Fire the laser and collect data for a few shots with no plasma in the vacuum vessel. If more than 20 or 30 counts of laser line light show up in any one of the spectrograph channels, then there is an alignment problem or the spectrograph is incorrectly adjusted. Make any necessary corrections.

l) Final adjustments should be made by firing the laser with a plasma in the vacuum vessel. The translation stage under the spectrograph should be adjusted in small steps to maximize the number of Thomson scattered photons collected.

Experience has shown that once the system has been properly aligned, it is very stable and will remain aligned for periods of weeks. The laser itself does have a tendency to drift out of alignment. This can be monitored by keeping daily records of the laser energy monitor and noting any trends. Laser alignment is covered in the laser manual and in additional lab notes.

As a final note, always remember that a Q-switched pulse of light from the laser has many of the properties of a projectile. It will inflict mechanical damage on anything in

its path. Be aware also of the tendency of material ejected from the surface of an object placed in the beam path to travel back up the beam path. This material carries so much momentum that it will embed itself in glass surfaces in the optical train. A number of windows have been damaged in this way.

C) Calibration of spectrograph and detector

This section covers measurement of the transfer function of the spectrograph and detector combination and measurement of the digitizer count to photoelectron conversion factor.

Measurement of the transfer function was done most efficiently and accurately in the following manner. Prior to execution of this procedure the grating drive must be absolutely calibrated and checked for linearity with lines from the spectra of mercury, argon, and hydrogen.

a) Remove the RG-645 color filter from the spectrograph, but leave the polarizer in place. Place a piece of diffusing glass next to the slit.

b) Fill the entrance slit with light from a HeNe laser. This is best done by sending the beam through a prismatic beam expander. The rectangular profile of the expanded beam should roughly match the profile of the entrance slit.



c) Starting at one end of the wavelength range of the detector sweep the 632.8 nm line across the exit plane of the spectrograph. The sweep will have to be in discrete steps, changing the grating drive at each step. The digitizer should be recording the number of counts from each channel at each step. Each step should cover about a nanometer of wavelength space in the exit plane.

d) Reconstruction of the transfer function simply involves plotting the number of counts from each channel versus the setting of the grating drive. This plot can be scaled to read in nanometers by factoring-in the dispersion of the grating. An example of such a plot is shown in Figure III.7. This plot was made with the program TRANS.

The plot of the transfer function should be scaled up to the wavelength region of interest, namely, the long wavelength side of the ruby laser line at 694.3 nm. This can be done with a knowledge of the dispersion of the spectrograph, calculated with the grating equation. The ruby laser line should be placed on the short wavelength side of channel #1. The exact position must be determined experimentally by adjusting the grating until enough rejection of the laser line is accomplished. For the 1200 g/mm ruled grating this meant setting the grating drive at 727.2. This produced the channel central wavelengths and channel widths listed in Chapter II.

The channel central wavelengths and channel widths may be determined from the plot of the transfer function. As can be seen from Figure III.7, the response curve of each individual channel is roughly trapezoidal. To a good approximation the width of each channel is equal to the FWHM of each trapezoid and the channel central wavelength is the center of the trapezoid.

Now that the channel widths and central wavelengths are known, it is easy to measure the relative efficiency of each channel. Light from a tungsten quartz-halogen bulb must be coupled into the spectrograph. The bulb is a good approximation of a black body radiator; its temperature can be measured with an optical pyrometer. Knowledge of the spectral radiance of the bulb allows calculation of the photon flux falling on each channel. Comparison of recorded flux to this calculated flux gives the relative efficiency of each channel. For the 1200 g/mm grating, these were



| Ch# | $\lambda_{ch}$(nm) | $\Delta w$(nm) | Relative Efficiency |
|---|---|---|---|
| 1 | 704.9 | 5.2 | 0.81 |
| 2 | 712.0 | 9.0 | 1.00 |
| 3 | 721.0 | 9.0 | 0.93 |
| 4 | 730.0 | 8.9 | 0.83 |
| 5 | 742.2 | 15.5 | 0.74 |

The last calibration coefficient to be measured is the factor that allows conversion of digitizer counts into photoelectrons. This conversion factor can be calculated by using the fact that repeated measurements of intensity of a constant source will be distributed according to Poisson statistics. Following the lead of Hart, et al.,[5] let

D = number of digitizer counts

C = conversion factor

P = number of photoelectrons

$\sigma_{n-1}$ = standard deviation of D

which implies

$$P = CD \tag{III.1}$$

$$\sigma_{n-1} = \frac{1}{C}\sqrt{P} \quad . \tag{III.2}$$

This can be solved to yield

$$C = \frac{S}{\sigma_{n-1}^2} \quad . \qquad \text{(III.3)}$$

The constant source used is, of course, the tungsten lamp. It is powered by a very stable DC source. The last time this conversion factor was measured 100 separate 400 ns long measurements of the source were taken. These yielded five values of the conversion factor, one from each channel. They were all similar with C approximately equal to 4/3. This is not a perfect method for measuring C because the distribution of the measurements is influenced by factors other than photon statistics, but these other factors are not overwhelming and the results are usually good.

The measurements and procedures described in this section provide all the necessary calibration coefficients. These are the channel widths and central wavelengths, the relative efficiencies of the channels, and conversion from digitizer counts to photons. These are all the coefficients necessary for electron temperature measurements. Calibration of the Thomson scattering system for absolute electron density measurements will be described in Chapter IV.



D) Other diagnostics

This section contains short descriptions of the diagnostics other than Thomson scattering that were used in the research described in this thesis.

1) Bolometer

The bolometer is a small thin piece of graphite that has a temperature dependent resistance. Energy deposited in the graphite raises the temperature of the graphite. Since very little of the energy deposited in the bolometer during a discharge of MST flows out of the bolometer during the discharge, the change in resistance during a discharge is proportional to the amount of energy deposited in the bolometer. In reality, electrical interference during the discharge prevents real-time measurement of the change in resistance of the bolometer. The best that can be done is measurement of the resistance immediately before and after the discharge. This change in resistance is then proportional to the amount of energy deposited in the bolometer over the whole of the discharge. The arbitrary bolometer units quoted in this thesis are simply proportional to this amount of energy.

The bolometer is sensitive to energy deposited by radiation and both charged and neutral particles. There are a number of subtleties associated with absorption of the

energy of charged particles and photoelectrons. These include secondary emission and charge buildup effects. This is not the proper place to delve into these problems. It is sufficient to know that the results of simple experiments indicate that the bolometer responds linearly to changes in the flux of incident energy.

2) VUV impurity radiation

Impurity radiation was monitored by a VUV spectrometer set to pass the central image to the exit slit. This spectrometer monitored radiation from the visible to the VUV. The spectral efficiency curve is not known, although it is likely that the efficiency drops off at shorter wavelengths. The impurity radiation falling on the spectrometer entrance slit came from a central diameter line-of-sight.

The VUV impurity signal quoted in this thesis is the time integral over the complete discharge of the signal from the VUV spectrometer. As can be seen from Figure III.8, the signal from the VUV spectrometer generally peaks early in the discharge; by the time the current peaks (around 15 ms), the signal is roughly zero. This is probably because the impurities that were radiating strongly in the visible during the early part of the discharge have been stripped to higher levels such as Oxygen VI and are radiating higher energy photons. The spectrometer is probably not very sensitive to



these photons. This does not matter for the present purposes as long as the amount of radiation seen in the early part of the discharge is proportional to the amount of radiation throughout the discharge. In other words, if a discharge is radiating heavily at the beginning, we assume it continues to radiate heavily. The behavior of individual oxygen and carbon lines support this assumption.

In sum then, in this thesis the VUV impurity signal in arbitrary units is directly proportional to the amount of energy lost by the discharge via radiation.

3) Plasma current

During the time period which most of the data in this thesis was taken the plasma current was not monitored in the usual manner. The Rogowski coil which should have provided this information had electrical problems which made it unreliable. This difficulty was bypassed by making use of the fact that the plasma is simply the one turn secondary of a very large transformer. Knowledge of the turns ratio and the primary current allows estimation of the plasma current. This measurement of the plasma current is compromised by the fact that the transformer saturates near the end of the discharge. This adds magnetizing current to the primary current; this effect is difficult to subtract out of the calculation of plasma current. However, during the first

20 ms of the discharge, the primary-current-generated plasma trace and that from the sometimes functional Rogowski coil showed good agreement. Since the Thomson scattering data was taken at the current peak (14 to 16 ms), this was not a great problem.

The algorithm for calculation of the loop voltage will be described in Chapter V. The only observation to make at this point is that the loop voltage calculated using the primary current generated plasma current trace was systematically a few percent smaller than the loop voltage calculated using the Rogowski coil plasma current. This does not compromise any of the conclusions in this thesis because the difference is systematic and, in this thesis, consistent use is made of the primary current generated plasma current and loop voltage.

The points listed above should be kept in mind when evaluating the results presented in this thesis. Data from other diagnostics were gathered following standard and accepted procedures.



References

[1]Y. Nagayama, K. Sakuma, and H. Toyama, Japan J. Appl. Phys. 21, 1056 (1982).

[2]D.J. Den Hartog and R.N. Dexter, University of Wisconsin-Madison PLP 1023 (1987).

[3]J.A. Casey and J.H. Irby, Rev. Sci. Instrum. 57 (8), 1804 (1986).

[4]D.C. Winburn, Practical Laser Safety, (Marcel Dekker, New York, 1985).

[5]G.W. Hart, F.M. Levinton, and D.H. McNeill, "A study of the effects of photon statistics on Thomson scattering data", PPPL-2293, Princeton Plasma Physics Laboratory (1985).

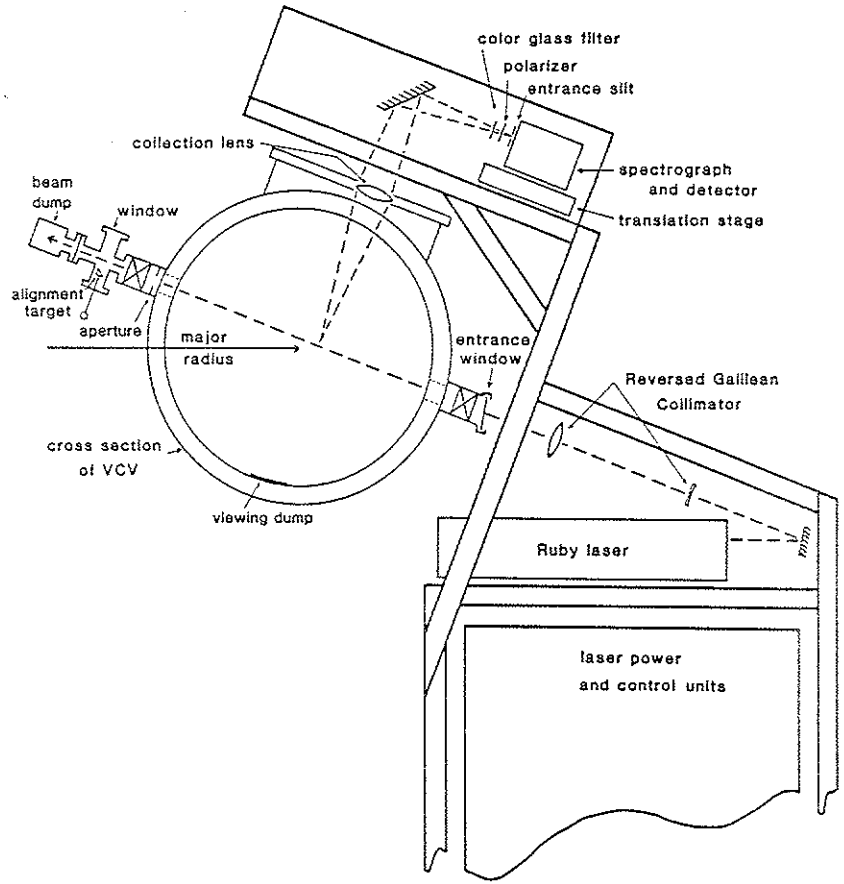


Figure III.1: Side view of Thomson scattering system on MST.
Lenses are not to scale.



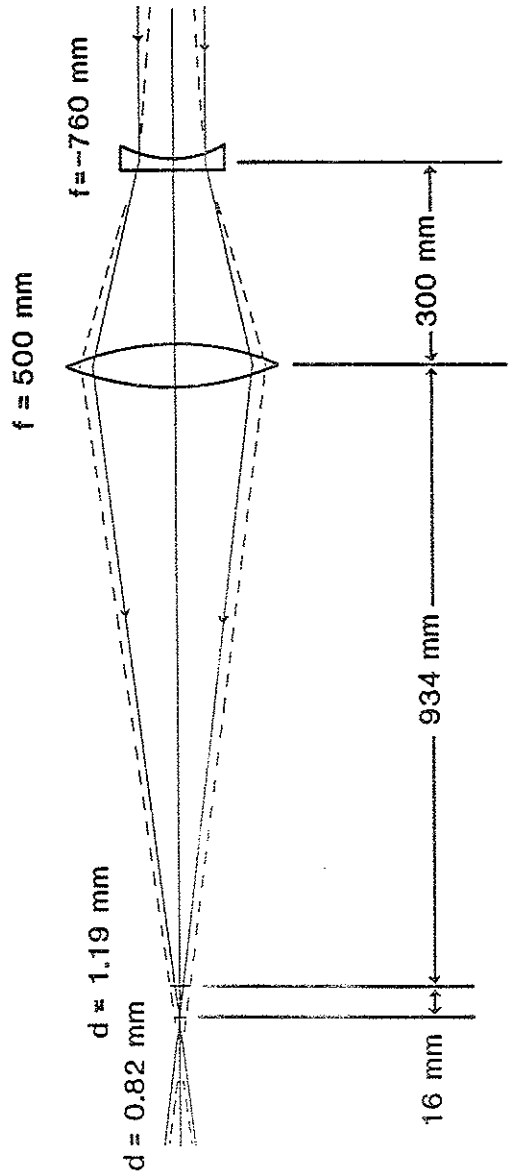


Figure III.2: The reversed Galilean collimator.

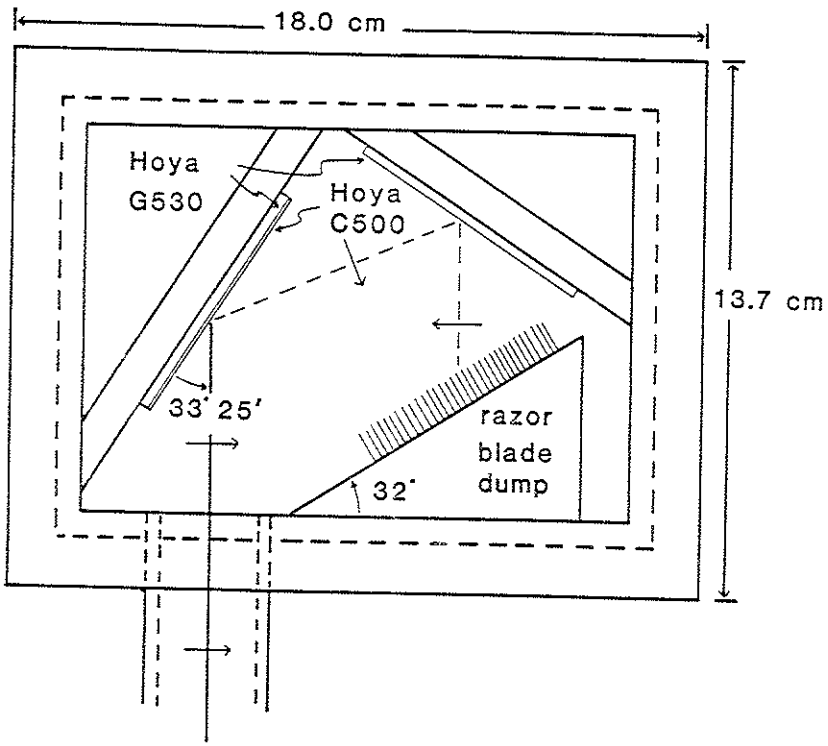


Figure III.3: The ruby laser beam dump. The arrows perpendicular to the laser beam indicate horizontal polarization.



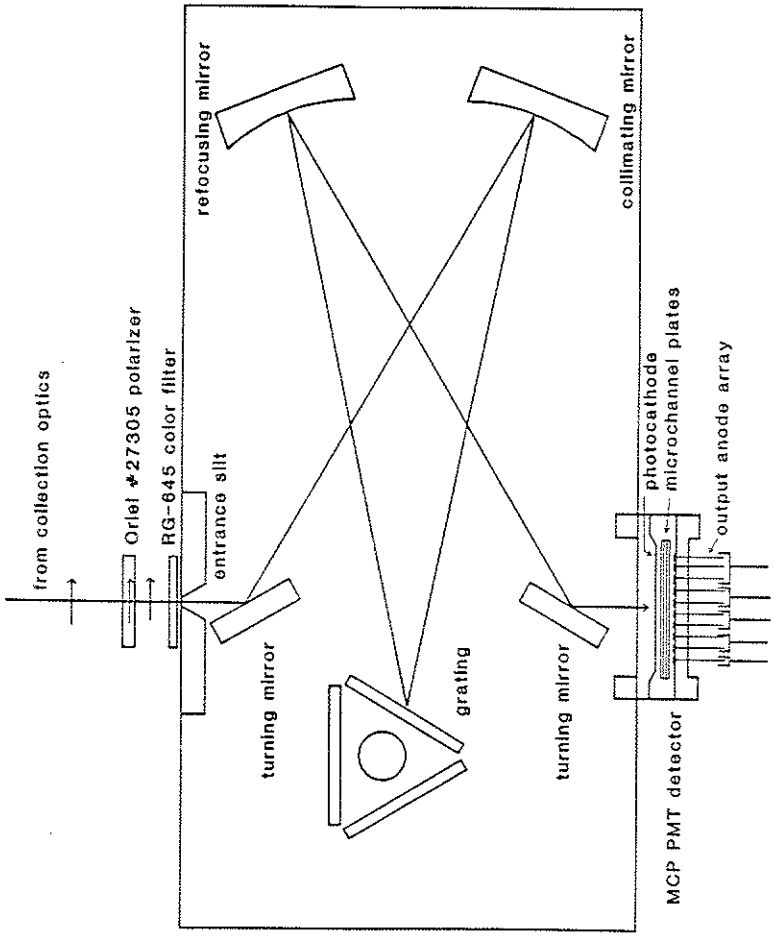


Figure III.4: The 275 mm focal length f/4.4 spectrograph.

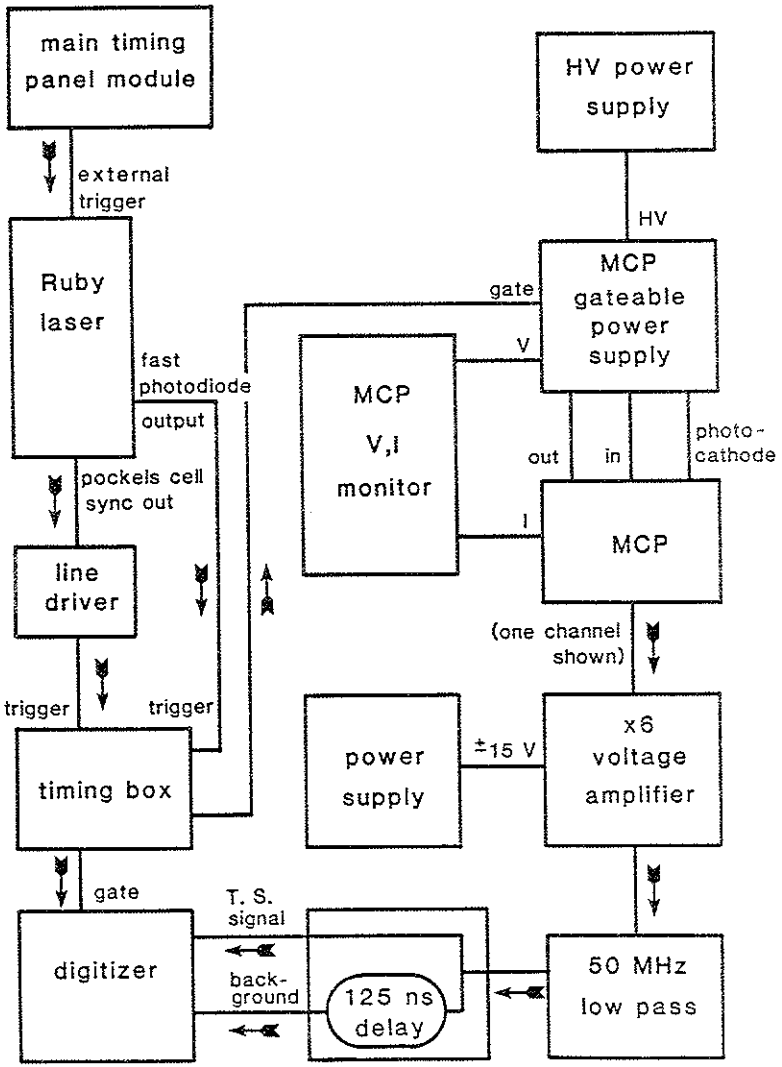


Figure III.5: The data acquisition system.



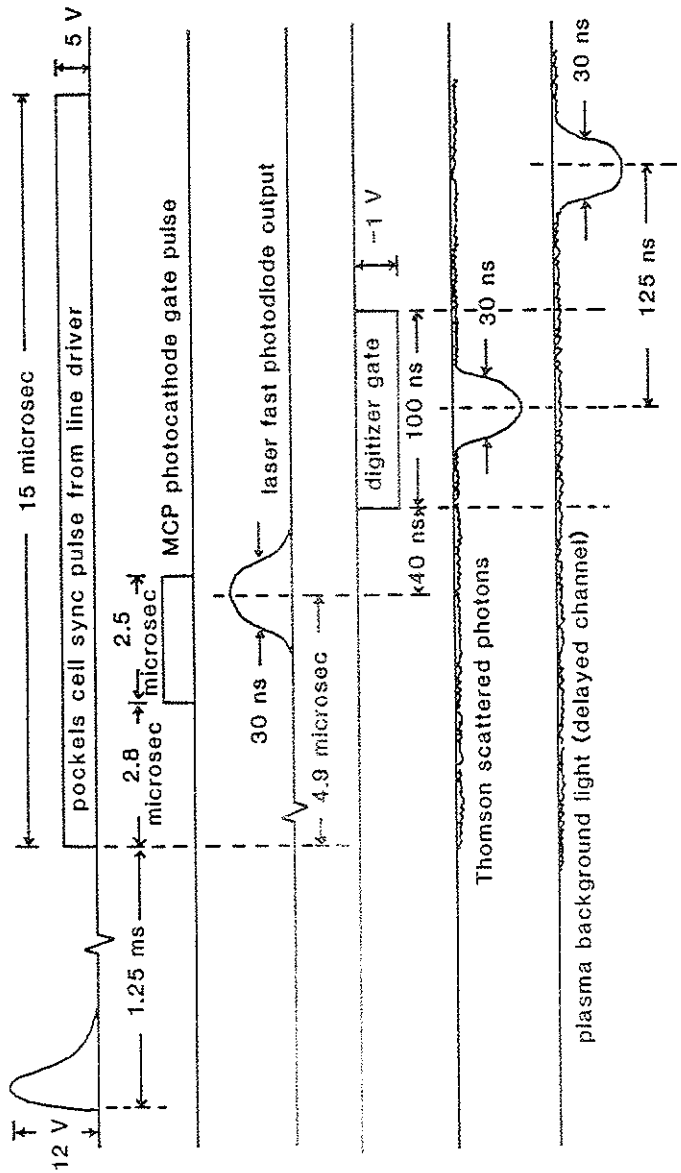


Figure III.6: The sequence of events during a data acquisition shot.

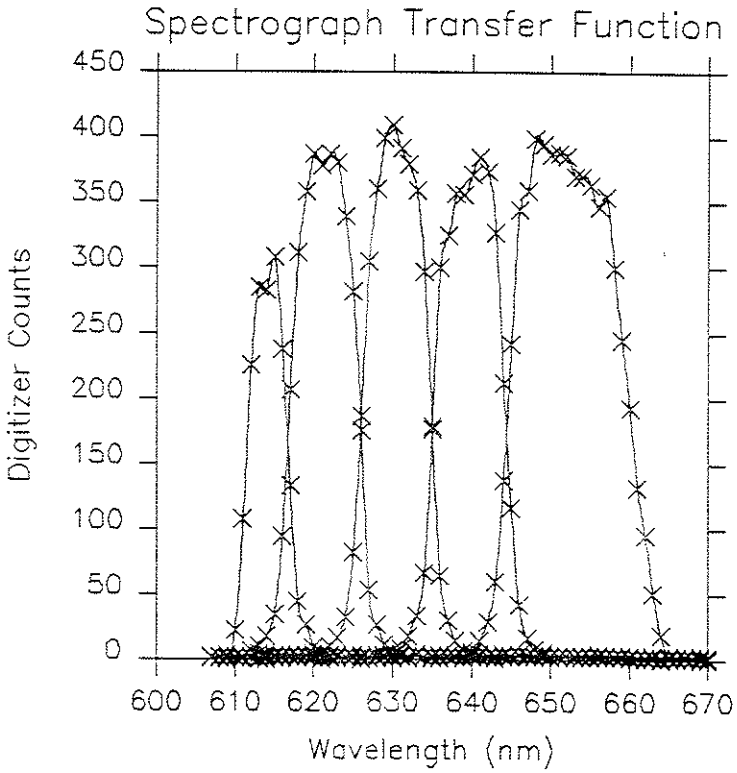


Figure III.7: The spectrograph transfer function as measured with a HeNe laser.



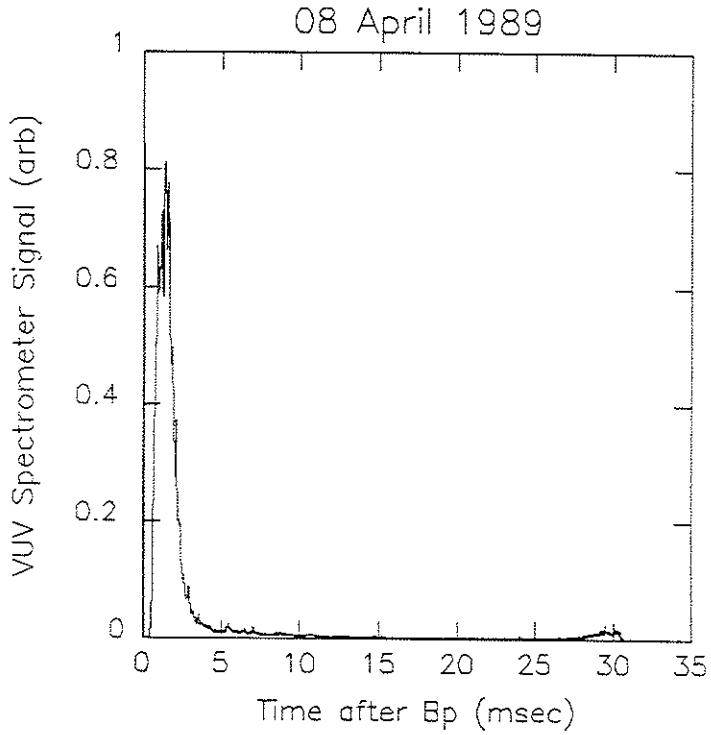


Figure III.8: The VUV spectrometer signal during a standard discharge.

# CHAPTER IV: EXPERIMENTAL PROCEDURE

## A) Data acquisition

Operation of the Thomson scattering diagnostic generally follows the following pattern:

a) Turn on the ruby laser system and allow the temperature of the rods to stabilize. The laser is generally set to produce 5 joule pulses (to avoid overstressing the beam optics), although it is capable of producing 10 joule pulses.

b) Inspect all the beam optics for dust and make sure the laser entrance and exit valves are open. Replace the panels on the laser and detector enclosures.

c) Turn on all the data acquisition electronic equipment. The high voltage on the MCP should be brought up slowly. The voltage set on the HV05 power supply is 223 volts above the voltage on the MCP. Thus, to set the MCP at 2300 volts, set the HV05 to 2523 volts. This will produce a reading of 1119 on the MCP voltage monitor and about 5.2 μA on the MCP current monitor.

d) The controls on the Thomson scattering timing box should be set to the following values:



QDC gate @100 ns, triggered by fast photodiode

MCP delay @2.8 μs

MCP gate @2.5 μs

See the instruction manual for the timing box for more information.

e) Set the main timing panel module that controls the laser trigger to send out a pulse 1.25 ms before the laser pulse is desired. In order to fire the laser at 16 ms into the discharge, set the module to pulse at 14.75 ms.

f) Turn on and mount the CAMAC crate containing the 2250L digitizer. Check to see that the MDS module that controls the digitizer is alright (the module is self-explanatory). Turn the module on.

g) Record the residual pedestal of the digitizer by triggering the timing box. Record the laser background light by pulsing the laser without a plasma in the vacuum vessel. Ten laser background shots is usually sufficient to give a good average. These two sets of numbers go into the data analysis program.

h) Start the data analysis program. It will wait for the laser to be fired. When the laser fires during an MST discharge it will be automatically triggered. The program performs a linear fit to the data (as described below) and produces an electron temperature and density.

i) Take data.

j) At the end of the run check and record all operating parameters of the laser and detection system. It is usually a good idea to again record the pedestal and laser background in case they have drifted during the day.

k) Slowly bring down the voltage on the MCP. Shut off the detection electronics and the laser.

The raw data from the Thomson scattering diagnostic must be analyzed between shots. Real-time analysis is the only way to monitor the performance of the diagnostic and to follow the effects of perturbations to MST operational parameters.

B) Data reduction

The raw data are analyzed by following this procedure:

a) The digitizer pedestal is subtracted from both the total counts (which includes the Thomson scattered counts) and the plasma background counts. This is done separately for each digitizer channel.

b) The total counts, plasma background counts, and laser line background counts from each detector channel are converted into numbers of photons.



c) The laser background light and the plasma background light are subtracted from the total light leaving the Thomson scattered light. Poisson statistics are used to estimate the uncertainty in this number. Contributions to the uncertainty come from the total number of photons and the background number of photons.

d) The Thomson scattered light and associated uncertainty from each channel are then normalized for channel gain differences and channel widths.

e) Since we assume that the electrons have a Maxwellian velocity distribution, the data can be linearized by plotting the natural log of the normalized signal in each channel versus the square of the wavelength shift from the laser line. (See Figure II.3 for an example.) The uncertainty in the signal is transformed according to the formula[1]

$$\sigma''_{ch} = \ln(1 + \sigma_{ch}/N_{ch}) \qquad \text{(IV.1)}$$

where $N_{ch}$ is the normalized signal in the channel, $\sigma_{ch}$ is the uncertainty in $N_{ch}$, and $\sigma''_{ch}$ is the transformed uncertainty.

f) This linearized data is fit to a straight line with the LINFIT routine.[2] The electron temperature is proportional to the slope of this line according to the formula[3]

$$T_e(eV) = - \frac{6.2 \times 10^4}{\lambda_i^2 \sin^2(\theta/2)} \cdot \frac{1}{\text{slope}} \qquad \text{(IV.2)}$$

where $\lambda_i$ has the same units (nanometers) as the wavelength shift from the laser line. The uncertainty in the electron temperature is directly derived from the uncertainty in the slope.

g) With this initial non-relativistic estimate of the temperature an iteration is made to provide a relativistically correct estimate of the temperature. The Thomson scattered spectrum is assumed to have the relativistic shift and distortion detailed in Eq. (II.36). This temperature dependent distortion is subtracted from the normalized raw data and the data is once again fit to a straight line. The slope of the line is proportional to the temperature as in Eq. (IV.2).

h) The electron density is directly related to the total number of scattered photons or, equivalently, to the area under the Maxwellian fitted to the raw data. The density is

$$n_e = 3.44\ D\ \sqrt{T_e(eV)}\ \exp(\text{y-int}) \qquad \text{(IV.3)}$$

where D is the calibration coefficient to be derived in the next section and the y-intercept is from the line fitted to the raw data. The uncertainty in $n_e$ comes from the



uncertainty in the calibration coefficient, the uncertainties in the slope and y-intercept, and the covariance between the slope and y-intercept.

The major problem with this linear fit analysis of the raw data is that it consistently produces temperature estimates that are, on the average, a few percent too large. (See Chapter VI for an illustration of this behavior.) There are two factors that cause this behavior. The first concerns the assumption made by the least-square linear fit that the uncertainties associated with the data points follow from a Gaussian distribution. They do not; the uncertainties are from a Poisson distribution. The net result is that the fitting routine gives too much weight to "outlier" points (it is not a statistically robust fitting routine[4]). The second problem comes from the fact that the natural log of a negative signal cannot be taken. A negative Thomson scattered light signal, even though unphysical, is statistically possible. It sometimes occurs in the wavelength channel farthest from the laser line. The Thomson scattered signal is smallest in this channel; subtraction of the background sometimes results in a negative signal. When this happens the data point cannot be used by the linear fitting routine. Throwing away these data points skews the distribution of slope estimates to a lower than realistic

mean, producing a distribution of higher than realistic temperature estimates. The sensitivity to outlier points just accentuates this problem.

The solution to this problem is the development of a fitting routine that would fit a Gaussian to the normalized (not linearized) raw data. The routine should be derived with the assumption that the uncertainties associated with the raw data are governed by Poisson statistics. Preliminary results from a non-linear least-squares fitting routine that assumes a Gaussian distribution of uncertainties are encouraging (see Chapter VI).

C) Electron density calibration coefficient

The definitive study of Thomson scattering density calibration was made by McCool et al.[5] The explanation below follows from this study; details may be found in the reference.

Equation (II.39) may be rearranged and integrated over all wavelengths to yield

$$n_e = \frac{\int_o^\infty S_T(\lambda_s)d\lambda_s}{N_I \sigma_T L \Delta\Omega \eta T} \qquad (IV.4)$$

where $\sigma_T$ is the differential Thomson scattering cross section (equal to $r_o^2$ when the scattering angle $\theta = 90^o$) and $S_T$ is



the Gaussian function fitted to the normalized raw data ($\int_o^\infty S_T(\lambda_s)d\lambda_s$ is the analog of $N_{pe}$ for all wavelengths). Equation (IV.4) can also be expressed as

$$n_e = D \int_o^\infty S_T(\lambda_s)d\lambda_s \qquad (IV.5)$$

where D is the calibration coefficient to be determined and is given by

$$D^{-1} = N_I \sigma_T L \Delta\Omega \eta T \quad . \qquad (IV.6)$$

In terms of the parameters from the linear fit, the integral is given by

$$\int_o^\infty S_T(\lambda_s)d\lambda_s = 3.44 \sqrt{T_e(eV)} \cdot \exp(y\text{-int}) \quad . \qquad (IV.7)$$

In principle all the factors in D can be calculated a priori, but in fact it is impossible to do so. The best way to determine D is to find a scattering process that mimics Thomson scattering but where the density of scattering centers can be independently measured. Rotational Ramam scattering from nitrogen fits the bill almost perfectly.

An equation similar to Eq. (IV.4) can be written for rotational Raman scattering:

$$\int_{\lambda_1}^{\lambda_2} S_R(\lambda_s)d\lambda_s = n_m N_I \sigma_R L \Delta\Omega \eta T \qquad (IV.8)$$

where

$\int_{\lambda_1}^{\lambda_2} S_R(\lambda_s)d\lambda_s$ = the relative efficiency normalized signal collected by a channel with sensitive range $\lambda_1$ to $\lambda_2$

$\sigma_R$ = the rotational Raman cross section over $\lambda_1$ to $\lambda_2$, weighted by the instrument response function (the transfer function) of the specific channel

$n_m$ = the number density of the molecular scattering centers.

The combination of Eqs. (IV.4) and (IV.8) gives

$$D = \frac{\sigma_R n_m}{\sigma_T \int_{\lambda_1}^{\lambda_2} S_R(\lambda_s)d\lambda_s} \quad . \qquad (IV.9)$$

All of the factors in this equation are known or can be be easily calculated or measured.

For the purpose of density calibration in MST nitrogen proved to be the most useful Raman scattering medium. The pressure can be easily measured (although care must be taken to insure that the measurement device is absolutely calibrated) and, at 300 K,

$$n_m(/cm^3) = 3.22 \times 10^{16} \, P(Torr) \quad . \qquad (IV.10)$$



Calculation of the Raman scattering cross section $\sigma_R$ for the wavelength region $\lambda_1$ to $\lambda_2$ is not difficult, but it does require care and attention to detail. The Raman scattered spectrum has much more structure than the Thomson scattered spectrum. Proper interpretation and use of Raman scattering date requires a thorough understanding of the response characteristics of the spectrograph.

The response of the $i^{th}$ channel of the spectrograph to a scattered flux of photons $I(\lambda)$ is given by

$$S_i = \eta_i T_i \int_0^\infty I(\lambda)\rho_i(\lambda)d\lambda \qquad (IV.11)$$

where $\rho_i(\lambda)$ is the transfer function of the particular channel normalized such that

$$\int_0^\infty \rho_i(\lambda)d\lambda = 1 \quad . \qquad (IV.12)$$

The quantum efficiency $\eta_i$ and the transmission $T_i$ are assumed to be constant over the wavelength range of the channel. For Thomson scattering the flux of photons varies slowly and approximately linearly over a single channel so that Eq. (IV.11) reduces to $S_i = \eta_i T_i I(\lambda_i)$. However, for rotational Raman scattering the spectrum is a set of discrete lines and Eq. (IV.11) is best expressed by

$$S_i = \eta_i T_i \sum_{n=0}^{\infty} I(\lambda_n)\rho_i(\lambda_n) \quad . \qquad \text{(IV.13)}$$

In the calibration experiment the signal $S_i$ is measured. The effect of the transfer function is folded into the interpretation of the data by using it to calculate the weighted cross section $\sigma_{Ri}$.

Raman scattering is a molecular scattering process. It is discussed in detail in a number of texts. Here is a short summary of relevant information from McCool et al.[5]:

> "In Raman scattering, the molecule undergoes a change in its rotational or vibrational quantum state. As the molecule loses or gains energy in the transition, the scattered photon undergoes an equal but opposite change in energy. The spacing in energy of the vibrational states is generally much greater than that of the rotational states. As a result, Raman scattering involving a change in the vibrational state of the molecule yields a large change in the wavelength of the scattered light. For many molecules, this wavelength change is too great to be of interest for Raman calibration. Consequently, only pure rotational Raman scattering will be considered.
>
> "In order to use Raman scattering as a calibration technique, the wavelength and intensity of the various lines must be known. In rotational Raman scattering the selection rule $\Delta J=\pm 2$ is obeyed, where J is the rotational quantum number. When $\Delta J$ is +2 the molecule gains energy and the wavelength of the scattered photon increases. This is termed Stokes scattering since the photon loses energy and hence obeys Stokes law. When $\Delta J=-2$ the photon gains energy from the molecule and is shifted to the blue. This is termed anti-Stokes scattering. The intensity of each line is determined by the cross section for that line weighted by the fraction of molecules in the appropriate initial state."



Since our spectrograph is sensitive only to the long wavelength side of the ruby laser line, our concern is limited to Stokes scattering. The relative intensities of the individual Raman lines for Stokes scattering from nitrogen are shown in Figure IV.1. The degeneracy of the nuclear spin causes the alternation in intensities of the Raman lines.[5]

The effective Raman cross section for the $i^{th}$ spectrograph channel is

$$\sigma_{Ri} = \sum_{J=0}^{\infty} F_J \sigma_{J\to J+2} \rho_i(\lambda_{J\to J+2}) \qquad \text{(IV.14)}$$

where

$F_J$ = the fraction of molecules in state J

$\sigma_{J\to J+2}$ = the differential cross section for the specific transition.

The transfer function $\rho_1(\lambda)$ for the channel #1 is shown in Figure IV.2. It was measured using the technique described in Chapter III. Calculation of the effective Raman cross section for channel #1 gives $\sigma_{R1} = 0.3 \times 10^{-31}$ cm$^2$. Channel #1 is the only channel with a finite Raman scattering cross section; Figure IV.1 shows that the relative intensities of the lines are approximately zero for the other channels.

The effective Raman scattering cross section is much smaller than the Thomson scattering cross section. For this reason, the number density of scattering centers must be much greater for Raman scattering calibration than for normal Thomson scattering operation. The high number density of scattering centers was achieved by filling MST with several hundred Torr of nitrogen. However, other than the fact that the vacuum vessel is filled with nitrogen instead of plasma, the data acquisition procedures for Raman scattering are exactly the same as for Thomson scattering.

Reduction of the raw Raman scattering data requires a procedure for subtraction of Rayleigh scattered light from the total light signal recorded during the scattering experiment. The Rayleigh scattered light is at the same wavelength as the laser line. But, because the Rayleigh scattering cross section is a factor of 7000 greater than the effective Raman scattering cross section and because the spectrograph has a finite rejection ratio, the Raman and Rayleigh signals in channel #1 are nearly equivalent. It is possible to subtract the Rayleigh scattered light from the total signal because the response of the spectrograph to laser line light is well known from the records of laser background light. This response function is simply scaled to match the counts in channels #3 through #5 (where there should be no Raman scattered light). The scaled response



function is then subtracted from the total signal leaving, presumably, only the Raman scattered signal.

Calculation of the calibration coefficient is done with

$$D = 4.05 \times 10^{41} \frac{\sigma_{R1}(cm^2)P(Torr)}{\int^{\Delta w_1} S_{R1}(\lambda)d\lambda} \qquad (IV.15)$$

where $\int^{\Delta w_1} S_{R1}(\lambda)d\lambda$ is the Raman scattered signal from channel #1, normalized for the relative efficiency of channel #1. Major contributions to the uncertainty of the calibration coefficient come from the uncertainties in the Raman scattered signal, the transfer function, and the cross sections of the individual Raman lines. Putting everything together gives a calibration coefficient $D = 1.47 \pm 0.16 \times 10^{10}$ $cm^{-3}$. Of course, this particular coefficient is applicable only to the MST Thomson scattering diagnostic when set up and operated as during March and April of 1989 (when most of the data for this thesis was taken).

The Raman scattering data can be used to estimate the transmission of the collection optical system. Solving Eq. IV.8 for T and using the values for the other parameters as stated in Chapter II, the Raman scattering data from channel #1 yields $T \cong 0.04$. This is similar to the estimate

that could have been made by comparing the actual to the estimated photoelectron counts given in Chapter II.

The Rayleigh scattering data from the Raman scattering calibration experiment can be used to calculate the rejection ratio of the spectrograph channels. For Rayleigh scattering,

$$N_p = N_I n_m \sigma_{Ray} L \Delta\Omega T \qquad \text{(IV.16)}$$

where $\sigma_{Ray} = 2.10 \times 10^{-28}$ cm$^2$ for $N_2$ and the other parameters are as previously stated. Comparison of the number of photons reaching the exit plane of the spectrograph to the number of photoelectrons divided by $\eta$ recorded by each channel gives a rejection ratio of about $1 \times 10^{-4}$ for each channel. This is not too bad, but could probably be improved by a factor of ten to one hundred by using a holographic grating.[6,7]

This rejection ratio, when coupled with the average number of laser line background photons registered by the spectrograph channels, indicates that only $10^6$ laser line photons (not Thomson scattered photons) reach the exit plane of the spectrograph during an average Thomson scattering data shot. Of these $10^6$ photons, only 1600 reach the detector channels. This is an amazingly small number in light of the fact that $10^{19}$ photons leave the laser. But, performance like this is demanded by the fact that only ~5000 Thomson



scattered photons reach the detector channels during a normal shot.

References

[1]M.G. Nicholson, Plasma Physics 26, 1035 (1984).

[2]P.R. Bevington, Data Reduction and Error Analysis for the Physicals Sciences, (McGraw-Hill, New York, 1969).

[3]J. Sheffield, Plasma Scattering of Electromagnetic Radiation, (Academic Press, New York, 1975).

[4]W.H. Press et al,, Numerical Recipes, (Cambridge University Press, Cambridge, 1986).

[5]S.C. McCool et al., "Calibration of Thomson Scattering Density Measurements", Fusion Research Center Report #234, University of Texas at Austin (1981).

[6]D.J. Den Hartog and R.N. Dexter, University of Wisconsin-Madison PLP 1023 (1987).

[7]J.A. Casey and J.H. Irby, Rev. Sci. Instrum. 57 (8), 1804 (1986).



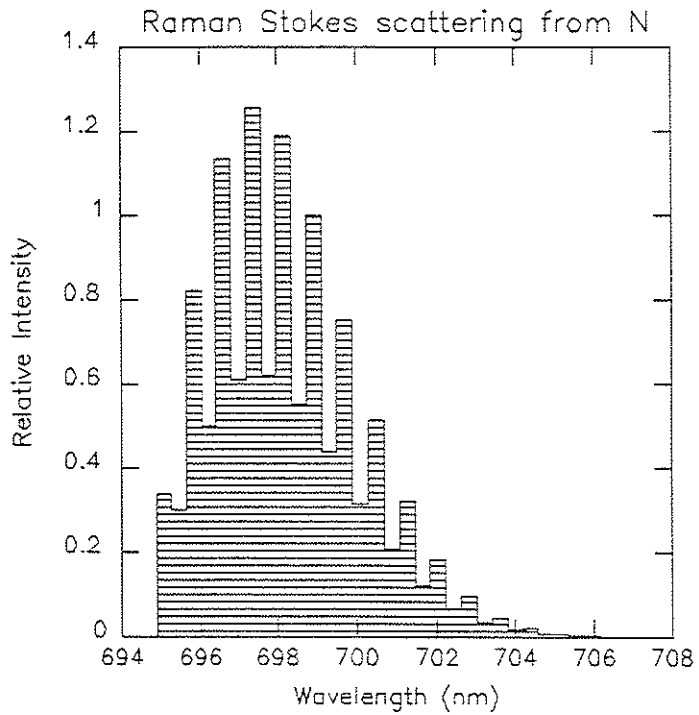


Figure IV.1: The relative intensities of the lines in the nitrogen Raman Stokes scattering spectrum.

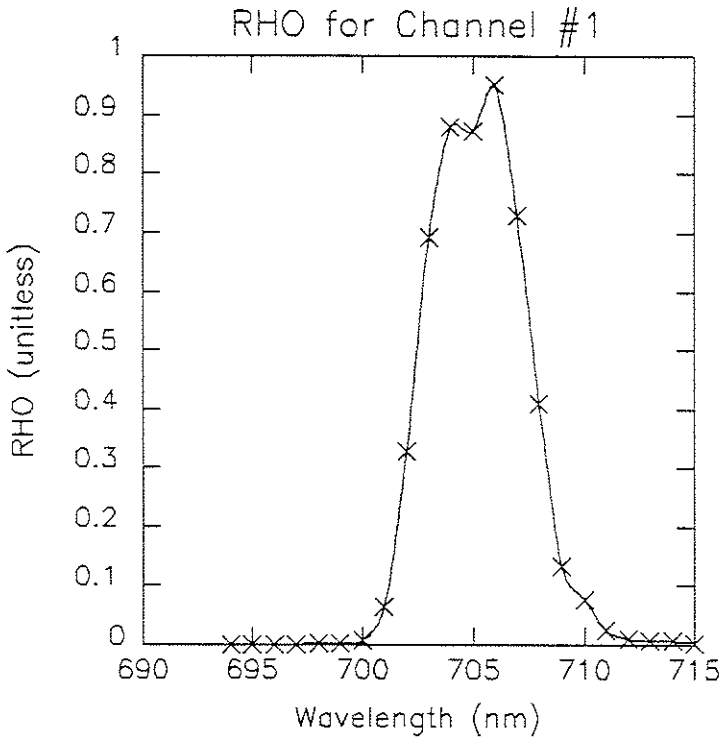


Figure IV.2: The transfer function ($\rho(\lambda)$) for spectrograph channel #1.



## CHAPTER V: INTRODUCTION TO RFP CONFINEMENT

### A) Global parameters describing confinement

The two global parameters often used to quantify the energy confinement of a magnetically confined plasma are the energy confinement time ($\tau_E$) and the poloidal beta ($\beta_\theta$). (They are called "global parameters" because they describe the plasma as a whole, usually by averaging over some combination of basic quantities such as temperature, density, or current.) The energy confinement time is usually defined as (plasma energy)/(ohmic heating power) which is expressed by

$$\tau_E = \frac{\int \frac{3}{2} (n_e T_e + n_i T_i) dV}{V_{loop} I_p} \quad . \qquad (V.1)$$

The poloidal beta is a measure of (plasma thermal pressure)/(magnetic field energy density), defined as

$$\beta_\theta = \frac{\frac{\int (n_e T_e + n_i T_i) dV}{\int dV}}{\frac{1}{2\mu_0} B_\theta^2(a)} \quad . \qquad (V.2)$$

This is, of course, a unitless ratio and is usually less than one. It is related to the cost of confining the plasma and should be large for an economical high power density fusion reactor.

The symbols in the above expressions are defined as follows:

$n_e$, $n_i$ = electron, ion densities

$T_e$, $T_i$ = electron, ion temperatures

$V_{loop}$ = loop voltage[1]

$I_p$ = plasma current

$B_\theta(a)$ = poloidal magnetic field at the wall

$\mu_0 = 4\pi \times 10^{-7}$ webers/amp-meter.

The integral is over the entire volume of the plasma. All quantities are, in general, time varying so that a quoted $\tau_E$ and $\beta_\theta$ must be associated with a specific period of the discharge. The temperatures and densities are, in addition, spatially varying.

The usual procedure used to maximize $\tau_E$ is to attempt to raise the temperatures and densities while keeping the loop voltage low. There are, of course, many subtleties associated with this procedure, not the least of these being the measurement of a loop voltage. Due to inductive effects and coupling between the toroidal and poloidal field circuits, the loop voltage is not just the integral of the



electric field around a simple loop when the fields and currents are changing. The details of loop voltage measurement and calculation on MST (and the measurement and calculation of the other global electrical parameters) are covered in references 1 and 2.

Also related to the global electrical parameters is the calculation of the poloidal field at the wall, $B_\theta(a)$. Assuming cylindrical symmetry (which is an acceptable assumption for MST) and using Ampère's law,

$$B_\theta(a) = \frac{\mu_0 I_p}{2\pi a} \quad . \tag{V.3}$$

This figure is within a few percent of the poloidal field measured at the wall with fixed-coil sets.[3]

The real difficulties in the calculation of $\tau_E$ and $\beta_\theta$ come when one begins to make the assumptions and approximations necessary for the calculation of the integrals involving temperatures and densities. There is almost no measured profile information available from MST. The Thomson scattering diagnostic measured $T_e$ and $n_e$ at a single point in the center of the discharge. The microwave interferometer, which measured central line-averaged electron density ($\bar{n}_e$), gave reliable information only intermittently. Radial arrays of soft x-ray and visible detectors were available, but the

connection of such signals to $T_e$ and $n_e$ is complex. Probe measurements more than a few centimeters into the plasma were impossible because the plasma immediately destroyed any probe inserted much past the wall. (Robust probes are now being developed.)

In addition to a lack of profile information is a lack of information about $n_i$ and $T_i$. A charge exchange analyzer was being constructed, but did not commence operation before the April 1989 shutdown for installation of poloidal field windings on MST. Doppler broadening measurements of a carbon III line were made and indicate impurity ion temperatures comparable to measured electron temperature,[4] but this information is of limited use because the carbon III radial profile is not known. Ion and electron densities are coupled via the requirement of quasi-neutrality, but the effect of impurity or dopant ions on $n_i$ (and $Z_{eff}$) is difficult to quantify (this topic will be discussed in more detail in the section covering the argon doping experimental results).

In light of the above and realizing the necessity that approximations need to be made, let us define a form factor (see reference 5 for another example of this procedure):



$$f = \frac{\frac{\int (n_e T_e + n_i T_i) dV}{\int dV}}{2 n_{eo} T_{eo} \left( \frac{1 + a_1 a_2}{2} \right)} \quad . \tag{V.4}$$

$n_{eo}$ and $T_{eo}$ are the central electron density and temperature and

$$a_1 = \frac{n_i}{n_e} \tag{V.5}$$

$$a_2 = \frac{T_i}{T_e} \tag{V.6}$$

are assumed to be constants determined by the type of discharge. Given the temperatures and densities of MST plasmas, it is reasonable to assume that

$a_1 = 1$ for hydrogen plasmas

$a_1 = \frac{1}{2}$ for helium plasmas.

($a_1$ for argon doped plasmas will be discussed later.) And, although data from other devices contradict this assumption,[6,7,8,9] we take

$a_2 = 1$ for all plasmas.

Now that we have a form factor f, we define

$$\tau_{EF} = \frac{(\frac{3}{2})\ 2n_{eo}T_{eo}\ (\frac{1 + a_1a_2}{2}) \cdot \text{Plasma Volume}}{V_{loop}\ I_p} \quad (V.7)$$

$$\beta_{\theta F} = \frac{2n_{eo}T_{eo}\ (\frac{1 + a_1a_2}{2})}{\frac{1}{2\mu_0}\ (\frac{\mu_0 I_p}{2\pi a})^2} \quad (V.8)$$

which implies

$$\tau_E = f \cdot \tau_{EF} \quad (V.9)$$

$$\beta_\theta = f \cdot \beta_{\theta F} \ . \quad (V.10)$$

(Note also that $\tau_{EF} = 3/8\ \mu_0 R_0 \beta_\theta (I_p/V_{loop})$).

We take the plasma volume to be equal to $2\pi R_0(\pi a^2)$ where major radius $R_0 = 1.5$ meters and minor radius $a = 0.52$ meters. These definitions allow $\tau_{EF}$ and $\beta_{\theta F}$ to be calculated using information readily available, namely central electron density and temperature, loop voltage, and plasma current. Then, with an estimate of the form factor f, these can easily be translated into estimates of $\tau_E$ and $\beta_\theta$.



In this thesis, all graphs and calculations which include poloidal beta and/or energy confinement time will use the quantities $\beta_{\theta F}$ and $\tau_{EF}$ in place of $\beta_\theta$ and $\tau_E$. (This means that all measured values of $\beta_\theta$ and $\tau_E$ quoted for MST in this thesis are really quotes of $\beta_{\theta F}$ and $\tau_{EF}$.) An estimate of f using currently available profile information will be stated below. Then, as the MST data base increases in the years to come, the estimate of f may improve and the true values of $\beta_\theta$ and $\tau_E$ may be more closely approximated by using the simple relations stated above.

The quantities in the form factor f that are the most difficult to estimate are the temperature and density profiles necessary for the volume integral which gives the plasma energy. We begin by assuming cylindrical symmetry. That is, $T_e = T_e(r)$ and $n_e = n_e(r)$, which are probably good approximations. There is no temperature profile information from MST other than that which can be postulated from a $n^\alpha T^\gamma$ ($\alpha$, $\gamma$ are unknown constants) dependence of the soft x-ray signal. There is some density profile information. Edge probe measurements in low current (~220 kA) RFP discharges indicate an electron density of $2 \times 10^{12}$ $cm^{-3}$ to $4 \times 10^{12}$ $cm^{-3}$.[10] An examination of a set of microwave interferometer data revealed about 30 believable traces, i.e., minimal dropouts, smooth trace, and a reasonable return to baseline. These provided a set of line-averaged electron densities $\bar{n}_e$

to compare with the Thomson scattering central density $n_{eo}$. As can be seen from Figure V.1, the relationship is approximately $n_{eo} = (2.0\pm0.5)\bar{n}_e$. If we assume a profile of the form $n_e(r) = n_{eo}(1-(\frac{r}{a})^2)^\alpha$, we have enough information to compute $\alpha$. The line-averaged density and the central density are related, by definition, as follows:

$$\bar{n}_e = \frac{1}{a}\int_0^a n_{eo}(1 - (\frac{r}{a})^2)^\alpha dr \quad . \tag{V.11}$$

The solution of this integral involves the gamma function and is

$$\frac{n_{eo}}{\bar{n}_e} = \frac{2\Gamma(\alpha + \frac{3}{2})}{\Gamma(\alpha + 1)\Gamma(\frac{1}{2})} \quad . \tag{V.12}$$

Using the relationship between $n_{eo}$ and $\bar{n}_e$ stated above, we find that

| $n_{eo}/\bar{n}_e$ | $\alpha$ |
|---|---|
| 1.5 | 1.0 |
| 2.0 | 2.3 |
| 2.5 | 4.1 |

Figure V.2 shows the function $(1 - (\frac{r}{a})^2)^\alpha$ plotted for these values of $\alpha$. Only for $\alpha = 1$ is there enough density near the



edge to account for the probe measurements of $\sim 10^{12}$ $cm^{-3}$ at the edge. Therefore, we will assume that $n_e(r) = n_{eo}(1 - (\frac{r}{a})^2)$.

RFP density and temperature profile measurements are not abundant. Radial profile measurements of $T_e$ and $n_e$ in ETA-BETA II using a Thomson scattering diagnostic have shown the temperature profile to be fairly flat in the center, dropping off only near the edge of the plasma, while the density profile is a bit more peaked.[11] Measurements made with an array of surface barrier diode x-ray detectors on HBTX1A suggest a temperature profile that is substantially flat across the plasma diameter.[12] Abel inversion of eight-chord data from ZT-40M shows the density peaked on axis, falling gradually to the edge.[5]

Therefore in order to calculate an estimate of the form factor f, we will assume the density profile noted above and take $T_e(r) = T_{eo}$. Using the definition for f and the relationships for $n_e$, $n_i$ and $T_e$, $T_i$ noted above, we have $f = \frac{1}{2}$ for all plasmas. This means, of course, that $\tau_E = \frac{1}{2}\tau_{EF}$ and $\beta_\theta = \frac{1}{2}\beta_{\theta F}$.

There is one more definition that will prove useful later. Define

$$\frac{I_p}{N} = \frac{I_p}{\int n_e dA} \tag{V.13}$$

where N is known as the "line density" and is the density integrated over the cross-section of the plasma column. The units of $I_p/N$ are amp-meter. As we have done before, define a form factor g such that

$$g = \frac{n_{eo} \cdot \text{Area}}{\int n_e dA} \quad . \tag{V.14}$$

Also define

$$\left(\frac{I_p}{N}\right)_G = \frac{I_p}{n_{eo} \cdot \text{Area}} \tag{V.15}$$

which implies

$$\frac{I_p}{N} = g \cdot \left(\frac{I_p}{N}\right)_G \quad . \tag{V.16}$$

$(I_p/N)_G$ will be used in all graphs and calculations. Applying the density profile assumed above to calculate g gives g = 2.

Remember that the estimates of the form factors f and g are subject to many assumptions. It is impossible to quote an uncertainty in these estimates except to say that it is large.



B) Anomalous resistivity of the RFP.

In the field of plasma physics, references to the "classical resistivity" of a plasma usually refer to the resistivity as calculated from the formulas and coefficients first worked out by Spitzer and Härm.[13] This so-called "Spitzer resistivity" is determined primarily by the actions of the electrons (which are the current carriers) in a completely ionized plasma. The electrons achieve a balance between the acceleration of the applied electric field and the deceleration of Coulomb collisions with the ions and other electrons.[14] The expression for the Spitzer resistivity is

$$\eta_{sp} = 5.2 \times 10^{-5} \frac{Z_\sigma \ell n \Lambda}{T_e^{3/2}} \text{ ohm-meter} \tag{V.17}$$

where $T_e$ is in eV, $Z_\sigma$ is the resistance anomaly defined by the ion charge (not equal to $Z_{eff}$)[14], and $\ell n \Lambda$ is the Coulomb logarithm. $Z_\sigma$ and $Z_{eff}$ are directly related; this will be shown explicitly in Chapter VI. $Z_{eff}$ is a measure of the mean ion charge of the plasma, defined as

$$Z_{eff} = \frac{\Sigma_i n_i Z_i^2}{\Sigma_i n_i Z_i} \quad . \tag{V.18}$$

The above expression for resistivity should be fully applicable to current flow parallel to a magnetic field, which is largely the case in the RFP ($\underline{J}_\parallel >> \underline{J}_\perp$).

The Spitzer resistivity is most strongly dependent on the mean ion charge and electron temperature. The Coulomb logarithm is a slowly varying function. Calculation of the resistivity profile of an RFP requires knowledge of the electron temperature and $Z_{eff}$ profiles (which are usually not well-known). The expected loop voltage can then be calculated given a current profile (measured or from a model). There are a number of equivalent methods for the expression of the occurrence of anomalous resistivity on an RFP (i.e., anomalous loop voltage or anomalous $Z_{eff}$). The procedure that seems to provide clarity and ease of comparison between different devices and discharges is to simply quote the ratio of $\eta_\parallel^*$, the measured parallel resistivity (assume perpendicular conductivity is negligible), to $\eta_{sp}$, the Spitzer resistivity. Measured parallel resistivity in a steady state RFP is defined by[1]

$$\eta_\parallel^* = \frac{V_\ell I_p}{4\pi^2 R_0 \int_0^a \frac{(\underline{J}\cdot\underline{B})^2}{B^2}\, r dr} \qquad (V.19)$$



which, in the MST, using the PFM,[1] is conveniently expressed by

$$\eta_\parallel^* = \left(\frac{V_\ell}{I_p}\right)\left(\frac{\pi a^2}{2\pi R_0}\right)\left[\frac{5(10+\theta^2)}{11(5+6\theta^2)}\right] . \qquad (V.20)$$

This expression includes the effects of the current density profile and the "screw-up factor"[1]. The Spitzer resistivity, $\eta_{sp}$ is calculated using the measured $T_{eo}$ and $Z_o$ expected from the gas fill (ignoring impurity effects). The assumption that the resistivity of a steady-state RFP plasma is a constant is reasonable, if, as is usually presumed, temperature and $Z_{eff}$ profiles are fairly flat.

The simple approach to a definition of resistivity outlined above follows the example of other authors[15,16] and forms sufficient basis for comparison of experiment to theory. It is helpful to note that for hydrogen plasmas the ratio $\eta_\parallel^*/\eta_{sp}$ is often referred to as the "apparent" or "anomalous" $Z_{eff}$. This is not a strictly correct use of the definition of Spitzer resistivity (in general, $Z_{eff} \neq Z_o$), and we shall avoid it.

All RFP devices have recorded observations of anomalous resistivity. The resistivity $\eta_\parallel^*$ (or a calculational variant) is one to fifteen or greater times the resistivity expected from the measured $T_e$ and $Z_{eff} = 1$ for hydrogen

discharges.[15] Empirically, this ratio appears to be directly proportional to $I_p/N$[7,15,16] and indirectly varying with the size and number of field errors.[7,17] The correlation of field errors with plasma resistance is particularly striking in the HBTX series of machines,[7,17] The resistance dropped sharply when field errors were reduced and a DC vertical field was used to center the plasma.

This phenomenon of anomalous resistivity has a strong impact on the energy confinement properties of the RFP. The energy confinement time $\tau_E$ is inversely proportional to the loop voltage $V_\ell$, which means that for a given plasma current, $\tau_E$ is inversely proportional to the resistance of the plasma. Clear examples of this relationship have been observed on ETA-BETA II and HBTX1A and -1B; $\tau_E$ dropped as $I_p/N$ (and concomitantly plasma resistance) was increased.[7,16] In both these cases, $\tau_E$ dropped in spite of the fact that measured $T_{eo}$ increased as $I_p/N$ was increased. The ETA-BETA II measurements were compromised by the assumption that $T_i = T_e$, but some measured $T_i$ information went into the HBTX calculations of $\tau_E$. A particularly interesting observation from these experiments was the rise of both $T_{eo}$ and measured plasma resistance as $I_p/N$ was increased. Spitzer's model, of course, predicts that resistivity should drop as $T_e$ rises. The ETA BETA II data are particularly striking in this regard as the ratio of measured $\eta^*_\parallel$ to Spitzer resistivity rose from



3 to ~15 as $I_p/N$ was increased from $2 \times 10^{14}$ amp-m to $15 \times 10^{14}$ amp-m.[16] This sharp rise in measured resistivity easily mitigated the observed rise in $T_{eo}$ to cause degraded $\tau_E$ at high $I_p/N$.

This phenomenon of anomalous resistivity has, of course, engendered a number of explanations. These fall into three major categories:

1) Anomalous resistivity may be due, at least in part, to actual increases in $Z_{eff}$ caused by intrusion of impurities into the plasma.[18,19]
2) Resistivity in the RFP cannot be correctly calculated with a simple Ohm's law model that neglects fluctuations. If fluctuations are to be ignored (primarily because they are difficult to absolutely quantify), then resistivity should be calculated from models based on helicity and/or energy balance and/or helicity dissipation.[7,17,20,21]
3) Loop voltage (and the apparent resistivity) cannot be fully described by MHD based models. A kinetic approach shows that loop voltage is affected by fast electrons carrying momentum directly to the walls or limiters.[22]

Each of these explanations will be discussed briefly below, with a comment on implications for energy confinement. Bear

in mind that these theories are not mutually exclusive; behavior of the RFP may embody aspects of each.

Direct spectroscopic measurements of $Z_{eff}$ have been made on all major RFP devices. Particularly comprehensive studies have been made on ZT-40M,[19] ETA-BETA II,[18] and HBTX.[7] Weber concluded that metal impurities (high-Z) play a significant role in determining the resistivity of ZT-40M operated without limiters.[19] Plasma-wall interactions were cited as the cause of the introduction of these impurities into the plasma. Field errors appeared to cause the plasma wall interaction. The spectroscopic $Z_{eff}$ = 3-4 for 120 kA discharges was self-consistently explained by <1% chromium or nickel in the plasma. Higher temperature, lower density discharges at 120 kA (higher $I_p/N$) showed spectroscopic $Z_{eff}$ approaching 7. The resistive anomaly is not fully explained by these measurements, but there is no doubt that impurities affect the measured resistivity of ZT-40M without limiters.

Gabellieri *et al.* derived $Z_{eff}$ profiles for ETA-BETA II that peak at the edge.[18] These were derived by inverting line integral emission measurements and folding in temperature and density profiles. These $Z_{eff}$ profiles result in enhanced dissipation of power and/or helicity which requires a larger loop voltage to sustain the current density profile characteristic of a pinch. It is claimed that these $Z_{eff}$ profiles and this mechanism can account for differences



of up to 20 between the simple Ohm's law resistivity and expected Spitzer resistivity.

Radiation studies in HBTX indicate that impurity effects alone definitely cannot account for the observations of anomalous resistivity.[7] The HBTX1B $Z_{eff}$ profile does not peak at the edge. And, even when resistivity is determined electrically from the helicity balance (a procedure that will be discussed shortly), the spectroscopic $Z_{eff}$ is 3-4 times less than the $Z_{eff}$ needed to account for the helicity balance resistivity. A convincing explanation of this discrepancy has not yet been given, but we are ahead of the story and must return to topics that have previously been hinted at, namely helicity and energy balance in the RFP.

When it became apparent that a simple Ohm's law (ignoring fluctuations) was not adequate to explain the resistivity of any RFP, a search for alternatives began. For a plasma, Ohm's law is

$$\underline{E} + \underline{u} \times \underline{B} = \eta_{\parallel}\underline{J}_{\parallel} + \eta_{\perp}\underline{J}_{\perp} \qquad (V.21)$$

where $\underline{E}$ is the electric field, $\underline{u}$ is the local plasma velocity, and $\underline{J}_{\parallel}$ and $\underline{J}_{\perp}$ are currents parallel and perpendicular to $\underline{B}$, respectively. Taking the average velocity $\langle\underline{u}\rangle$ to be negligibly small[21] and neglecting fluctuating terms gives the simple resistivity $\eta_{\parallel}^{*}$ calculated

above. However, fluctuations may be important; they may, for instance, drive the mean poloidal plasma current during the steady-state phase of an RFP discharge.[20] In other words, fluctuations may be the coupling mechanism whereby power from the toroidal electric field and current sustain the continuously relaxing RFP field configuration, that is, the "dynamo effect".

More accurate estimates of resistivity can be drawn from global power and helicity balance relationships. In an RFP with a conducting shell, the time derivatives of magnetic energy W and helicity K are respectively

$$\frac{dW}{dt} = I_\phi V_\phi - I_\theta V_\theta - \int \underline{E} \cdot \underline{J} dV \qquad (V.22)$$

and

$$\frac{dK}{dt} = 2\Phi V_\phi - 2 \int \underline{E} \cdot \underline{B} dV \qquad (V.23)$$

where $\Phi$ is the toroidal flux. By using Ohm's law, taking appropriate averages, and neglecting small terms Schoenberg et al.[20] showed that

$$\frac{d\langle W\rangle}{dt} \simeq I_\phi V_\phi - I_\theta V_\theta - \int \eta_m^W \langle \underline{J}_m \rangle^2 dV \qquad (V.24)$$



and

$$\frac{d\langle K\rangle}{dt} = 2\Phi V_\phi - 2 \int \eta_m^K \langle \underline{J} \rangle \cdot \langle \underline{B} \rangle dV \qquad (V.25)$$

where $\eta_m^W$ and $\eta_m^K$ are the effective resistivities defined by magnetic energy and helicity balance respectively. They, by themselves, do not delineate the mean field versus fluctuational contributions to resistivity.[20] However, Schoenberg et al. showed that $\eta_m^K$ is a much better representation of the actual resistivity $\eta_m$ than $\eta_m^W$ when fluctuations are ignored as is done in the two defining equations above. Thus, we now have a reasonable way to estimate the resistivity of a steady-state RFP discharge. Note that the actual measured toroidal loop voltage $V_\ell$ is much larger than that obtained from the simple Ohm's law where $V_\ell = 2\pi R_0 \eta_m^K J_\phi(0)$. The difference is ascribed to the supposition that power absorbed on axis drives both the dynamo and local ohmic heating.[20]

Since the difference between $\eta_m^K$ and the actual $\eta_m$ appears to be small, a reasonable estimate of the fraction of the input power absorbed by fluctuations (as opposed to power absorbed by simple Ohmic heating) is given by[9]

$$P_F = 1 - \frac{\eta^k}{\eta^w} \quad . \qquad (V.26)$$

This power is available to drive the dynamo, MHD modes, and ion heating. In the BFM fully relaxed minimum energy state of an RFP $\eta_m^k = \eta_m^w$ (and $P_F = 0$).[21] However, the real RFP is engaged in a dynamic relaxation process and resides away from the minimum energy state. The most popular scenario presents the RFP continually relaxing toward the minimum energy state by coupling power into fluctuations. It has been postulated that the power coupled into fluctuations supplies the energy for the "anomalous" ion heating seen in RFP devices.[23] The ion temperatures recorded in RFPs are large compared to what one would expect from classical electron-ion collisional equipartition.[9,23] If indeed the energy pumped into fluctuations is coupled efficiently to the ion heating, then increasing the fluctuations in an RFP simply increases the total energy content of the plasma and thus the energy confinement time does not degrade. Data from ZT-40M indicate that this is the case.[9]

There is evidence that $\eta_m^k$ provides a reasonable estimate of the resistivity, at least for certain modes of operation of an RFP, usually characterized by fairly low values of $I_p/N$.[18,19] However, in HBTX1B, even at fairly low $I_p/N$, $\eta_m^k$ is substantially larger than the Spitzer value $\eta_{sp}$, even when



the spectroscopic $Z_{eff}$ is included in the calculation of $\eta_{sp}$.[7] It has been postulated that this extra, non-Spitzer, component of the loop voltage is independent of temperature and current, but depends on the intersection of field lines with material surfaces such as walls or limiters.[7] The dependence of plasma resistance on field errors and plasma column centering in HBTX is taken to be evidence for this point of view. The specific explanation has to do with helicity loss at the edge of the plasma. These models have been tested by inserting movable limiters into the plasma edge and comparing the rise in loop voltage to that predicted by the models. The models have been at least partially successful in explaining the observed phenomena, particularly in high temperature discharges in a low-field error magnetic geometry where any non-Spitzer component of the loop voltage would be highlighted.[7]

A 3D MHD computer code was used by Ho, Prager, and Schnack to study the nonlinear behavior of the RFP with nonideal boundary conditions.[24] This code was used to simulate loop voltage versus vacuum region thickness at constant theta. (Vacuum region is the space between the boundary of the plasma and the conducting wall.) Loop voltage rose as the vacuum region thickness was increased; the rise in loop voltage became dramatic when the vacuum region thickness became larger than ~33% of the plasma minor

radius. An evident explanation of the rise in loop voltage caused by the insertion of limiters into the plasma may be simply that such limiters form a vacuum region at the edge of the plasma, thereby moving the plasma boundary away from the conducting wall.

These computational results can be interpreted in terms of conservation of magnetic helicity. Helicity balance requires that injected helicity ($V_\ell \Phi$) balance the plasma dissipation and surface losses. The computational results suggest that the increased helicity input is lost at the surface of the plasma.[24] The fluctuation-induced electric field ($E_f$) is the actual mechanism that causes the rise in $V_\ell$; the vacuum induces instability that causes $E_f$ (and thus $V_\ell$) to rise.

It has become apparent in the past few years that edge plasma conditions play an important role in the determination of global RFP parameters. An alternative explanation of the edge phenomena covered above was proposed in the context of the nonlocal kinetic dynamo theory (KDT).[22] This model proposes, in contrast to a strictly MHD-based model, that there is net electron momentum transfer to the wall. This implies a difference in the total power carried to the wall and limiters by electrons moving parallel to $\underline{B}$ and antiparallel to $\underline{B}$.[22] The edge helicity dissipation models imply no such difference. An electron flux asymmetry has



been observed in the edge plasma of an RFP, thus giving support to the KDT model. The magnitude of the effect of this electron energy loss channel on the energy confinement time $\tau_E$ is not yet clear.

As should be coming clear at this point, the energy (and particle) confinement picture of an RFP is complex. It is as if the RFP were one giant feedback mechanism, with electron dynamics influencing phenomena observed at the plasma edge which in turn is connected to the global parameters and to the relaxation of the plasma which in turn influences ion heating ••• and so on. References to the anomalous resistivity of an RFP (and other observed phenomena) can only be understood within and as part of the total RFP confinement picture. The global parameters exhibited by an RFP are simply signposts to an understanding of the underlying physical process that determine the confinement characteristics of the RFP.

C) Scaling of energy confinement time

Knowledge of the scaling of $\tau_E$ to higher plasma currents is crucial to the development of an RFP fusion reactor. Not enough data have been taken to empirically establish this scaling, nor has there been an unequivocally convincing theoretical estimate given. The starting point of this discussion must then be a comparison of $\tau_E$ experimentally

obtained to that predicted by classical (or neoclassical) ion thermal conduction.

Classically, the dominant contribution to the thermal conductivity of a plasma with density and temperature gradients is from ion-ion collisions.[25] The amount of energy transported by ion-ion collisions is much larger than that transported by electron-electron or ion-electron collisions because the thermal conductivity is proportional to $(\Delta x)^2/\Delta t$, where $\Delta x$ is the mean spatial step caused by the collision and $\Delta t$ is the mean step time (one over the collision frequency). The spatial step size is proportional to the particle gyroradius, which is much larger for the ions.

DiMarco calculated the $\tau_E$ expected from classical thermal conductivity to be[26]

$$\tau_E \text{ (classical)} = 1.6 \frac{\beta_\theta{}^{1/2} I_p{}^3}{n_e{}^{3/2} a Z_{eff} \ell n \Lambda} \text{ seconds} \quad (V.27)$$

where $I_p$ is in MA, $n_e$ is in $10^{20}$ $m^{-3}$, and a is in meters. Taking $\ell n \Lambda = 16$, $Z_{eff} = 1$, and $\beta_\theta = 0.1$ gives

$$\tau_E \text{ (classical)} = 32 \frac{I_p{}^3}{n_e{}^{3/2} a} \text{ milliseconds} \quad (V.28)$$



where all units are as previously stated. This is in contrast to a scaling fit of present data where[26]

$$\tau_E \text{ (fit)} = 1.7 \frac{I_p{}^3}{n_e{}^{3/2} a} \text{ milliseconds} \quad . \quad (V.29)$$

This factor of twenty difference between $\tau_E$ (classical) and $\tau_E$ (fit) agrees with other estimates.[15,27] Excluding the energy lost via radiation and including a realistic $Z_{eff} \cong 2.5$ reduces the difference between $\tau_E$ (classical) and $\tau_E$ (fit) to less than ten.[26] If $\tau_E$ does indeed scale proportional to $I_p{}^3/(n_e{}^{3/2} a)$, then this order of magnitude difference in the proportionality constant suggested by classical ion thermal transport and that suggested by empirical fit is not a serious strike against an RFP fusion reactor. In fact, such scaling suggests that an RFP fusion reactor is indeed practical and possible. However, the current data base is not extensive enough to confirm or deny the possibility that $\tau_E \propto I_p{}^3/(n_e{}^{3/2} a)$. Data from the MST (particularly data that will be taken after the primary winding upgrade) will cover a range of operating parameters that is between present generation RFP machines (ETA-BETA II, HBTX, and TPE-1RM(15)) and the next generation devices (RFX

and ZTH). MST data will provide important tests of proposed scalings.

One of the most well-known scalings of $\tau_E$ is due to Connor and Taylor.[28] Their scaling is based on the supposition that energy confinement is limited by electron energy transport due to resistive fluid turbulence. This theory implies that all ohmically heated RFP devices should reach a value of $\beta_\theta$ given by

$$\beta_\theta \cong \left(\frac{m_e}{m_p}\right)^{1/6} \cong 30\% \ . \qquad (V.30)$$

(Thus the reason why this theory is often referred to as "constant $\beta_\theta$ scaling.") The electron temperature should also exhibit a specific dependence, namely

$$T_e \propto I_p \left(\frac{I_p}{N}\right) \ . \qquad (V.31)$$

These two results are included in the prediction for energy confinement time, which is[26]

$$\tau_E \propto \frac{I_p^3}{n^{3/2} a Z_{eff}} \ . \qquad (V.32)$$



This is the same dependence as given by classical ion thermal transport; as $\beta_\theta$ approaches unity the electron heat transport due to resistive turbulence in an RFP approaches classical ion transport.[28]

Ortolani has introduced a viewpoint that is useful when evaluating scaling data,[15,23] especially in light of a constant $\beta_\theta$ hypothesis. Typically, the values of $\tau_E$ and $\beta_\theta$ reported and used for comparison to scaling laws are the maximums obtained. These maximums are generally achieved after machine optimization and usually at the highest density consistent with burning through the radiation barrier.[23,26] This means operation near the high density limit of an RFP, which can be expressed as[15]

$$\frac{I_p}{N} \gtrsim 10^{-14} \text{ amp-meter} \ . \qquad (V.33)$$

The definition of $\beta_\theta$ can be rearranged to give

$$T \propto \beta_\theta \left(\frac{I_p}{N}\right) I_p \ . \qquad (V.34)$$

Now, by observing that maximum values of $\tau_E$ and $\beta_\theta$ occur for a value of $I_p/N$ that is nearly the same for all RFP devices, we see that[15]

$$T \propto \beta_\theta I_p \qquad (V.35)$$

and

$$\tau_E \propto a^2 \beta_\theta^{5/2} I_p^{3/2} \quad . \qquad (V.36)$$

In light of this the important question becomes the scaling of $\beta_\theta$ with plasma current. Experimental data suggest a weak dependence of $\beta_\theta$ on $I_p$; the usual case is a slow decline of $\beta_\theta$ as $I_p$ is increased.[7,16]

The theory of Connor and Taylor predicts that all RFP devices should reach a similar value of $\beta_\theta$ so long as radiation is a minor energy loss mechanism.[28] This is not a serious constraint; however, data from ZT-40M suggest that $\beta_\theta$ is approximately constant even as the fraction of ohmic power radiated is increased from 15% to 95%.[29] These data imply that energy transport processes in the RFP decrease to compensate for an increase of radiation so that a constant $\beta_\theta$ is maintained. $\tau_E$ did decrease as the radiative fraction was increased, however, this was simply the effect of the increase of $Z_{eff}$ (and the plasma resistance) as the plasma was doped with increasing amounts of strongly radiating krypton. The calculations of Pickrell et al.[29] indicate that the non-radiative energy confinement time increased by an order of magnitude in order to compensate for the drop in



radiative confinement time as the radiative fraction was increased.

We do not know what the important non-radiative energy transport processes are in an RFP plasma. One of the most intriguing recent experimental discoveries has been the existence of a substantial population of suprathermal ($T_e \approx 2\ T_{eo}$, not runaway) electrons streaming along the edge of the RFP.[30] These electrons seem to carry a substantial fraction of the local plasma current and may be responsible for most of the energy deposited on the wall and limiters. If these suprathermal electrons are an important energy loss channel, then their behavior during the radiative energy loss experiment described above should be monitored. This experiment has apparently not yet been done at ZT-40M, although a similar experiment was performed on ZETA (a large toroidal pinch of dimensions comparable to MST) in the early 1960's. An electrostatic energy analyzer (of the same type used to discover the suprathermal electrons) was inserted into the edge plasma of ZETA.[31] The electron densities in the edge were greater than $10^{13}$ $cm^{-3}$. With the energy analyzer pointing downstream of the local electron drift velocity along the local magnetic field lines, electron temperatures of 30 eV to 50 eV were recorded during discharges where radiation losses were small. These temperatures fell to $\leq$ 10 eV when fractional amounts of argon

were added to the discharge in order to increase the radiative energy loss. Electron density in the edge remained roughly constant as argon was added in increasing fractions. It appears that radiative energy loss and edge electron energy loss are in an inverse relationship.

There is one further observation from ZETA that is of interest. When the electron energy analyzer was pointed upstream of the local electron drift velocity, a non-thermal tail of the electron energy distribution was observed. These may have been runaway electrons since they were present only in discharges with a low initial fill gas pressure.

As the above data and theory indicate, the mechanisms that govern energy transport (and thus energy confinement) of an RFP plasma are not understood. In order for the RFP to be considered as a viable candidate for a fusion reactor, it is vitally important to understand the physical processes that determine its energy confinement properties. But the RFP is more than just an engineering problem, it is an intricate, intrinsically beautiful structure that we have only begun to appreciate and visualize.



## References


[1] J.C. Sprott, Phys. Fluids 31 (8), 2266 (1988).

[2] J.C. Sprott and E.W. Goetz, University of Wisconsin-Madison PLP 1039 (1988).

[3] J.S. Sarff, private communication.

[4] S.A. Hokin, R.N. Dexter, and E. Scime, Abstract submitted for the 31st Annual Meeting of the Division of Plasma Physics-American Physical Society (Anaheim, 1989).

[5] H. Dreicer, Physica Scripta T2/2, 435 (1982).

[6] B. Alper et al., 16th IEEE International Conference on Plasma Science (Buffalo, 1989), Poster 2P47.

[7] H.A.B. Bodin, in "Proceedings of the International School of Plasma Physics," Varenna, 1987 (Società Italiana di Fisica, Bologna, 1988), Vol. I, p. 307.

[8] Y. Nagayama et al., 16th IEEE International Conference on Plasma Science (Buffalo, 1989), Poster 2P48.

[9] P.G. Weber et al., 16th IEEE International Conference on Plasma Science (Buffalo, 1989), Poster 2P50.

[10] T. Rempel, private communication.

[11] M. Bassan, F. Flora, and L. Giudicotti, in "Proceedings of the International School of Plasma Physics," Varenna, 1987 (Società Italiana di Fisica, Bologna, 1988), Vol. III, p. 1035.

[12] H.A.B. Bodin and D.E. Evans, Nucl. Fusion 25 (9), 1305 (1985).

[13] L. Spitzer and R. Härm, Physical Review 89 (5), 977 (1953).

[14] I.H. Hutchinson, Principles of Plasma Diagnostics, (Cambridge University Press, Cambridge, 1987), p. 18.

[15] S. Ortolani and G. Rostagni, Nucl. Instrum. and Methods 207, 35 (1983).

[16]B. Alper, S. Martini, and S. Ortolani, Nucl. Fusion 26 (9), 1256 (1986).

[17]H.A.B. Bodin in "Proceedings of the International School of Plasma Physics," Varenna, 1987 (Società Italiana di Fisica, Bologna, 1988), Vol. I, p. 3.

[18]L. Gabellieri et al., Nucl. Fusion 27 (5), 863 (1987).

[19]P.G. Weber, Phys. Fluids 28 (10), 3136 (1985).

[20]K.F. Schoenberg, R.W. Moses, and R.L. Hagenson, Phys. Fluids 27 (7), 1671 (1984).

[21]H.Y.W. Tsui, A.A. Newton, and M.G. Rusbridge, Culham Laboratory Memorandum, CLM-M110 (1987).

[22]R.W. Moses, K.F. Schoenberg, and D.A. Baker, Phys. Fluids 31 (10), 3152 (1988).

[23]S. Ortolani, "16th European Conference on Controlled Fusion and Plasma Physics," Venice, 1989.

[24]Y.L. Ho, S.C. Prager, and D.D. Schnack, Phys. Rev. Letters 62 (13), 1504 (1989).

[25]M.N. Rosenbluth and A.N. Kaufman, Physical Review 109 (1), 1 (1958).

[26]J.N. DiMarco, Los Alamos National Laboratory LA-UR-Revised-88-3375 (1989).

[27]H.A.B. Bodin, Nucl. Instrum. and Methods 207, 1 (1983).

[28]J.W. Connor and J.B. Taylor, Phys. Fluids 27 (11), 2676 (1984).

[29]M.M. Pickrell et al., Los Alamos National Laboratory report, "Evidence for Poloidal Beta Limited Confinement on the ZT-40M Reversed Field Pinch" (1989).

[30]R. Ellis, J.C. Ingraham, P.G. Noonan, and H.Y.W. Tsui, Bull. Am. Phys. Soc. 33 (9) 1999 (1988).

[31]A. Gibson and D.W. Mason, Proc. Phys. Soc. 79, 326 (1962).



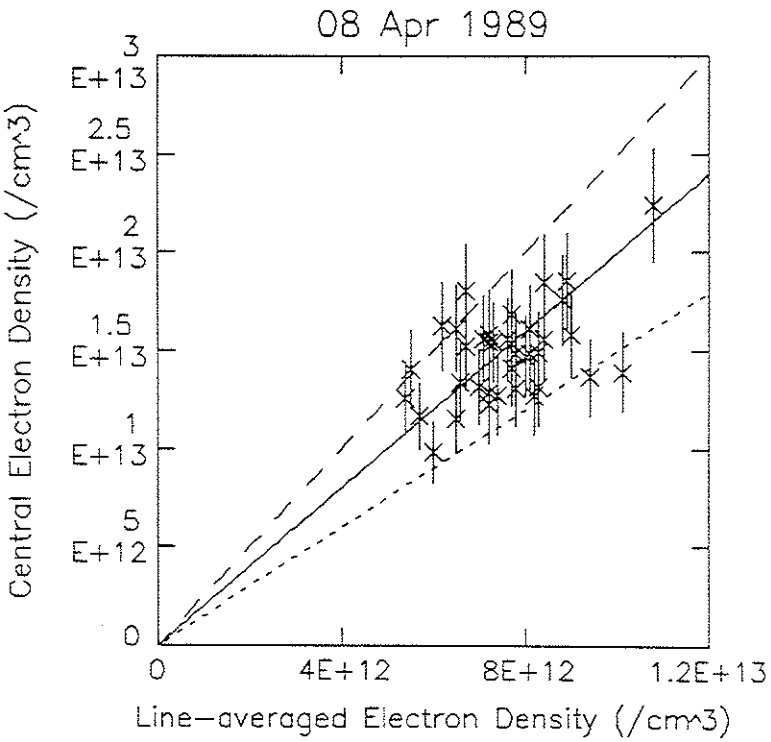


Figure V.1: Thomson scattered central electron density versus microwave interferometer line-averaged electron density from a group of about thirty 08 April 1989 RFP discharges.

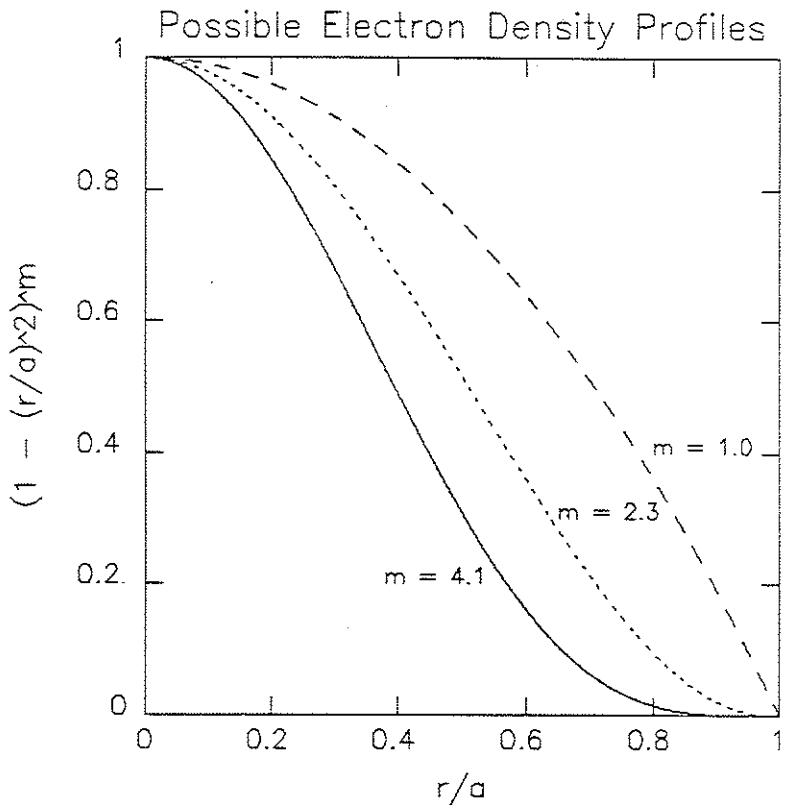


Figure V.2: Possible MST electron density profiles of the form $n_e(r) = n_{eo}[1 - (r/a)^2]^{\alpha}$.



## CHAPTER VI: THE MST PLASMA

Results of experiments performed on the MST RFP are presented in this chapter. The Thomson scattering diagnostic played a major role in all of these experiments. It, however, provided a limited amount of information, namely a local measurement of central electron temperature and density at a single time point during the discharge. Extrapolation of this local measurement to global characterization of a particular discharge must be done with caution. As was shown in the previous chapter, there is a negligible amount of profile information available for MST. The assumption is normally made that large profile changes do not take place when a parameter such as plasma current is varied or when a perturbation such as a doping gas is introduced into the discharges. If this assumption is valid, then a $\tau_E$ or a $\beta_\theta$ derived from a local measurement is meaningful. If it is not, then much of this work (and most of the experimental work done on RFP's) is of limited use.

There were, of course, many diagnostics besides Thomson scattering available on MST. These were introduced in Chapter III; the reader should be aware of the limitations of all the experimental apparatus as the emphasis below will be placed upon the presentation of experimental results.

The goal of a large part of this chapter is the development of an understanding of the processes and mechanisms that determine MST energy confinement. This will be done with a coherent and internally consistent presentation of the energy loss of MST as seen by the diagnostics that were available when this work was done. It is hoped that the whole will prove greater than the sum of the parts.

A) Electron temperature and density fluctuations

Figures VI.1, VI.2, and VI.3 present central electron temperature and density data taken with the Thomson scattering diagnostic over the course of an entire day. (Central energy density is the $n_eT_e$ product.) As can be seen from Figure VI.2, the density was drifting upward over the course of the day (mainly because it is extremely difficult to effectively control the density of hydrogen-fueled discharges), but all other controllable parameters were held constant throughout the run. In particular, note that even though $n_e$ was drifting up and $T_e$ was drifting down, the $n_eT_e$ product was stable. Since the plasma current was held constant at 440 kA to within a few percent, this implies that poloidal beta was constant throughout this series. An outstanding feature of these three figures is the amount of scatter in the data points. This observation drove an



investigation to determine the cause of this scatter, the results of which are presented below.

The initial examination of this data concentrated on a search for evidence of any correlation between the fluctuations in $T_e$ and $n_e$ and the fluctuations in certain macroscopic discharge parameters. The most striking of such phenomena are sawtooth-like oscillations in the soft x-ray signal, average toroidal field and toroidal field at the wall, and line-averaged electron density. The last two parameters are graphed in Figures VI.4 and VI.5 for a 16 February 1989 discharge. The drop in line-averaged density is well-correlated with the drop in $B_T$ at the wall. Therefore, the $B_T$ at the wall signal can be used as a time marker to tell when the line-averaged density is at its lowest point.

On 4 February 1989, the day the data in Figures VI.1, IV.2, and VI.3 were taken the interferometer was not functional. However, the sawtooth-like oscillations were clearly visible on the soft x-ray and $B_T$ at the wall signals (see Figures VI.6 and VI.7). Since the phase of these oscillations is random and the Thomson scattering laser was fired at a specific time point during the discharge, it was inevitable that some of the $T_e$ and $n_e$ data were taken when $B_T$ at the wall (and presumably the line-averaged density) was at or near a minimum. Such points are marked by triangles in

Figure VI.1, VI.2, and VI.3. These temperature, density, and energy density points seem to be as randomly distributed as the remaining, suggesting that there is no correlation with the drop in line-averaged density or the drop in the soft x-ray signal.

Other attempts to establish a correlation of MST $T_e$ and $n_e$ with the phase of the sawtooth-like oscillation have also yielded a null result. At this point, we have been forced to conclude that the central temperature, density, and energy density of MST do not vary reproducibly during the sawtooth-like oscillations evident in other parameters. This implies that the observed drop in line-averaged density is simply a steepening of the density profile; only edge density is lost during the drop. The drop in line-averaged density, coupled with the observation that central $T_e$ and $n_e$ do not appear to vary, does indicate that global energy confinement does degrade during a sawtooth-like oscillation. Detailed profile information would be necessary in order to make a quantitative statement about the drop in global confinement.

Results from the ZT-40 RFP indicate that the central $n_eT_e$ product does vary reproducibly during a sawtooth-like oscillation.[1] The minimum of the central energy density occurs at the same time as the minimum in the soft x-ray signal. The variation in $n_eT_e$ is about 50% of the peak value of $n_eT_e$ and indicates that $n_eT_e$ recovers to its peak value



much more quickly than the soft x-ray signal. Data from MST quite conclusively rule out such a large variation in the $n_eT_e$ product; further studies need to be made to determine the variation, if any, in the MST central $n_eT_e$ product.

Having investigated what appeared to be the most likely physical cause (or effect) of the $T_e$ and $n_e$ fluctuations, we looked more closely at the statistical uncertainties associated with each data point. In order to accomplish this task in the most unbiased manner possible, a subset of the 4 February 1989 data was selected for examination. Figures VI.8 and VI.9 present this data. The discharges in this set were macroscopically similar to within a few percent for every parameter monitored except $T_e$ and $n_e$. Given that these were reproducible discharges we must ask if the scatter in the data points is representative of true local fluctuations in the temperature and density or if the scatter simply arose from the statistical deviations expected from measurements which have uncertainties determined by Poisson statistics.

If the data points are simply distributed normally around a mean, then the distribution can be characterized by the mean and standard deviation. Approximately two-thirds of the data points should lie within one standard deviation of the mean. The uncertainty associated with each data point is an estimate of its probable deviation from the actual value of the parameter being measured. There is a probability of

approximately two-thirds that the measured value differs from the actual value by no more than plus or minus the uncertainty. Then, if we assume that the mean of the data points is representative of the actual value of the parameter being measured, we can assume that the standard deviation and the average uncertainty should be of comparable magnitude if the scatter in the data points is simply representative of the measurement uncertainty.

Refer once again to Figures VI.8 and VI.9 where electron temperature and density data are graphed versus shot number for a set of 44 nearly identical discharges. Statistical analysis of the data gives the following information:

$$\text{Average}\left(\frac{\text{temperature uncertainty}}{\text{temperature}}\right) = 0.24 \qquad \text{(VI.1)}$$

$$\frac{\text{Standard deviation of temperature}}{\text{Mean Temperature}} = 0.28 \qquad \text{(VI.2)}$$

and

$$\text{Average}\left(\frac{\text{density uncertainty}}{\text{density}}\right) = 0.10 \qquad \text{(VI.3)}$$



$$\frac{\text{Standard deviation of density}}{\text{Mean density}} = 0.13 \qquad \text{(VI.4)}$$

where "uncertainty" refers to the "error bar" associated with each individual point and standard deviation is, as usual, the square root of the variance of the set of 44 data points. Comparison of Eq. (VI.2) with Eq. (VI.1) and Eq. (VI.4) with Eq. (VI.3) shows that the scatter of the actual data points is only a few percent larger than that which would be expected from the scatter induced by the inherent uncertainty of the measurement technique. (Density has been quoted in arbitrary units in this section because conversion to absolute units adds an absolute uncertainty onto the error bars. This additional uncertainty is not associated with the statistical limitations of the measurement technique and would cloud the issue if it were present.) It is reasonable to conclude that the central electron temperature and density fluctuations in MST are no larger than a few percent of the mean values.

This result is substantially different from that obtained from a fluctuation analysis of the electron temperature and density data taken on ETA-BETA II.[3] Series of macroscopically identical discharges produced sets of electron temperature and density data with far more scatter than could be accounted for by measurement uncertainty. They

attributed this additional scatter in the data points to actual local fluctuations of the temperature and density. The rms amplitude of the temperature fluctuations in the plasma was about 22%, density fluctuation amplitude was slightly smaller. Results of an analysis of the correlation between temperature and density were not reported.

At the present time we have no explanation for the large difference in fluctuation levels exhibited by ETA-BETA II and MST. Measurement uncertainties are not, of course, exactly known in either case, but adjustments in these uncertainties could only account for a small fraction of the difference in fluctuation amplitude. This avenue of experiment must be further pursued on MST in order to determine the fluctuation magnitude and spectrum and to examine correlation between temperature and density fluctuations.

Careful examination of the data graphed in Figure VI.8 revealed that the individual temperature points are not quite normally distributed around the mean temperature. The distribution is slightly skewed toward higher temperatures. This is an artifact of the linear least-squares fitting routine used to analyze the raw Thomson scattering data. The slope (which is proportional to the temperature) of the line fit to the raw data is unduly influenced by the number of counts in the wavelength channel farthest from the laser line. In order to determine the size of this problem, a



nonlinear least-squares fitting routine was used to analyze this same set of data. The results are shown in Figure VI.10. The distribution of individual points around the mean is closer to a normal distribution, although the difference from Figure VI.8 is not striking. (The nonlinear routine indicated that shots 23 and 28 were poor quality fits and should be disregarded.) Analysis of all shots except 23 and 28 gave

$$\text{Average}\left(\frac{\text{temperature uncertainty}}{\text{temperature}}\right) = 0.26 \qquad \text{(VI.5)}$$

$$\frac{\text{Standard deviation of temperature}}{\text{Mean temperature}} = 0.23 \quad . \qquad \text{(VI.6)}$$

These results are similar to those from Figure VI.8. The density from the nonlinear routine is even less distinctive than the temperature data and is not presented here. Although the two routines did occasionally return substantially different estimates of the temperature for a given shot, the weighted mean temperatures from the two analyses (disregarding shots 23 and 28) differ by only seven percent, the higher mean coming from the linear fitting routine.

The upshot of this matter lies in the observation that the temperature estimates from the linear least-squares fitting routine cannot be used to support conclusions about the specific distribution of the individual temperature points. However, these temperature estimates do reveal changes (or the lack thereof) in the electron temperature as other plasma parameters are varied. Since all of the experiments described below are of this nature, it was not deemed necessary to re-analyze the raw data that had already been fit with the linear fitting routine. Be aware, then, that all the temperature and density estimates presented in this thesis (except those in Figure VI.10) come from a least-squares linear fit. Further development of this diagnostic should include the implementation of a data analysis procedure that uses a statistically robust nonlinear fitting routine.[2]

B) Experimental approach to energy confinement

The experiments described below were not designed just to determine or optimize the energy confinement of the MST RFP. They were executed in pursuit of an understanding of the mechanisms which determine the energy confinement characteristics of the RFP. To this end, the discussion below concentrates on a determination of the means whereby energy escapes from the MST plasma (the "energy loss



channels") and the relative importance of each of these processes. The energy confinement time $\tau_E$ is not the most convenient quantity with which to describe the energy loss mechanisms of the RFP. The inverse of $\tau_E$, the energy loss rate $\nu_E$, is easier to manipulate because it can be thought of as

$$\nu_E = \frac{\sum_i P_i}{n_e T_e \cdot \text{Volume}} \qquad \text{(VI.7)}$$

where $P_i$ is the power flowing out through the $i^{th}$ energy loss channel. An equivalent definition is

$$\nu_E = \sum_i \nu_i \qquad \text{(VI.8)}$$

where $\nu_i$ is the energy loss rate due to the $i^{th}$ loss channel. With this definition it is easier to describe the relative magnitude of each of the loss mechanisms.

The following discussions will show that important RFP energy loss channels appear to be

a) electron thermal transport from stochastic magnetic fields

b) radiative energy loss

c) escape of particles from the plasma.

Using simplifying assumptions it is possible to separate these channels using results from the diagnostics that were available on MST during the spring of 1989 and the previously discussed assumptions of symmetry and profile invariance. Some of the specific numbers and percentages given below are subject to question because of the assumptions that have been made in order to allow interpretation of the raw data. In addition, statement c) above has been left deliberately vague because there was no way to differentiate between neutral particle loss and anomalous loss of charged particles. However, the supposition will remain that the energy loss mechanisms discussed below are indeed major energy loss channels of the MST RFP plasma.

Chapter V of this thesis contained a lengthy discussion of the anomalous character of the RFP loop voltage. In the discussion below it will become apparent that variations of the loop voltage are indeed the key element behind variations of the energy loss rate which is, of course, directly proportional to the loop voltage:

$$\nu_E \propto \frac{V_\ell I_p}{n_e T_e \cdot \text{Volume}} \quad . \qquad \text{(VI.9)}$$



In all of the perturbation experiments described below the peak plasma current did not vary substantially and some mechanism within the plasma held the energy density $n_e T_e$ roughly constant. The variations in the energy loss rate $\nu_E$ are almost entirely correlated with variation in $V_\ell$. One useful way of interpreting the data from these experiments, then, is to use the results from the Thomson scattering diagnostic to establish the approximate constancy of the $n_e T_e$ product and then to concentrate on changes in $V_\ell$ associated with changes in magnetic fluctuation level or bolometer signal. In fact, as will be suggested, it may be possible to break down the anomalous (non-Spitzer) portion of the loop voltage into parts associated with each of the energy loss mechanisms. Also note that during each of the perturbation series poloidal beta was approximately constant. This was observed because $T_e$, $n_e$, and $I_p$ were all individually constant during each series.

C) F-scan experiment

The results of the 30 March 1989 F-scan experiment will be examined first because they help to illuminate results from other experiments. During this experiment the toroidal field reversal parameter, F, was scanned from -0.3 to +0.3. The pinch parameter $\theta$ was held approximately constant only for $F < 0$ (see Figure VI.11). Theta was held constant by

varying the amount of energy stored in the poloidal field capacitor bank, however, $I_p$ was not varied by more than 15% (Figure VI.12).

One of the striking aspects of the raw data from this experiment is the variation in edge magnetic fluctuation level ($\tilde{B}/B$) with F (Figure VI.13). ($\tilde{B}/B$ was read from a set of edge magnetic coils at a toroidal angle of $180^{\circ}$ and a poloidal azimuth of $61^{\circ}$.) The fluctuation level is nearly constant for $F < 0$, rising sharply as F becomes more positive. The same data plotted versus $\theta$ (Figure VI.14) shows a monotonic decrease in fluctuation level as $\theta$ approaches 1.6 to 1.7. The toroidal pinch may be most stable in this range of $\theta$ values.

The above speculation is, however, only secondary to the purpose at hand. During the discussions immediately below, attention will be focussed on the group of shots for which $F < 0$. (These have been and will be represented on the graphs by triangles; the $F > 0$ shots will be represented by crosses.) Since $\tilde{B}/B$ did not change for the $F < 0$ series, it seems reasonable to assume that the part of the energy loss rate due to magnetic fluctuations also did not change. However, the part of $\nu_E$ due to radiation and particle loss did change over this series. The bolometer, which integrates this loss channel over the entire discharge, showed wide variation over the $F < 0$ series (Figure VI.15). The cause of



the scatter in the data points for $F < 0.1$ is not known, however, a similar scatter is seen in the heating power and the loop voltage for $F < -0.1$. (See Figures VI.16 and VI.17.) In fact, both the heating power ($V_\ell I_p$) and loop voltage ($V_\ell$) track the bolometer signal with what appear to be linear relationships (Figures VI.18 and VI.19). Extrapolation of the bolometer signal back to zero (which represents a discharge in which no energy is lost via particles or radiation) gives a heating power of 5.3 MW and a loop voltage of 16 volts. It is not a large leap then to postulate that about 35% of the input heating power of standard $F = -0.1$ discharge is lost via radiation or particle loss. Since neither plasma current nor the energy density of the plasma varied substantially during this series (the second condition will be justified below), it seems reasonable to postulate that the increase in the rate at which energy flowed out of the plasma is correlated with the increase in $V_\ell$. Lower loop voltage appears to be indicative of less power flowing out of the plasma.

There are a few points concerning the performance of the bolometer that need to be discussed before proceeding further. The bolometer is sensitive to energy leaving the plasma via particles or radiation. In order to break this energy loss channel down into its two components (as will be done later), there is available a signal proportional to the

amount of VUV radiation coming out of the plasma. This is the VUV impurity signal and was integrated over the whole of the discharge just as the bolometer was. The VUV impurity signals from the $F < 0$ series are graphed versus the bolometer signals in Figure VI.20. The relationship between the two signals is not apparent from this figure; although both seem to increase together. The relationship will be clarified below in the section covering the argon doping experiments.

Since the bolometer integrates energy loss from the plasma over the entire discharge, it is reasonable to compare it to the amount of energy that goes into the plasma, $V_\ell \cdot I_p \cdot$ time. This calculation cannot be made for the entire discharge for the data presented in this thesis because the plasma current and loop voltage were not available during the last third of most discharges. The best that can be done is to integrate the quantity $V_\ell \cdot I_p$ for the first 20 milliseconds of the discharge. This figure, called "heating energy," is plotted versus bolometer signal for the $F < 0$ series (Figure VI.21). There again appears to be a monotonic relationship between the two quantities, although it is not as clearly linear as that between the bolometer signal and heating power at the plasma current peak (Figure VI.19). The reasons for this behavior are not known, although the sensitivity of the $V_\ell$ and $I_p$ calculations to



time derivatives during the ramp-up phase of the discharge may be part of the explanation. In any case, this result should not dissuade us from believing that, during this series of shots, the discharge integrated bolometer signal was approximately proportional to the particle and radiative energy loss channels at the plasma current peak.

As a final exhibition of the fact that plasma current did not vary substantially or monotonically during the $F < 0$ series, Figure VI.22 is a plot of $I_p$ versus bolometer signal. Plasma current did not exhibit the regular variation that is apparent from the loop voltage versus bolometer signal graph.

Previously it was stated that the energy density of the plasma remained approximately constant during the $F < 0$ series. Figure VI.23 is a graph of the $n_e T_e$ product versus the bolometer signal. The uncertainties associated with each individual datum make it difficult to discuss any trend. However, there do appear to be two distinct groups of points, one with bolometer signals below 0.8 arbitrary units and the other with signals above this point. The weighted means of these two groups are $3.1 \times 10^{15}$ eV/cm$^3$ and $3.4 \times 10^{15}$ eV/cm$^3$, respectively. This 10% difference is insubstantial in light of the nearly 40% variation in $V_\ell$ for the same series.

In light of the fact that neither the energy density nor the plasma current varied during this series, it is reasonable to expect poloidal beta to remain constant. This

is apparently the case, (see Figure VI.24), although there may be a slight positive trend at high bolometer readings.

The other confinement quantity of interest is the energy loss rate, $\nu_E$. This quantity should follow the same trend versus bolometer signal that loop voltage does. However, as can be seen from Figure VI.25, the uncertainties eliminate the possibility of making a definitive statement, although $\nu_E$ does appear to trend upward with increasing bolometer signal.

It is clearly impossible, in light of the uncertainties associated with $\nu_E$, to directly infer a relationship between the bolometer signal and the particle/radiation energy loss rate. But, with reference to the constancy of plasma current and energy density during this series, it is reasonable to assume that the energy loss rate from particles and radiation is directly proportional to $V_\ell$. Return again to Figure VI.18. The slope of the line is 19 volts/bolometer unit. (Or, alternatively from Figure VI.19, the slope is 4.4 MW/bolometer unit.) Now, during the $F > 0$ series, both the magnetic fluctuation level and the bolometer signal changed as F was varied (Figure VI.26). However, since we have postulated a relationship between $V_\ell$ (or heating power) and the bolometer signal, the effect of the particle and radiation loss channel may be subtracted from the $F > 0$ data. This was done for Figures VI.27 and VI.28; the results of course, are similar. There does appear to be a relationship



between $(\tilde{B}/B)^2$ and $V_\ell$ (or heating power). However, because some of the increase in $(\tilde{B}/B)$ is probably due to plasma motion and not to field line reconnection, a specific relationship will not be derived. The next section contains more applicable and controlled results, namely, an $F = -0.1$ series where $(\tilde{B}/B)$ was varied. As a final note, however, refer to Figure VI.29, where it is obvious that, for the $F > 0$ series, the energy loss rate did rise as $(\tilde{B}/B)^2$ increased.

D) Paddle insertion experiment

A graphite paddle limiter was inserted into the edge of the MST plasma at a toroidal angle of $138^\circ$ and a poloidal azimuth of $19^\circ$. Dimensions of the paddle were 75 x 150 x 6 millimeters, the 75 mm edge was parallel to the toroidal axis. Paddle insertion experiments were done in both hydrogen and helium plasmas in order to examine the effects of limiter insertion on energy confinement parameters. The experiment done with the hydrogen plasmas showed large changes in the electron density as the paddle was inserted and removed over a series of shots. Apparently the graphite paddle was acting as a source and sink of hydrogen during the discharge. This perturbation of the density (which was difficult to control because it exhibited a fair amount of hysteresis) obscured the more subtle changes in the other

global parameters associated with energy confinement. Therefore, the results presented below are solely from a paddle insertion experiment done in helium plasmas on 08 April 1989. The general behavior exhibited by the plasma on this date has been confirmed by the results of several other paddle insertion experiments. Insertion of the paddle into the helium plasmas caused very little change in the electron density, as is shown in Figure VI.30. Variations in other parameters, such as loop voltage, were clear and tractable.

In order to clarify trends and patterns in the Thomson scattered derived data, uncertainty weighted averages of certain groups of points will be plotted. For the paddle insertion experiment, this means a weighted average of four data points at each of the four insertion positions. The weighted averages and associated uncertainties were calculated according to the method of Bevington.[4] This averaging technique is appropriate if the scatter of the data points is approximately Gaussian; that this is so has been shown earlier in this chapter. An example of this technique is shown in Figure VI.31. This figure is the analog of Figure VI.30 and clarifies the results contained in that figure.

The central electron temperature exhibited a similar lack of variation as the paddle was inserted. In fact, within the uncertainties, the temperature remained constant



at about 275 eV. (See Figure VI.32.) However, the time integrated (over the entire discharge) central chord soft x-ray signal did decrease as the paddle was inserted. (See Figure VI.33.) This reflects the fact that both the magnitude of the SXR signal and the size of the SXR sawtooth-like oscillations decreased. This behavior may indicate that the SXR signal is generated by energetic electrons in the tail of the distribution and that it does not reflect the bulk $T_e$. The plasma current remained approximately constant, dropping off only slightly as the paddle was inserted. (See Figure VI.34). This is, therefore, a situation where the plasma energy density (temperature and density product) and plasma current (which is proportional to the poloidal magnetic field at the edge) have remained approximately constant. This means that a constant $\beta_\theta$ was observed as the paddle was inserted, a not entirely unexpected result. See Figure VI.35 for plot of $\beta_\theta$ versus paddle insertion.

However, not every parameter remained constant as the paddle was inserted. The loop voltage rose monotonically once the paddle was pushed in past 4 cm (Figure VI.36). This result is similar to that of the HBTX limiter insertion experiments,[5] although they observed the loop voltage to rise as soon as the paddle was inserted into the edge of the plasma. The observation here and in other paddle insertion

experiments on MST that the loop voltage remains constant or slightly decreases as the paddle is introduced into the edge of the plasma engenders speculation about the interaction of the plasma with the wall. However, no firm explanations can be offered at this point.

The energy confinement time, $\tau_E$, reflected the rise of the loop voltage. It appears to be bending downward after the paddle was inserted past 4 cm. (See Figure VI.37.) The change in $\tau_E$ is not substantial, but the trend downward does appear to be real. The energy loss rate $\nu_E$ is graphed in Figure VI.38.

We have in this experiment a plasma which, as the paddle limiter is inserted, does not alter its energy density (see Figure VI.39), yet the power flowing into the plasma is increasing (see Figure VI.40). Therefore, as the paddle is inserted, there must be an increasing flow of power out of the plasma. Neither the VUV impurity signal nor the bolometer signal increased as the paddle was inserted (see Figures VI.41 and VI.42). The remaining obvious alternative is fluctuation-induced thermal transport. This data set contains both edge electrostatic and edge magnetic fluctuation data. Some sort of electrostatic fluctuation-induced transport does not seem likely because the magnitude of the floating potential fluctuations did not change as the paddle was inserted. (See Figures VI.43 and



VI.44 for graphs of the data from the two toroidally separated floating probes.) The magnitude of the magnetic fluctuations, however, did increase as the paddle was inserted. This may indicate that electron thermal transport from stochastic magnetic fields was increasing. This transport theory[6] links thermal transport with radial magnetic field fluctuations in the bulk plasma. We, however, do not have such measurements. The fluctuations have been measured only at the edge, near the wall, where poloidal and toroidal magnetic field fluctuations dominate. There is, however, justification for believing that these measurements are indicative of the radial field fluctuations that are involved in transport.[7] Figure VI.45 is a graph of total magnetic fluctuations at the edge ($\tilde{B}/B$) versus paddle insertion. The set of three coils (measuring $B_R$, $B_P$, and $B_T$) was at a toroidal angle of $180^o$ and a poloidal azimuth of $61^o$. The magnitude of the fluctuations appears to increase almost linearly with paddle insertion once the paddle is beyond a depth of four cm.

The most convenient method of linking magnetic fluctuations and thermal transport is to express an energy loss rate in terms of the magnitude of the fluctuations. We know from the previous discussion that

$$\nu_E = \frac{1}{\tau_E} \qquad \text{(VI.10)}$$

and we define

$$\nu_E = \nu_{EO} + \frac{g}{a^2} X_E \qquad \text{(VI.11)}$$

where

$X_E$ = diffusion coefficient calculated from electron thermal transport due to stochastic magnetic field lines.

$\nu_{EO}$ = loss rate dependent upon transport mechanisms other than those linked to magnetic field fluctuations.

a = minor radius.

g = geometric factor.

The form of the diffusion coefficient is[7]

$$X_E = v_{th} L \left(\frac{\tilde{B}}{B}\right)^2 \qquad \text{(VI.12)}$$

where $v_{th}$ is the thermal velocity of the electrons and L is a characteristic length of the diffusion process. In this model, then, the energy loss rate is directly proportional to the magnitude squared of the magnetic fluctuations. We are implicitly assuming that the magnetic fluctuations are not due to plasma motion, which does not produce stochastic



fields. Reconnection of field lines must be taking place in order to produce stochastic fields and thermal transport. We do not need (and indeed do not have) a specific knowledge of the mechanism that controls the level of magnetic fluctuations in order to interpret our results in terms of this model.

Figure VI.46 is a plot of the energy loss rate $\nu_E$ versus the magnitude squared of the magnetic fluctuations. The energy loss rate does appear to increase linearly with $(\tilde{B}/B)^2$. The intercept $\nu_{EO}$, which is indicative of what the energy loss rate would be in the absence of magnetic fluctuations, is approximately 70% of the energy loss rate of a standard discharge (i.e., when paddle insertion is zero, see Figure VI.38). This means that, in standard MST discharges about 30% of the energy lost from the plasma flows out via a mechanism connected with magnetic fluctuations. Remember that this result may not be realistic if any one of the simplifying assumptions we have made is incorrect.

In this experiment, as in the F-scan experiment, the uncertainties associated with the $\nu_E$ points are so large that specific conclusions such as that above cannot be made too forcefully. But, note again that in this experiment, as in the F-scan experiment, the loop voltage (or heating power) is the only quantity that exhibited a strong variation as the paddle was inserted and magnetic fluctuations increased.

The $F < 0$ series of the F-scan provided information about the relationship between the particle and radiation energy loss channel (represented by the bolometer signal) and the loop voltage (or heating power). However, because this paddle insertion data set was taken at a different plasma current, only the relationship between the heating power and the bolometer signal is applicable. Subtracting the particle and radiation energy loss channel from the heating power gives the graph in Figure VI.47. The intercept at zero fluctuation level is about 35% of the 11 MW of heating power that goes into a non-perturbed discharge at this plasma current level. The power balance that these two experiments suggest is that 35% of the input power is lost via particles and radiation, 30% lost via fluctuation induced thermal transport, and 35% lost via other processes. It is interesting to note that if the particle/radiation and fluctuation loss channels could be shut off completely, the input power needed by the plasma would be within a factor of two of Spitzer resistance heating. (See Figure VI.48 for results of a calculation of Spitzer heating power using $Z_{eff} = 2$, the lowest possible $Z_{eff}$ for a helium plasma.)

While it is obvious that the magnetic fluctuation level rises linearly with paddle insertion, it is not clear why paddle insertion so effectively modulates fluctuation level. The interaction of the paddle and the plasma column is no



doubt a complex one, (witness the different responses of central $T_e$ and soft x-ray signal to paddle insertion), but there are a few simple observations that are relevant. First, insertion of the paddle did not give rise to a global edge vacuum region (the operations edge ion saturation current probe showed little variation and surely did not decrease as the paddle was inserted; see Figure VI.49). This lack of a substantial vacuum complicates simple comparison with the theory of Ho, et al.[8] The second observation is strictly phenomenological. Suppose the paddle is simply an obstruction that intercepts field lines, helicity, fast electrons, or some other parameter. Further suppose that the amount of obstruction is, by some unknown mechanism, directly proportional to the magnetic fluctuation level. Refer to Figure VI.50. If the paddle was removed to a hypothetical insertion of -8 cm, that is, alternatively, an obstruction of area 20 $cm^2$ was removed, then the fluctuation level would go to zero. This is, of course, unlikely, but may have implications for the possible effects of field error reduction.

E) Argon doping experiment

On 08 April 1989, immediately following the completion of the paddle insertion experiment, standard F ≈ -0.1 and $I_p$ = 370 kA RFP discharges were doped with varying amounts of argon. The primary effect of the introduction of a small amount of argon into a helium plasma of $T_e$ = 275 eV is to greatly increase radiative energy loss from the plasma. Manipulation of this energy loss channel has provided insights into the energy confinement behavior of other RFP devices such as ZT-40.[9] The results presented below are similarly suggestive.

In order to lay down a foundation upon which to build a quantitative description of this experiment, it is necessary to first describe how argon was introduced into the plasma in a controlled fashion and then how the resulting $Z_{eff}$ of the plasma was estimated. The argon dopant did not flow directly into the main chamber of the MST vacuum vessel; it was introduced into the pumping duct through a separate puff valve. This puff valve was controlled by the same circuitry that operated the puff valves through which the helium gas fill flowed into the vacuum vessel. It was necessary to pulse the fueling system 400 milliseconds before the discharge in order to allow the argon to fully diffuse up through the pumping duct holes and reach an equilibrium pressure in the vacuum vessel.



The amount of argon puffed into the vacuum vessel was controlled with the circuit shown in Figure VI.51. The resistance of the decade resistance box was proportional to the amount of argon allowed to pass through the puff valve.

Since argon and helium are both monatomic gases, the argon fraction of the fill gas is simply the argon partial pressure fraction. The fast ion gauge was calibrated for argon and helium by comparing the relative sensitivity of the fast ion gauge to these two gases and to hydrogen. (See page 3-47 of the "Granville-Phillips Series 303 Vacuum Process Control Manual.") The results of the calibration are shown in Figure VI.52.

The work described above made possible estimates of the ion density $n_i$ and $Z_{eff}$ at all levels of argon dopant. (The ion density was needed for the calculation of $\tau_E$ and $\beta_\theta$.) The most important assumption made was that most of the argon dopant was Ar IX (neon-like) during the plasma current peak. This assumption is reasonable, at least near the center of the discharge, given that the plasma may be close to coronal equilibrium and the particle confinement time is long enough to allow the argon ions to reach this state. Ion density was calculated assuming quasi-neutrality. The factor $Z_\sigma$ necessary for the calculation of Spitzer resistivity (see Chapter V) is directly related to $Z_{eff}$ via the Spitzer

transport factor $\gamma_E$.[10] Hutchinson[11] made the implicit definition:

$$Z_\sigma = \frac{\gamma_E(Z_{eff} = 1) \cdot Z_{eff}}{\gamma_E(Z_{eff})} \qquad \text{(VI.13)}$$

where $\gamma_E(Z_{eff})$ is the particular $\gamma_E$ for such a $Z_{eff}$. This relationship can be approximated by[11]

$$Z_\sigma = 0.40 + 0.62\ Z_{eff} \qquad \text{(VI.14)}$$

for $Z_{eff}$ less than 20.

The argon doping experiment varied $Z_{eff}$ from 2 (helium plasma) to 4.3, a $\Delta Z_{eff} = 2.3$ (Figure VI.53). Even though the initial $Z_{eff}$ was actually larger than 2 due to impurity contamination of the plasma (see below for an estimate of the initial $Z_{eff}$), a $\Delta Z_{eff}$ of this magnitude produced measurable effects. The measured parallel resistivity $\eta_\parallel^*$ (Eq. (V.20)) and the Spitzer resistivity $\eta_{sp}$ (Eq. (V.17)) are graphed in Figure VI.54. Both $\eta_\parallel^*$ (squares) and $\eta_{sp}$ (triangles) increased as the argon fraction was increased. In fact, both resistivities increased by about the same amount. This is illustrated in Figure VI.55 where the quantity $\eta_\parallel^*$ minus $\eta_{sp}$ is plotted. This quantity is the anomalous resistivity of the RFP. For this experiment the anomalous resistivity was



about 85% of the measured parallel resistivity. This experiment illustrates the truly anomalous nature of the resistivity of the RFP; if the anomalous resistivity resulted from edge-peaked $Z_{eff}$ profiles that enhance power and/or helicity dissipation, then we should have observed dissimilar changes in $\eta_\parallel^*$ and $\eta_{sp}$ when $Z_{eff}$ was varied. This result reinforces the presumption that the Spitzer resistivity profile is flat, otherwise the changes in $\eta_{sp}$ and $\eta_\parallel^*$ would not have matched (the calculation of $\eta_\parallel^*$ assumes a spatially uniform resistivity). These results, however, force no claims about the shape of a non-Spitzer anomalous resistivity profile.

The results from this argon doping experiment contained a number of other noteworthy results. Poloidal beta remained nearly constant as the plasma was doped (see Figure VI.56), as expected from the results of the ZT-40 krypton doping experiment (see Chapter V). However, not only was $\beta_\theta$ constant, nearly every other parameter was also. Central electron temperature, density, and energy density remained constant as the argon fraction increased (Figures VI.57, VI.58, and VI.59). However, here as in the paddle insertion experiment, the time integrated soft x-ray signal dropped as the plasma was doped (Figure VI.60). This suggests that these two perturbations affect the suprathermal tail electrons much more than they affect the bulk electrons.

Plasma current dropped slightly (which explains the slight rise in $\beta_\theta$), loop voltage rose slightly, and heating power remained nearly constant (Figures VI.61 and VI.62).

The above results translated into an energy confinement time that was constant as the plasma was doped with 0 to 14% argon (Figure VI.63). This is a remarkable result in light of the fact that impurity radiation rose four-fold as the plasma was doped (Figure VI.64). Two explanations of this result immediately come to mind. The first, drastic profile changes, is a possibility that cannot be ruled out with the present set of diagnostics. The second explanation, which has some support, is that certain non-radiative energy loss channels dropped as the plasma was doped.

An examination of the results from the diagnostics which monitor the non-radiative energy loss channels reveals the following observations. First, neither the magnetic nor the floating potential fluctuation levels changed as the plasma was doped (Figures VI.65 and VI.66). It is likely that neither of these loss channels changed. The second, and most important, observation is that the bolometer and VUV impurity signals exhibited a remarkably linear relationship. This, of course, would be expected if the bolometer was only sensitive to radiation; in such a situation the line fit to the data would extrapolate to the origin. This is clearly not the case, as can be seen in Figure VI.67. As the argon fraction



was increased, the VUV impurity signal rose 400%, while the bolometer signal rose only 50%. Extrapolation of the VUV impurity signal to zero leaves a substantial bolometer signal; this is a definitive indication that a sizable portion of the energy reaching the bolometer is non-radiative. Of course, this may not be the case if the spectral distribution of the radiation varies greatly during the doping experiment, but this does not seem likely.

The lack of independent information about the non-radiative component of the bolometer signal limits conclusions that can be made. There are, however, a number of interesting scenarios that can be explored. Suppose, for instance, that the non-radiative (presumably particle) energy loss channel dropped linearly as the plasma was doped, reaching zero at maximum dopant fraction. This would mean that about 65% of the energy reaching the bolometer during a non-doped discharge (VUV impurity signal of 100, bolometer signal of 1) was non-radiative. If this is the case, then, in a standard discharge, about 12% of the energy flowing out of the plasma is lost via radiation. (Assuming, as established by previously discussed experiments, that the bolometer is proportional to a 35% fraction of the energy leaving the plasma.)

As mentioned earlier, it is not too difficult to estimate the initial $Z_{eff}$ at the start of the argon doping series. Refer again to Figure VI.64. Extrapolate the approximately linear relationship between argon fraction and VUV signal back to a zero VUV signal. This zero intercept of -0.06 means that the normal impurity radiation level is equivalent to a 0.06 argon fraction. Take oxygen as an impurity and guess a final charge state of Oxygen VII (helium-like). This implies

$$Z_{eff} = \frac{0.94(2)^2 + 0.06(6)^2}{0.94(2) + 0.06(6)} = 2.6 \quad . \qquad \text{(VI.15)}$$

This $Z_{eff}$ is only slightly larger than $Z_{eff}$ of 2 for a pure helium discharge. The fact that this estimate of $Z_{eff}$ is slightly larger than that assumed in the earlier discussion does not change any of the stated results, but it does imply that the plasma was quite free of impurities at the start of the doping series.

There is one final apparent inconsistency in the doping experiment data that needs to be discussed. In this experiment, unlike previously discussed experiments, the heating power ($V_\ell I_p$) was not roughly proportional to the heating energy ($V_\ell I_p$ integrated over the first 20 milliseconds of the discharge). This situation occurred



because, as the argon fraction was increased, the loop voltage necessary to start up and maintain the discharge during the first 10 milliseconds increased also. (Calculations indicate that only a small fraction of the heating energy is used to ionize the helium and argon.) But, by the time the plasma current peak was reached, the loop voltage had settled down to about 30 volts, no matter what the argon fraction. This situation forces scaling of the bolometer signal against heating energy instead of heating power, as was previously done. Such a graph is shown in Figure VI.68. The assumption that other energy loss channels remained constant as the plasma was doped leads to the conclusion that the bolometer sees about 1/3 of the energy lost from a non-doped discharge. This is, of course, in line with the results from previously discussed experiments.

The results of an 01 April 1989 plasma current scan of helium discharges further illustrate the points discussed above. The plasma current was scanned from 150 kA to 450 kA in four steps. At each step the fill gas density was varied. Enough shots were taken at each step to allow the discharges to stabilize (presumably by stripping the walls of impurities). The VUV impurity signal is shown versus heating energy in Figure VI.69. It appears that the amount of energy lost via radiation stabilizes at a constant level, no matter what the current level. The bolometer signal, however, does

not stabilize at such a constant limit (see Figure VI.70). It appears to reach a linearly rising limit that extrapolates to the origin. This means that the non-radiative loss channel grows as the plasma current increases. This is an intriguing observation that needs further investigation to determine the nature and composition of the non-radiative loss channel.

The data on Figure VI.69 can also be used to estimate the fraction of the input heating energy lost via radiation. Assume that the discharge at 0.1 MJ and VUV impurity signal of 280 was so radiation dominated that all energy was lost via radiation. This gives a conversion factor of 0.1/280 MJ/arb. Applying this factor to the highest current discharges (at 0.25 MJ) gives a radiative energy loss for these discharges of about 10% of the input energy, similar to the previous estimate.

F) MST scaling of confinement parameters

Two significant plasma current scaling experiments were performed on MST, one in hydrogen discharges, the other in helium. Scaling experiments such as these are almost always done in order to gain empirical knowledge of the variation of various confinement parameters with an easily controlled parameter, usually plasma current. In addition, there are insights that can be drawn from the data below that may



further an understanding of the mechanisms that govern the confinement characteristics of an RFP.

The initial scaling study in hydrogen was done 11 February 1989. There were a number of difficulties with this experiment that limit its usefulness. The plasmas were of very low density and, as such, 15 shot averages were calculated at each current step. The Thomson scattering diagnostic was not independently calibrated for absolute electron density; an estimate of the calibration factor was made by comparison to the line-averaged density measured by the sometimes functional microwave interferometer. The results for $T_e$, $\tau_E$, and $\beta_\theta$ versus $I_p$ are presented in Figures VI.71, VI.72, and VI.73. The only obvious trend appears to be a possible linear scaling of $T_e$ with $I_p$, at approximately 2/3 eV/kA. This scaling is similar to that seen on the Poloidal Divertor RFP[12] and elsewhere.[13]

The other current scaling experiment, done on 01 April 1989, has already been mentioned. The purpose of this experiment was to step plasma current upward, and, at each step, to vary the electron density as much as possible. This was done by varying initial gas fill density from the minimum density necessary to insure initiation of the discharge to the ceiling set by the flow rate of the puff valves. As can be seen from Figure VI.74, this varied the filling pressure by only a factor of three; more flow from the puff valves or

another fueling mechanism would be necessary to further extend the range.

The results of these attempts at density manipulation are shown in Figure VI.75. Two points are evident. First, the central electron density hardly varied by more than a factor of two at each current setting. Second, density increase with current appears to be almost linear. This is a manifestation of the apparent tendency of MST to operate at constant $I_p/N$ ratio (N is the line density). See Figure VI.76 for evidence of this. Note that only at the lowest currents is $I_p/N$ close to the density limit of $1.0 \times 10^{-14}$ amp-meter. Recall from Chapter V that this limit may be where the best energy confinement times are achieved; it may be worth some effort to approach it more closely.

It is worth noting that there may also be a low density limit for RFP's. Ortolani and Rostagni suggest that the streaming parameter $\xi$ must be below a critical value; this sets an upper limit on $I_p/N$.[16] The data from this scaling experiment suggest a connection between $I_p/N$ and the time integrated soft x-ray signal. Figure VI.77 is a plot of these two quantities; the square symbols represent the group of shots near 400 kA and the triangle symbols the group near 300 kA. There is no apparent correlation of $\tau_E$ with $I_p/N$ for these two groups (Figure VI.78), although the uncertainties in both quantities make a definitive statement impossible.



The scaling of $T_e$, $\tau_E$, and $\beta_\theta$ with plasma current is shown in Figures VI.79, VI.80, and VI.81. Note that $T_e$ appears to scale linearly with $I_p$ only at the lowest values of $I_p$; it almost appears to saturate at a limit of 300 eV at higher currents. This behavior is not totally unlike that seen in other current scaling experiments;[14] the canonical linear scaling of $T_e$ with $I_p$ may not be applicable at higher currents.

The best values of $\tau_E$ and $\beta_\theta$ were achieved at the lowest current settings. This is, of course, where $I_p/N$ was smallest, so the result is not entirely unexpected. Of this group of shots with $I_p \lesssim 200$ kA, the highest values of $\tau_E$ are correlated with the lowest values of VUV impurity signal and bolometer signal. These values occurred at $I_p \approx 200$ kA (see Figures VI.82 and VI.83); these were the discharges at the end of a "clean-up" series. $\tau_E$ appears to remain at about 1.0 millisecond at the higher currents, but $\beta_\theta$ appears to continue to drop, a consequence of the fact that only $n_e$ scaled with $I_p$. The energy density (Figure VI.84) did show a monotonic and possibly linear increase with $I_p$, but this increase was offset in the calculation of $\tau_E$ by concomitant increases in the heating power as plasma current was increased.

There is one possibly encouraging result from this confinement scaling experiment. A look at the plot of loop voltage versus plasma current in Figure VI.85 reveals two observations. First, the largest values of $\tau_E$ occurred around 200 kA because $V_\ell$ reached its lowest values there. Second, although $V_\ell$ increased during the step from 200 kA to 300 kA, it did not continue to increase at the higher current steps. The resistivity reflects this behavior; see Figure VI.86 where measured resistivity $\eta_\parallel^*$ and Spitzer resistivity are plotted versus $I_p$. There was an initial decrease in both resistivities at low current while MST cleaned up, but at higher currents only $\eta_\parallel^*$ continued to decrease. The significance of this trend is unclear.

Finally, the scaling of $\tau_E$ with $I_p$ does not appear to be encouraging. In fact, it seems that over the somewhat narrow range of high currents covered by this scaling experiment that a constant $\tau_E$ is maintained because energy density and input power increase proportionally. The combination of factors behind this observation is

1) $n_e$ rises with $I_p$ to keep $I_p/N$ roughly constant
2) $T_e$ and $V_\ell$ remain roughly constant.

In short, any increase in energy density seems to require an increase in input power. This is not an encouraging trend,



but perhaps the results with the new MST poloidal field windings will be more positive.

C) Summary of energy confinement observations

The observations noted below apply specifically to high current ($\geq$300 kA), $F \approx -0.1$, $\theta \approx 1.6$ RFP discharges in MST. The results may not be relevant in other operational regimes.

Statistical analysis of the fluctuations in electron temperature and density in a series of reproducible discharges revealed that all but a few percent of the scatter of the $T_e$ and $n_e$ data points is due to the inherent statistical uncertainty of the measurement technique. Plasma induced fluctuations in central $T_e$ and $n_e$ are no larger than a few percent and do not appear to be correlated with each other or with sawtooth oscillation in other parameters.

Investigation of the mechanisms and the routes by which energy flows out of the plasma suggests that, for a standard RFP discharge,

a) 1/3 of the energy is lost by thermal conduction due to stochastic magnetic field fluctuations.
b) 1/4 of the energy is lost by particles leaving the plasma.
c) 1/10 of the energy is lost via radiation
d) the balance of the energy is lost through an unknown channel.

These observations were gathered from a series of perturbation experiments under the assumption that the perturbations to the plasma were small and the effects caused were separable. Other specific assumptions are that

a) the magnetic field fluctuations were stochastic and due to reconnection, not plasma motion
b) the bolometer and VUV impurity signals (which are integrated over the entire discharge) can be used, with care, to illuminate the energy loss processes occurring during the "equilibrium" (current peak) portion of the discharge
c) and that the non-radiative part of the bolometer signal is representative of a particle energy loss channel.

The existence of such a large particle energy loss channel raises questions that need to be answered. Calculations done by Hokin[15] indicate that the neutral particle energy loss channel may be substantial. Specific measurements of this loss channel should be carried out.

The modulation of the soft x-ray signal during the two perturbation experiments may be providing additional information about RFP energy confinement. Suppose that the SXR signal is indicative of the energy of the suprathermal electrons. If this is so, then the results of the paddle limiter or argon doping experiments suggest that increases in



such perturbations are correlated with a decrease in the energy of the suprathermal electrons. If the suprathermal electrons are part of a significant energy loss channel, then such a decrease may balance radiation, fluctuation, particle, or other energy loss channels (and thereby cause the quantitative energy loss results quoted above to be incorrect). The suprathermal electrons may be energetic particles leaving the plasma (and observed on the bolometer) or they may be the "unknown energy loss channel" referred to above. Since they may carry a substantial portion of the plasma current (at least in some situations such as large $I_p/N$), they may be involved in the generation of magnetic fluctuations. In any case, these perturbation experiments should be repeated while the suprathermal electrons are being monitored with a diagnostic such as an electrostatic energy analyzer (see Chapter V for references). The results might help to fill out or correct the energy confinement picture presented in this thesis.

As a final note recall the observation that, during the perturbation experiments, the global quantity that showed strong variation was the loop voltage. Electron temperature and density and plasma current were approximately constant, meaning that poloidal beta was constant even as the amount of power flowing in and out of the plasma varied. If these observations are of global significance and not simple

artifacts of hidden profile or other changes, then these experiments lend support to the contention that the RFP is a constant beta device (or, perhaps, beta limited device, since $\beta_\theta$ did vary during the current scan). These experiments also seem to indicate that understanding the behavior and cause of the anomalous loop voltage is a key to understanding the energy confinement of the RFP.



References


[1] R.G. Watt and E.M. Little, Phys. Fluids 27 (4), 784 (1984).

[2] W.H. Press et al., Numerical Recipes, (Cambridge University Press, Cambridge, 1986), p. 539.

[3] M. Bassan, F. Flora, and L. Giudicotti, in "Proceedings of the International School of Plasma Physics," Varenna, 1987 (Società Italiana di Fisica, Bologna, 1988), Vol. III, p. 1035.

[4] P.R. Bevington, Data Reduction and Error Analysis for the Physical Sciences, (McGraw-Hill, New York, 1969), p. 72.

[5] H.A.B. Bodin, in "Proceedings of the International School of Plasma Physics," Varenna, 1987 (Società Italiana di Fisica, Bologna, 1988), Vol. I, p. 3.

[6] A.B. Rechester and M.N. Rosenbluth, Phys. Rev. Lett. 40, 38 (1978).

[7] I.H. Hutchinson, M. Malacarne, P. Noonan, and D. Brotherton-Ratcliffe, Nucl. Fusion 24, 59 (1984).

[8] Y.L. Ho, S.C. Prager, and D.D. Schnack, Phys. Rev. Lett. 62, (13), 1504 (1989).

[9] M.M. Pickrell, et al., Los Alamos National Laboratory report, "Evidence for Poloidal Beta Limited Confinement on the ZT-40M Reversed Field Pinch" (1989).

[10] L. Spitzer and R. Härm, Physical Review 89 (5), 977 (1953).

[11] I.H. Hutchinson, Principles of Plasma Diagnostics, (Cambridge University Press, Cambridge, 1987), p. 18.

[12] D.J. Den Hartog and R.N. Dexter, University of Wisconsin-Madison PLP 1061 (1989).

[13] B. Alper, S. Martini, and S. Ortolani, Nucl. Fusion 26 (9), 1256 (1986).

[14] P. Weber in "Proceedings of the Japan-U.S. Workshop on RFP Data Base Evaluation," Tokyo, 1989 (University of Tokyo, 1989).

[15]S.A. Hokin, R.N. Dexter, and E. Scime, Abstract submitted for the 31st Annual Meeting of the Division of Plasma Physics-American Physical Society (Anaheim, 1989).

[16]S. Ortolani and G. Rostagni, Nucl. Instrum. and Methods 207, 35 (1983).



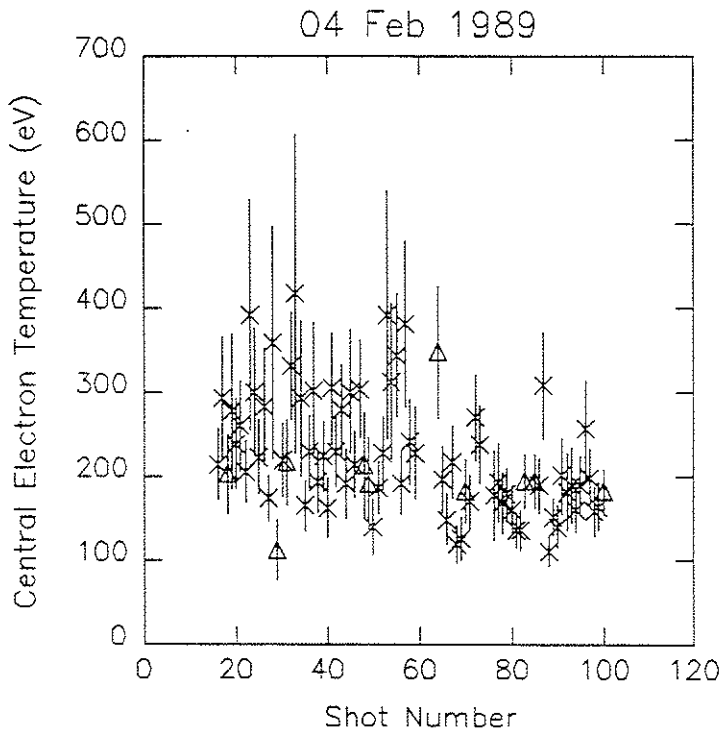


Figure VI.1: Central $T_e$ versus shot number from a series of 440 kA hydrogen discharges.

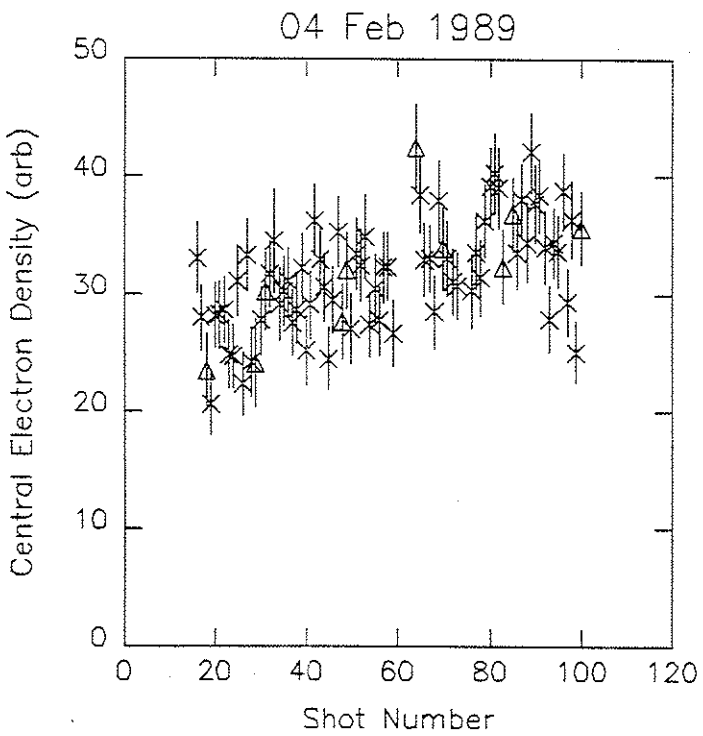


Figure VI.2: Central $n_e$ versus shot number from a series of 440 kA hydrogen discharges.



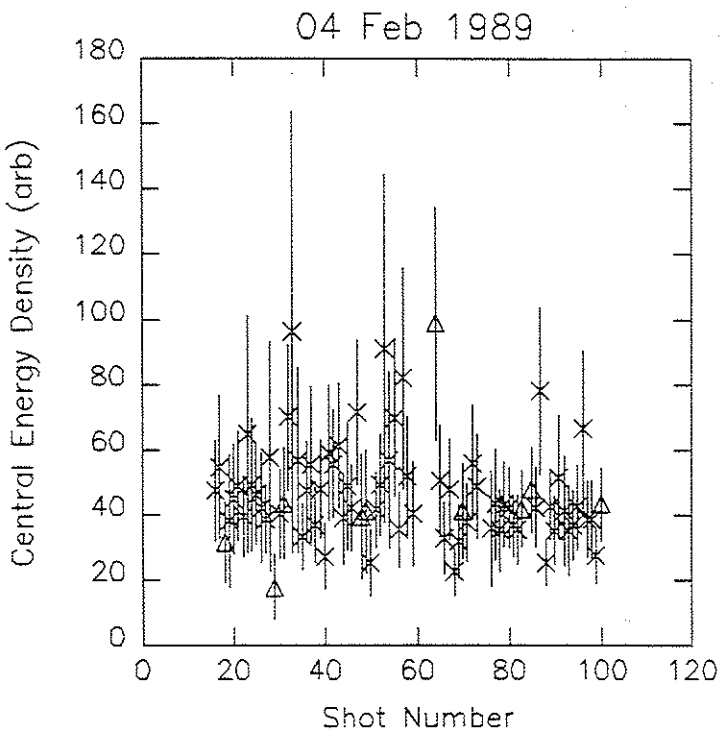


Figure VI.3: Central $n_eT_e$ product versus shot number from a series of 440 kA hydrogen discharges.

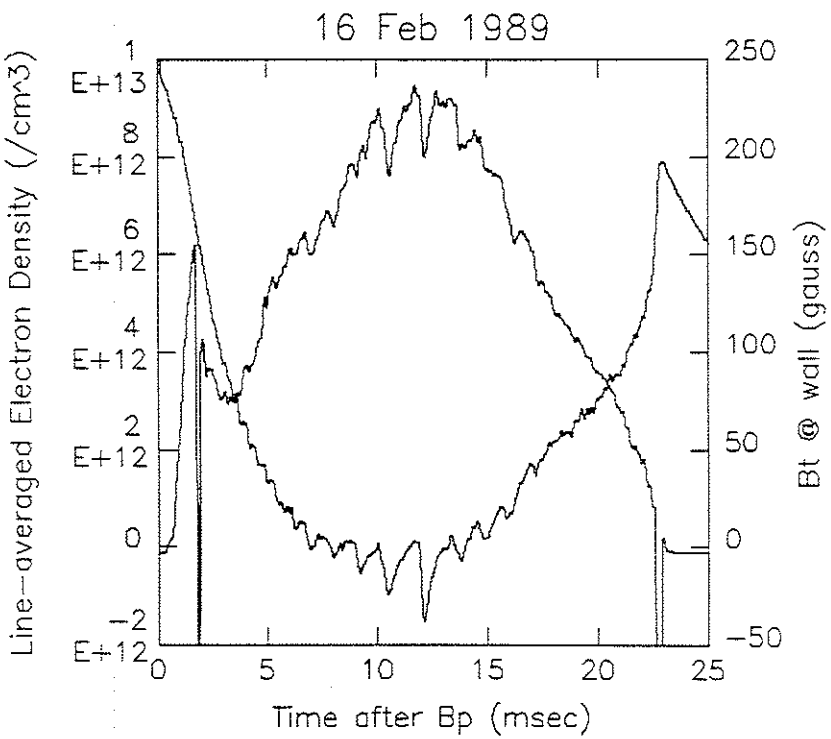


Figure VI.4: $\bar{n}_e$ (upper trace) and $B_T$ @ wall (lower trace) versus time after initiation of discharge (shot #172).



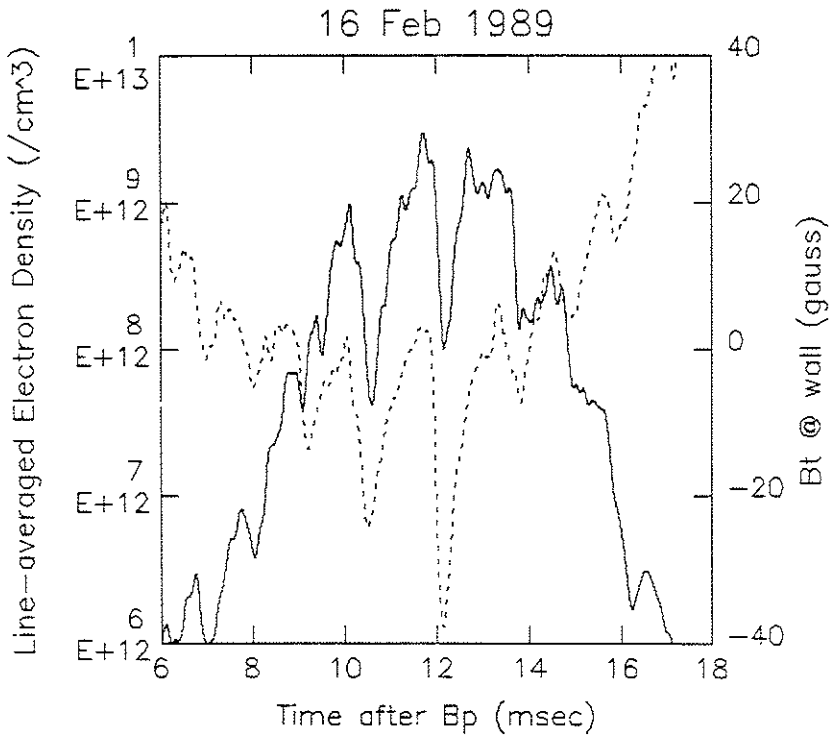


Figure VI.5: $\bar{n}_e$ (solid trace) and $B_T$ @ wall (dashed trace) versus time after initiation of discharge (shot #172).

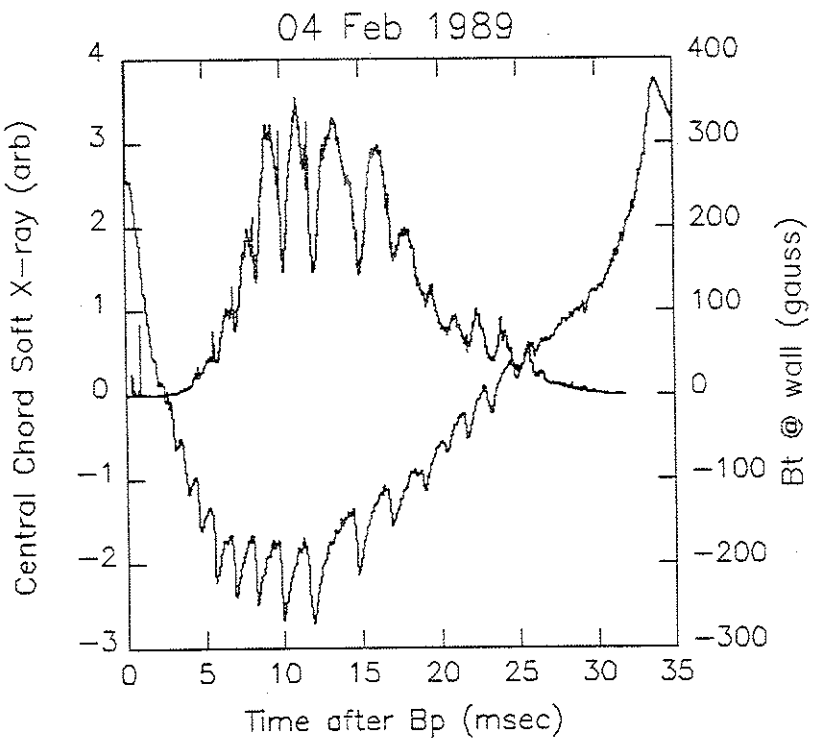


Figure VI.6: Central chord SXR (upper trace) and $B_T$ @ wall (lower trace) versus time after initiation of discharge (shot #23).



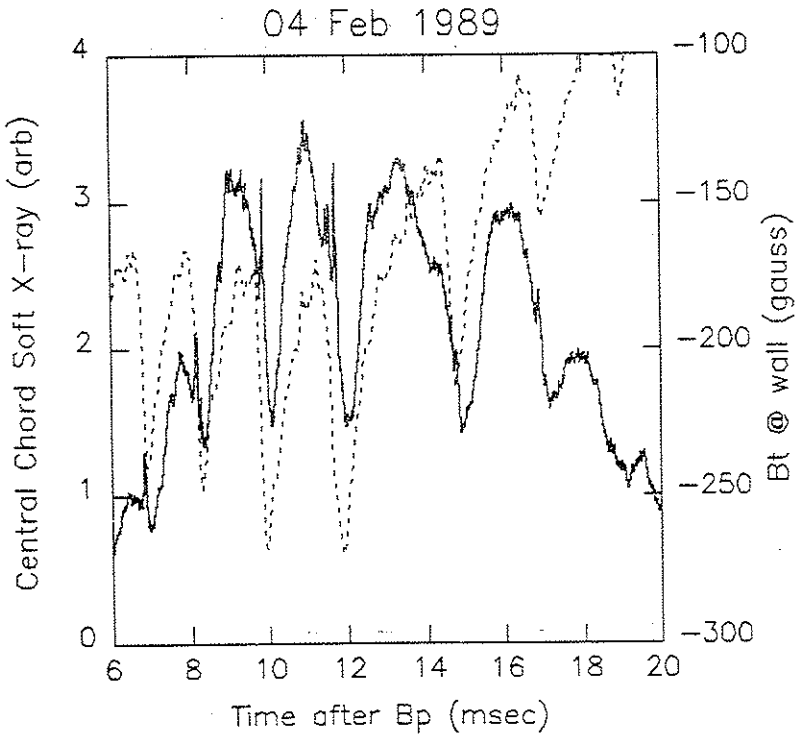


Figure VI.7: Central chord SXR (solid trace) and $B_T$ @ wall (dashed trace) versus time after initiation of discharge (shot #23).

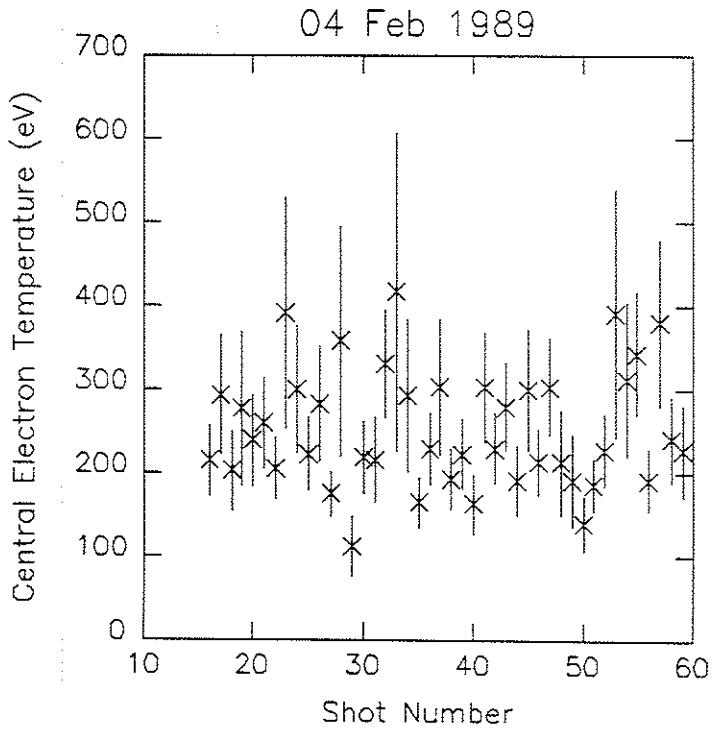


Figure VI.8: Central $T_e$ versus shot number from a subset of a series of 440 kA discharges.



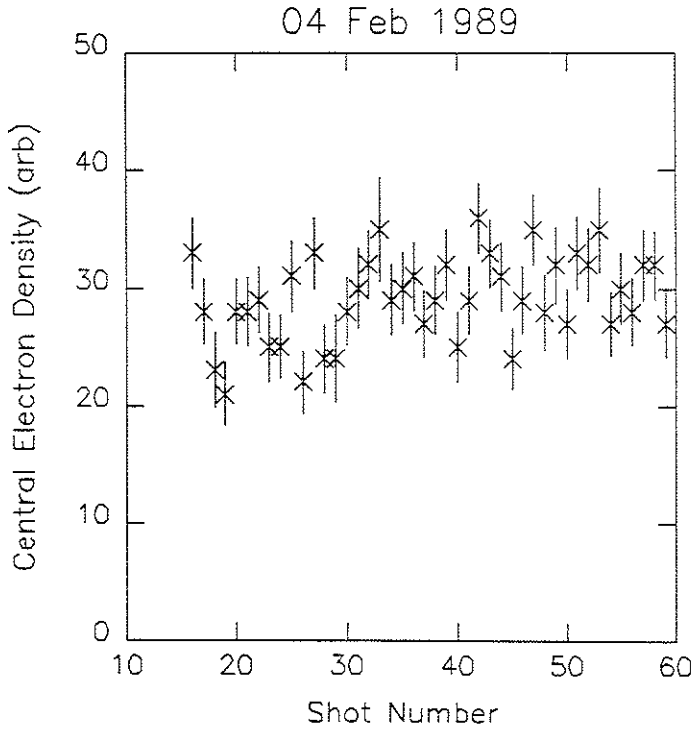


Figure VI.9: Central $n_e$ versus shot number from a subset of a series of 440 kA discharges.

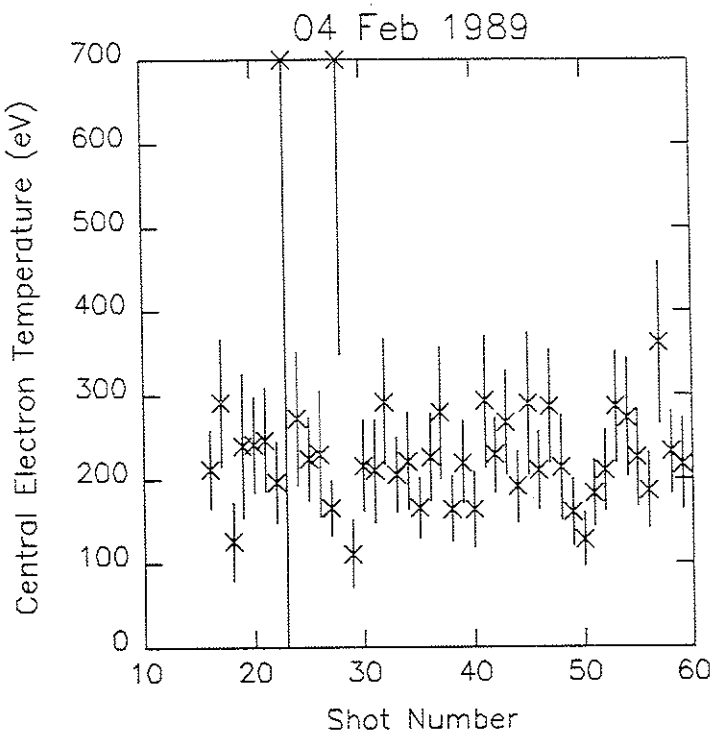


Figure VI.10: Central $T_e$ as estimated by a nonlinear least-square fitting routine. This is the subset of shots shown in Figures VI.8 and VI.9.



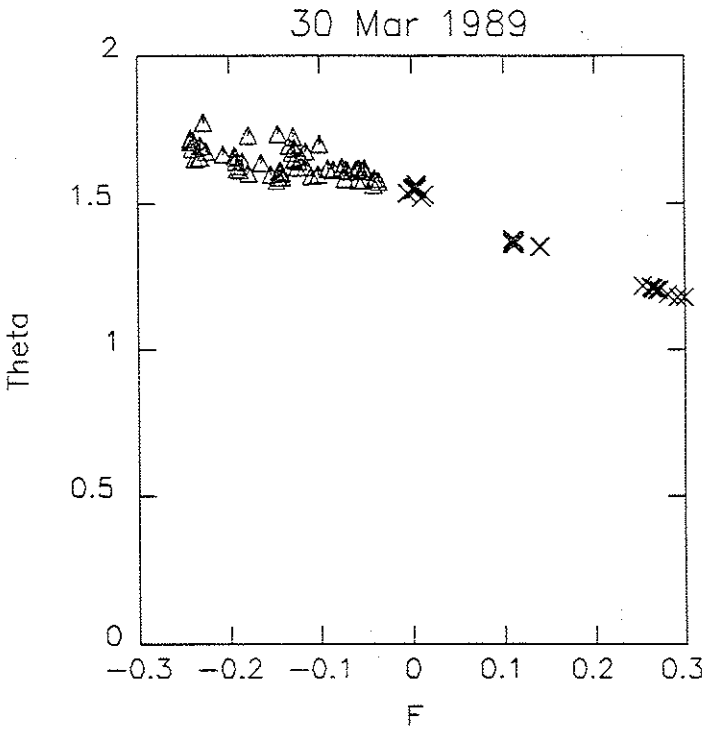


Figure VI.11: The pinch parameter θ versus the reversal parameter F from an F-scan series. The triangle symbols represent discharges where $F < 0$, the cross symbols discharges where $F > 0$.

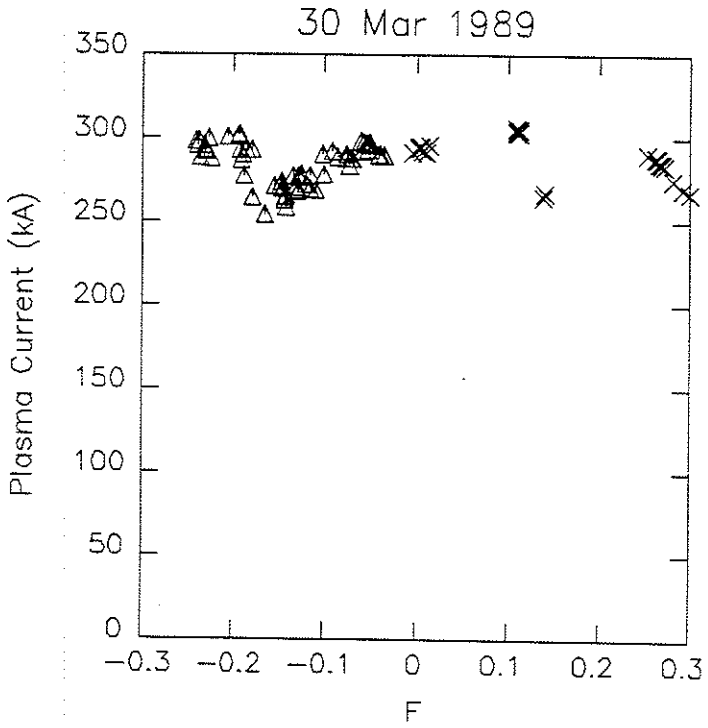


Figure VI.12: $I_p$ versus F from an F-scan series.



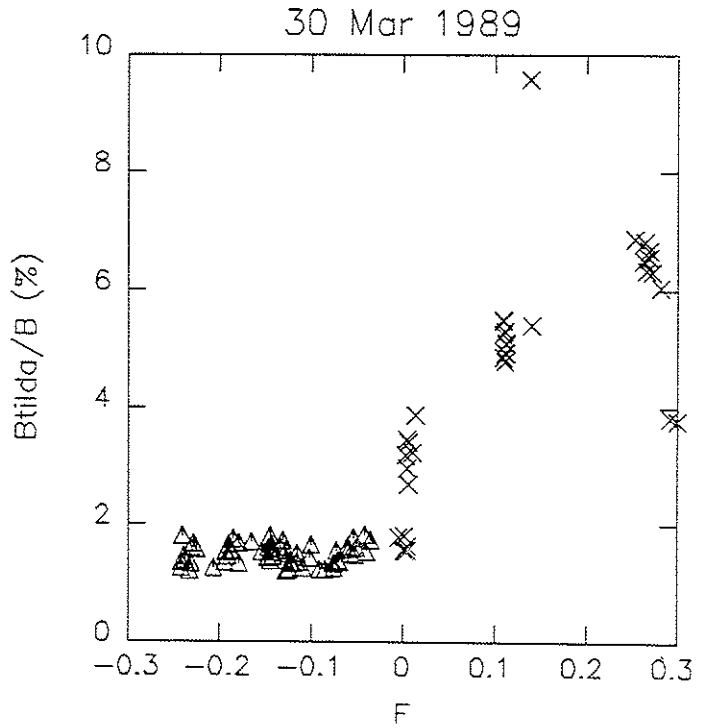


Figure VI.13: $\tilde{B}/B$ versus F from an F-scan series.

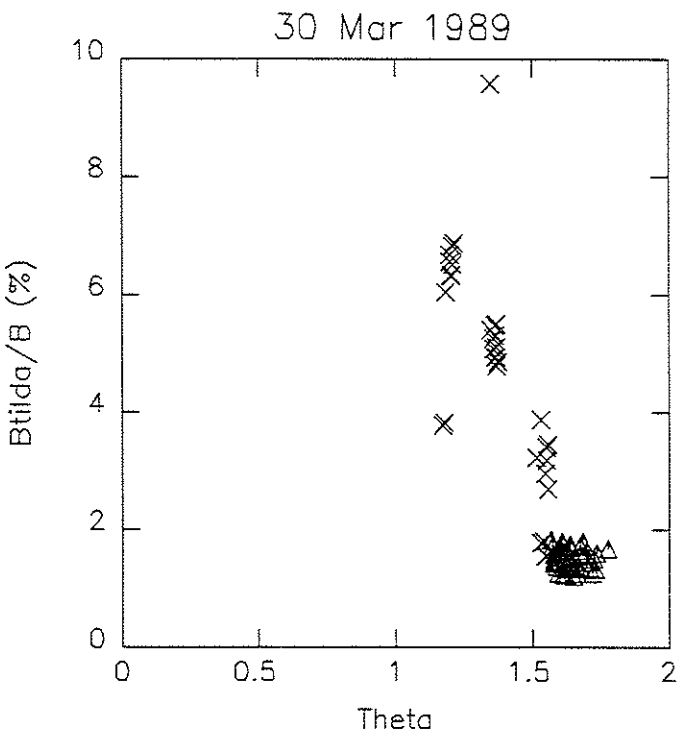


Figure VI.14: $\tilde{B}/B$ versus $\theta$ from an F-scan series.



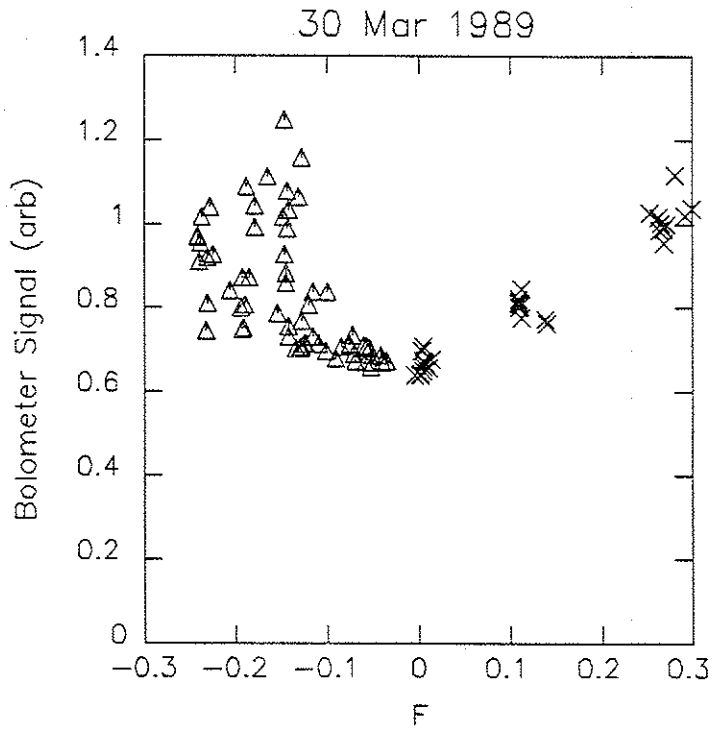


Figure VI.15: Bolometer signal versus F from an F-scan series.

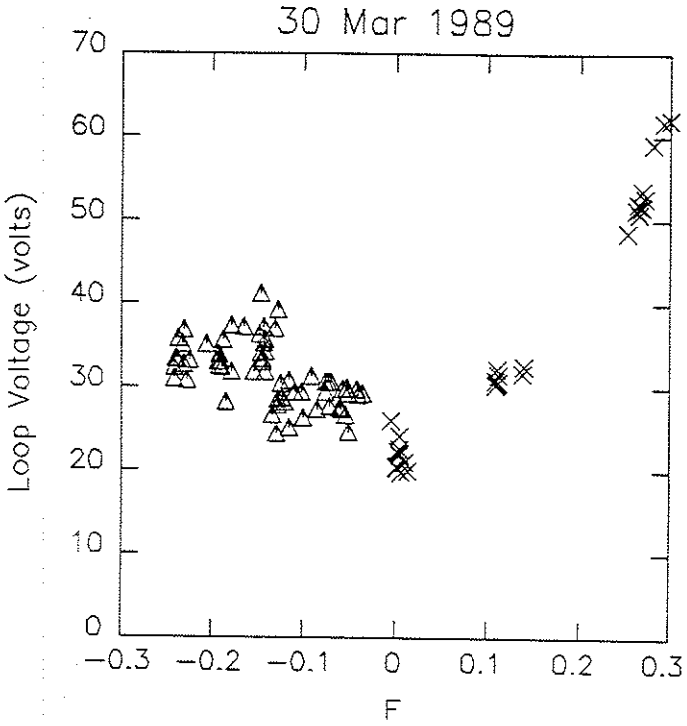


Figure VI.16: $V_l$ versus F from an F-scan series.



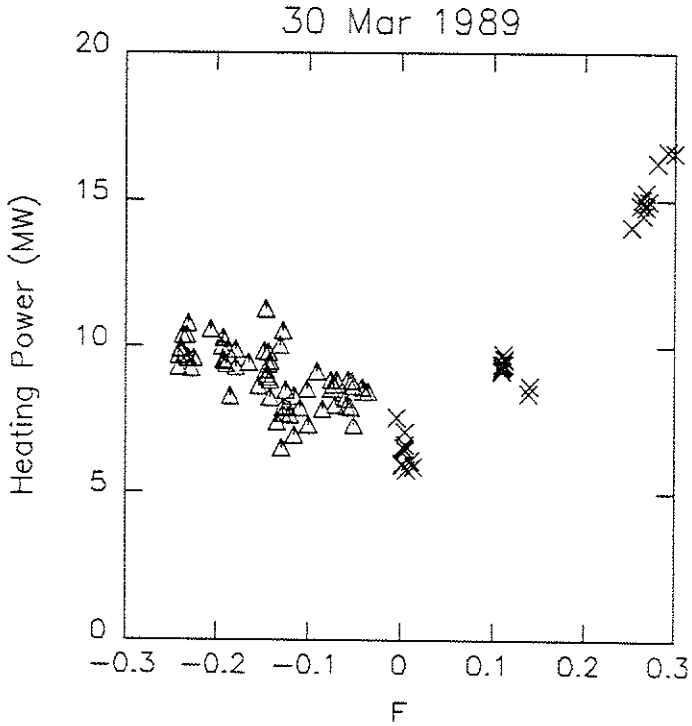


Figure VI.17: Heating power versus F from an F-scan series.

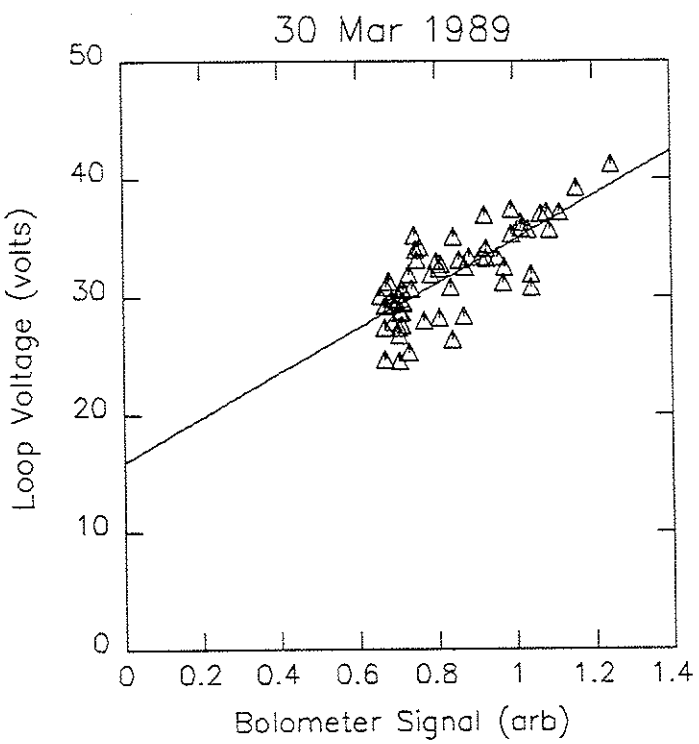


Figure VI.18: $V_\ell$ versus bolometer signal from an F-scan series.



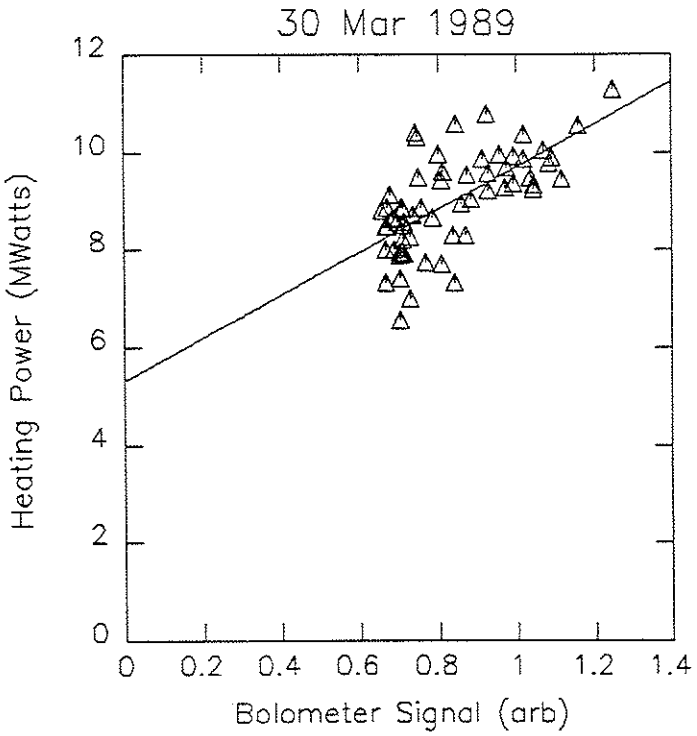


Figure VI.19: Heating power versus bolometer signal from an F-scan series.

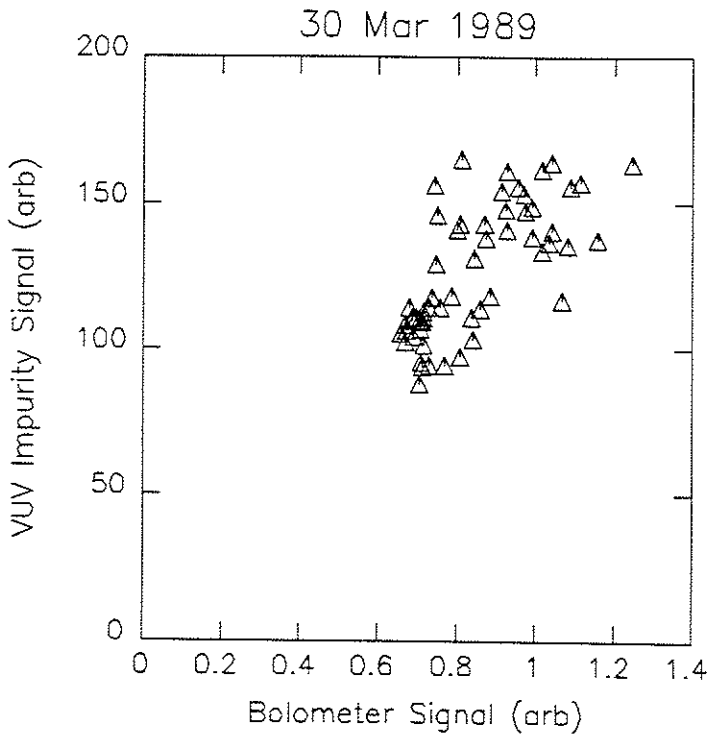


Figure VI.20: VUV impurity signal versus bolometer signal from an F-scan series.



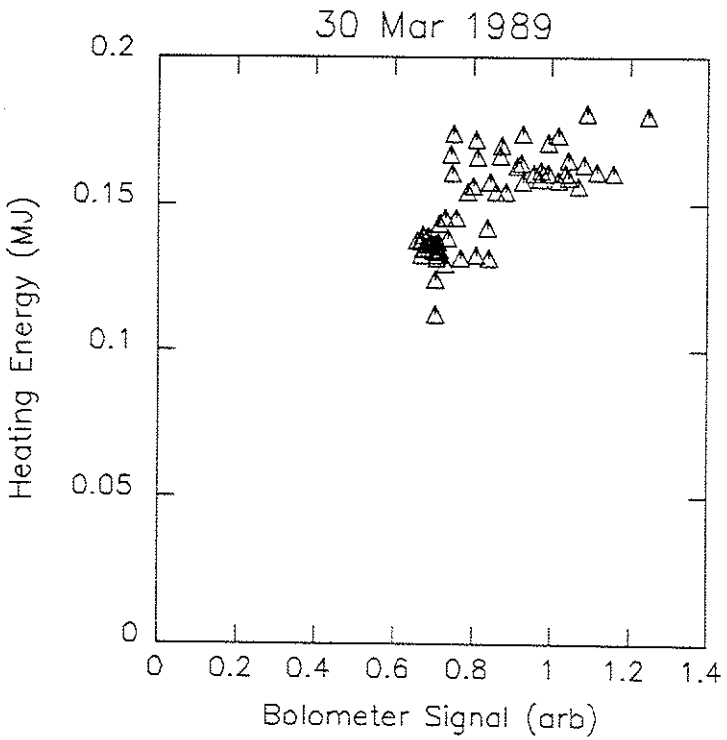


Figure VI.21: Heating energy versus bolometer signal from an F-scan series.

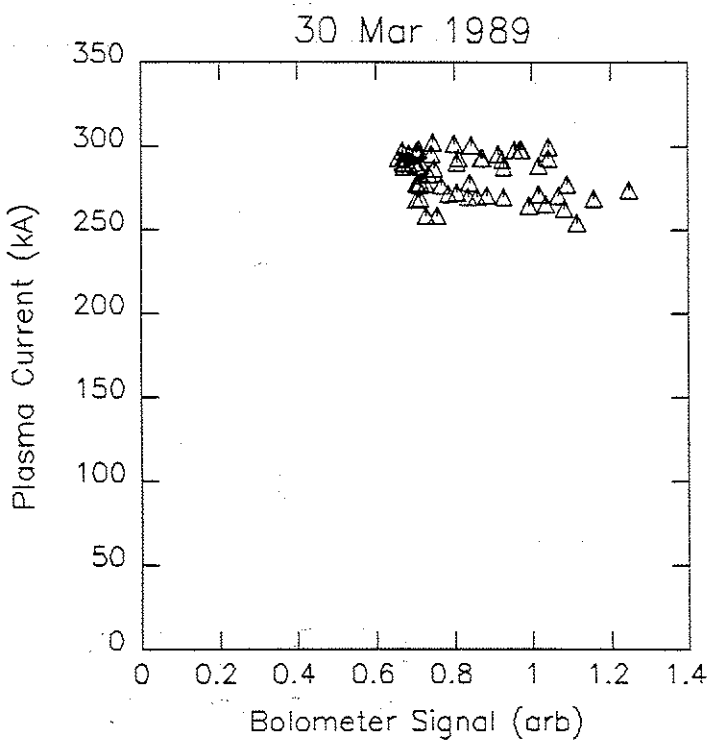


Figure VI.22: $I_p$ versus bolometer signal from an F-scan series.



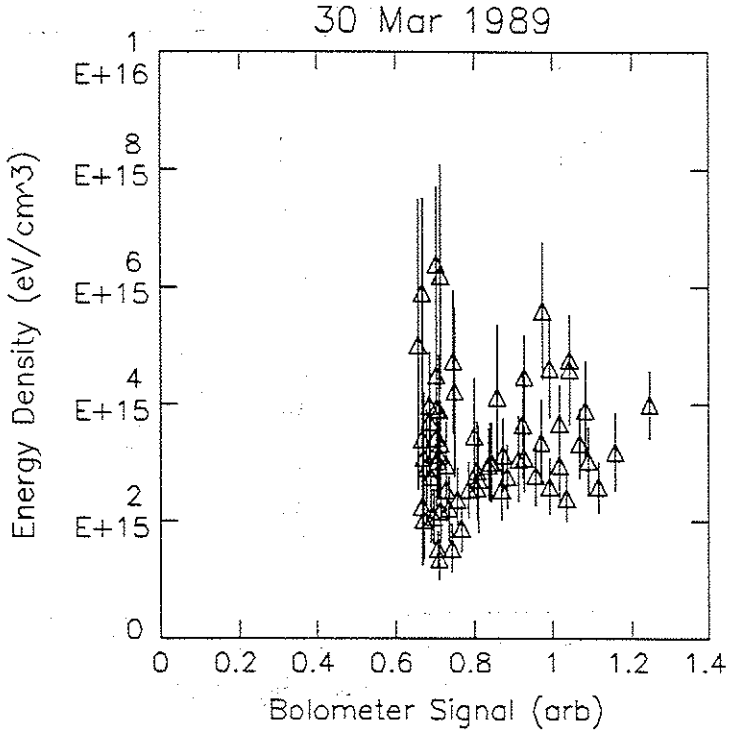


Figure VI.23: Central $n_eT_e$ product versus bolometer signal from an F-scan series.

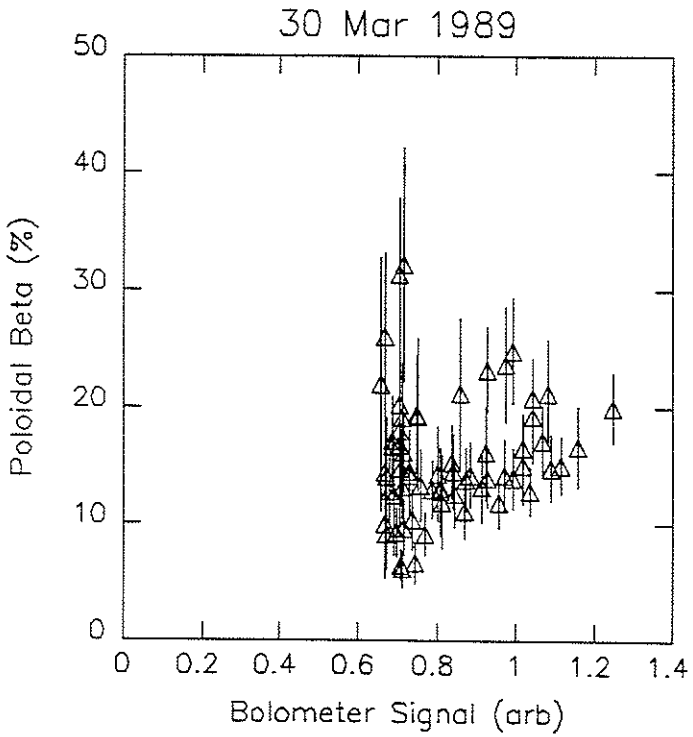


Figure VI.24: $\beta_\theta$ versus bolometer signal from an F-scan series.



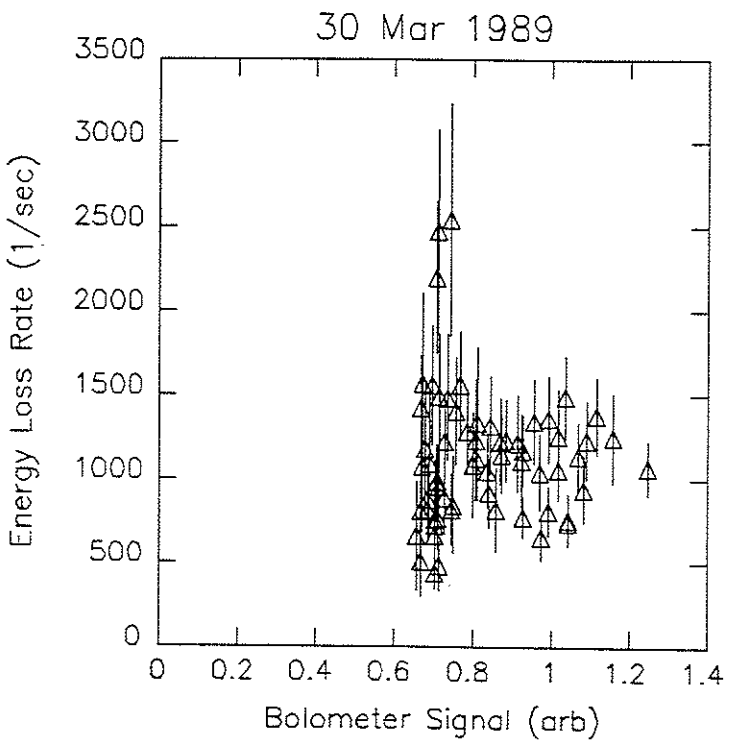


Figure VI.25: $\nu_E$ versus bolometer signal from an F-scan series.

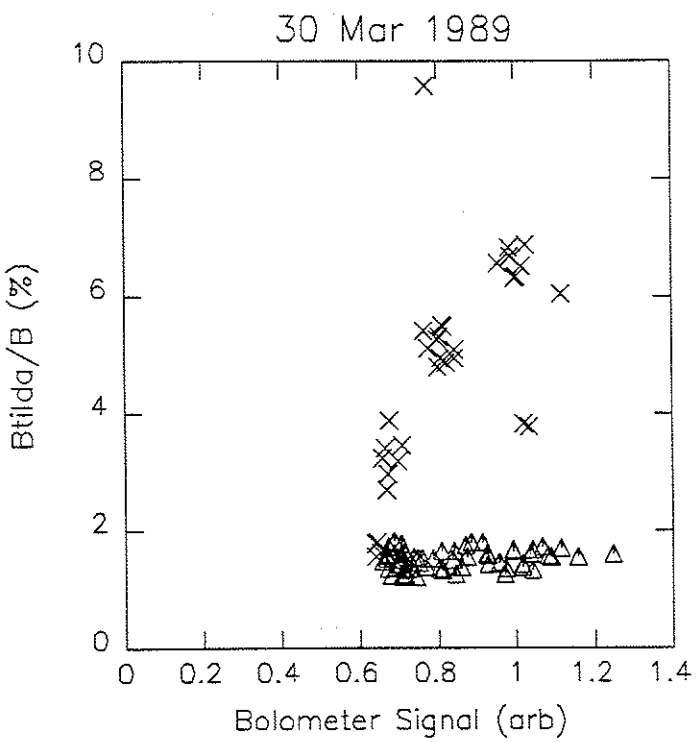


Figure VI.26: $\tilde{B}/B$ versus bolometer signal from an F-scan series.



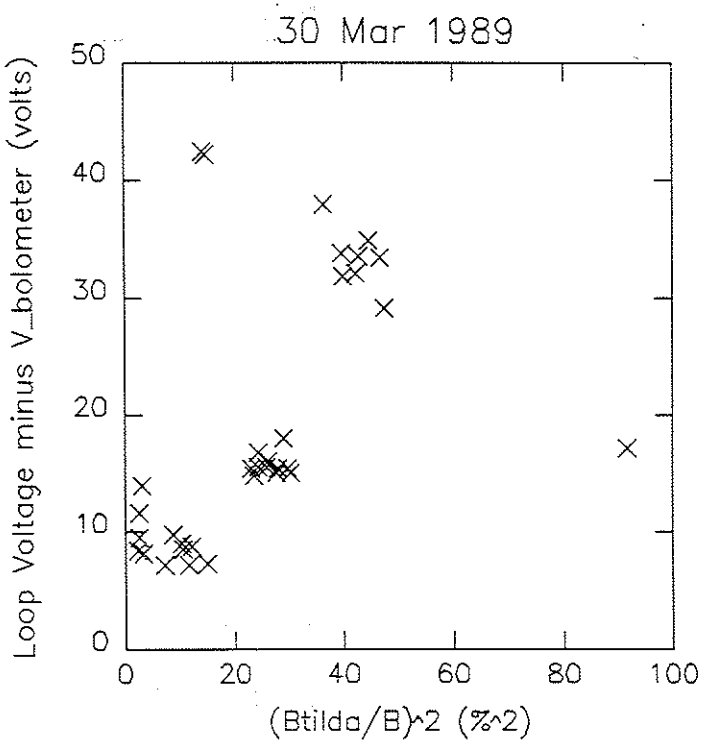


Figure VI.27: $V_\ell$ minus bolometer correlated loop voltage versus $(\tilde{B}/B)^2$ from an F-scan series.

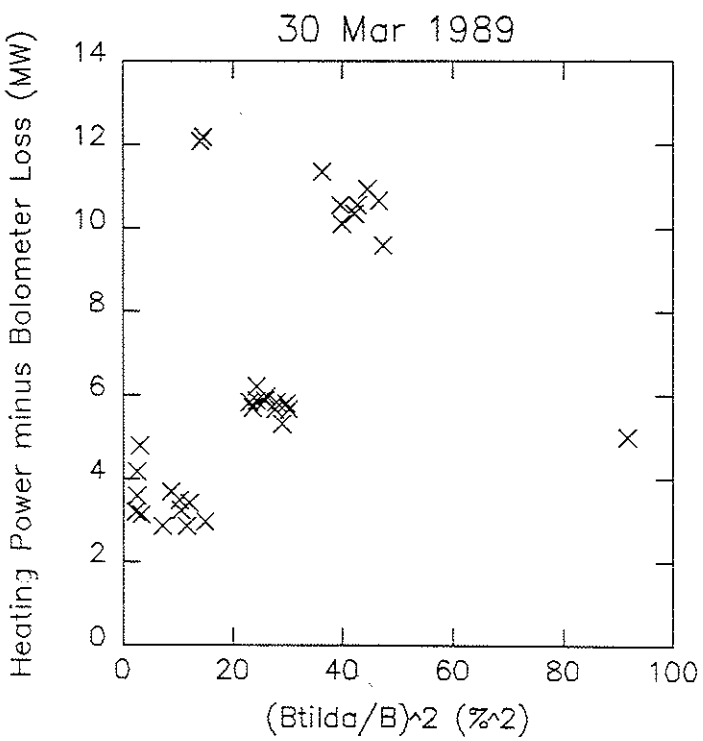


Figure VI.28: Heating power minus bolometer correlated power loss versus $(\tilde{B}/B)^2$ from an F-scan series.



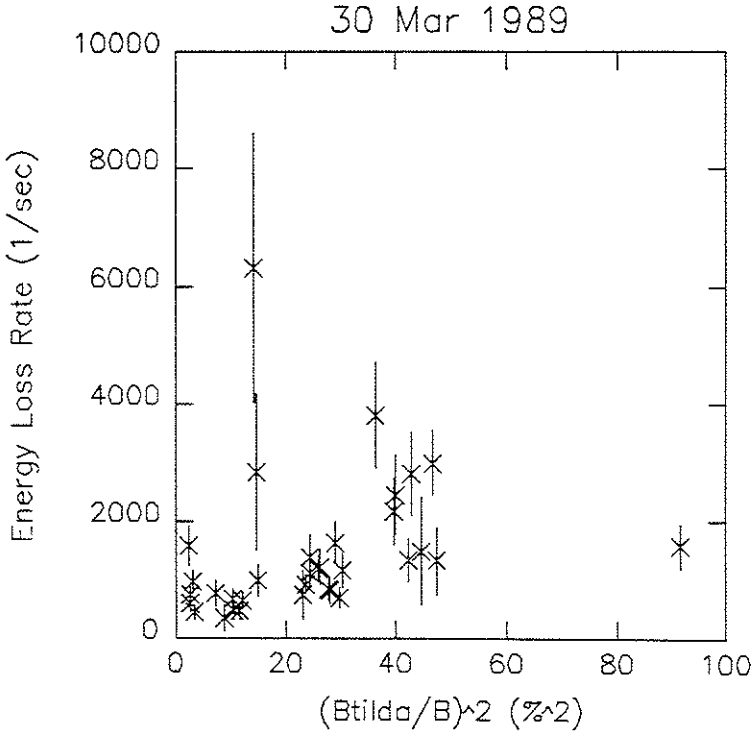


Figure VI.29: $\nu_E$ versus $(\tilde{B}/B)^2$ from an F-scan series.

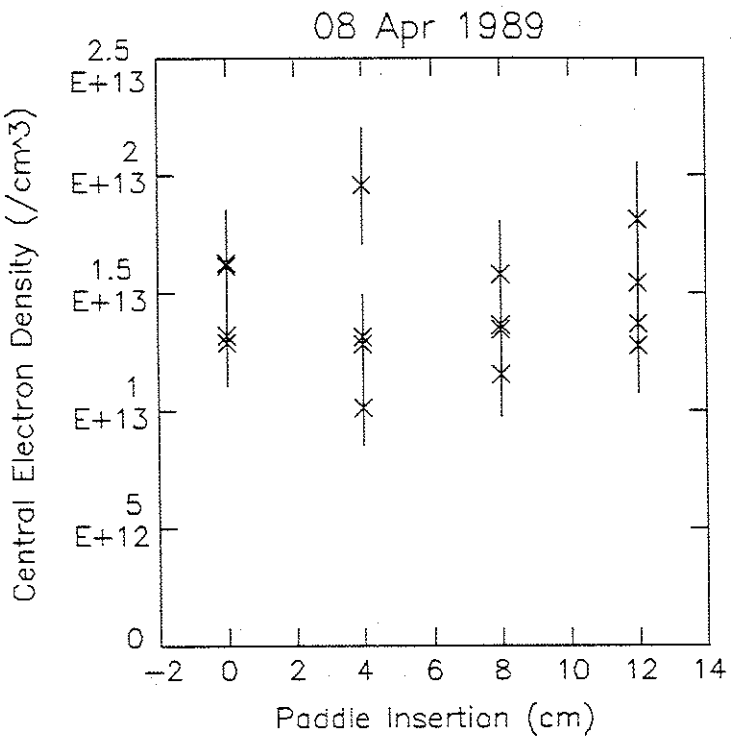


Figure VI.30: Central $n_e$ versus paddle insertion from a paddle limiter series. Each individual datum has been plotted.



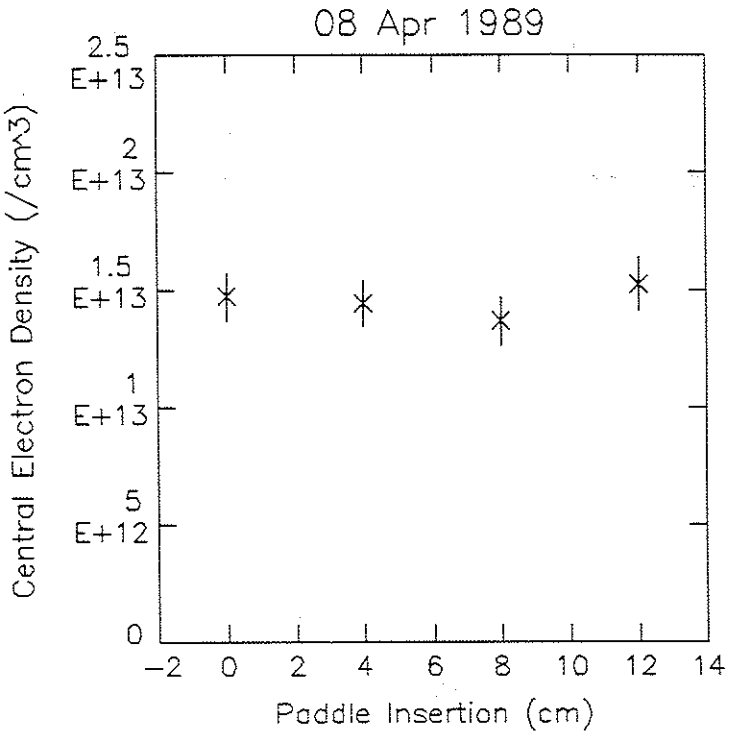


Figure VI.31: Mean central $n_e$ versus paddle insertion from a paddle limiter series. Each point is a weighted mean and uncertainty of the points plotted in Figure VI.30.

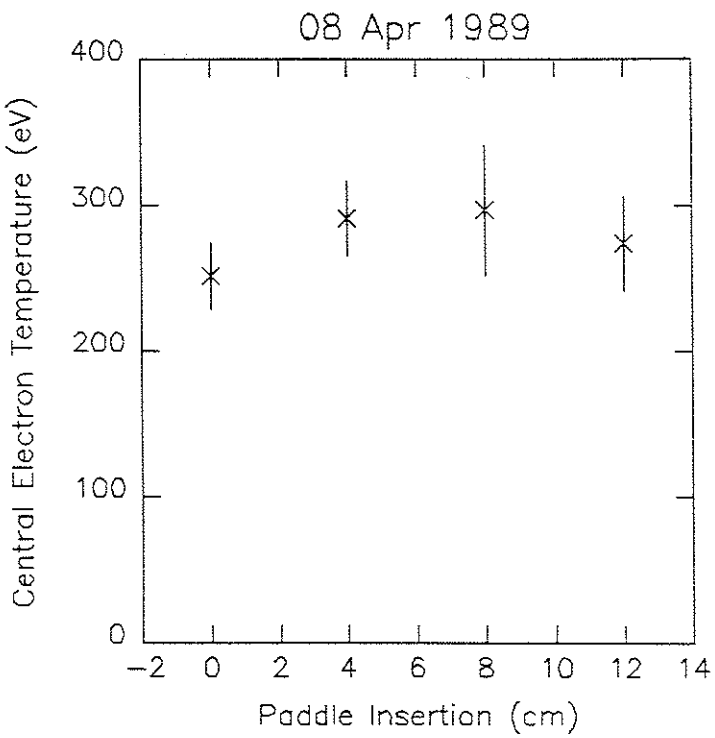


Figure VI.32: Mean central $T_e$ versus paddle insertion from a paddle limiter series.



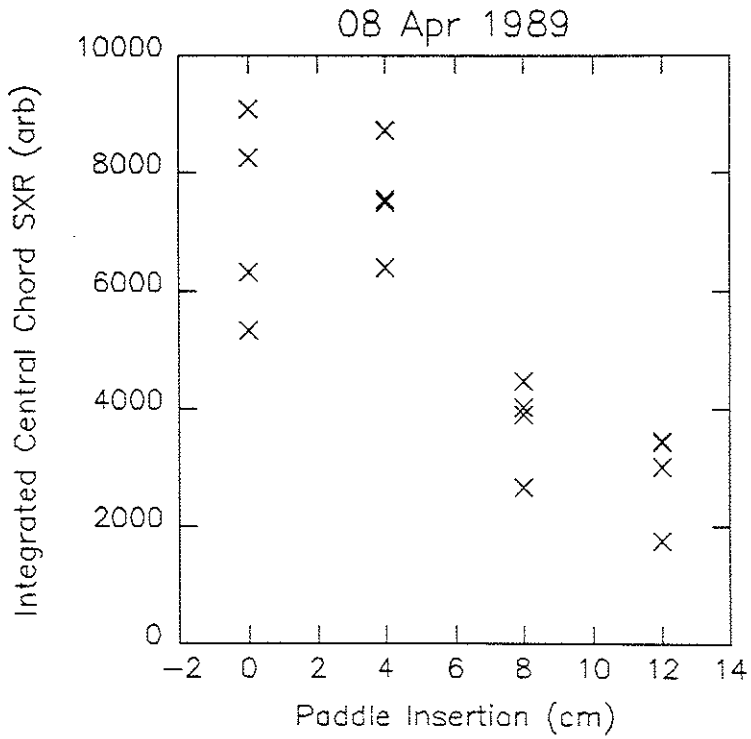


Figure VI.33: Central chord SXR versus paddle insertion from a paddle limiter series.

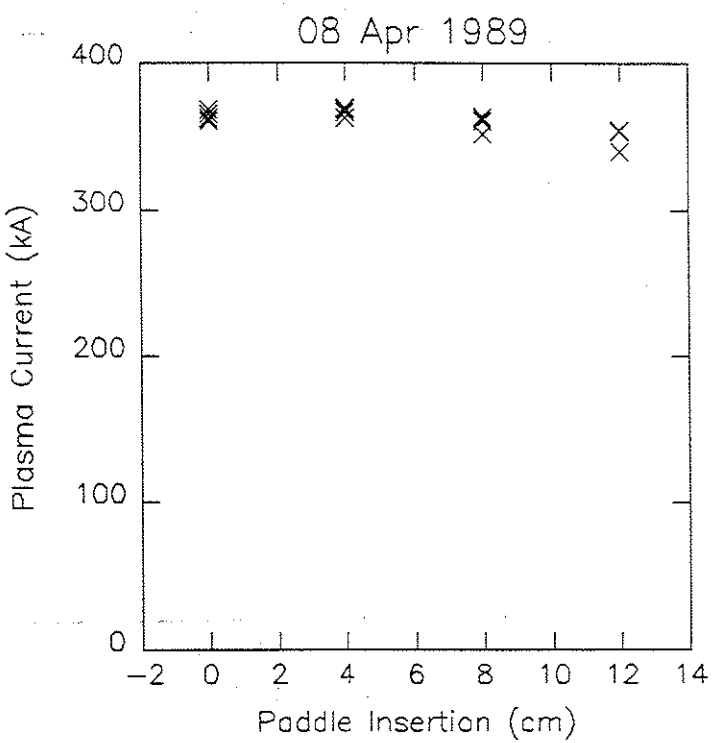


Figure VI.34: $I_p$ versus paddle insertion from a paddle limiter series.



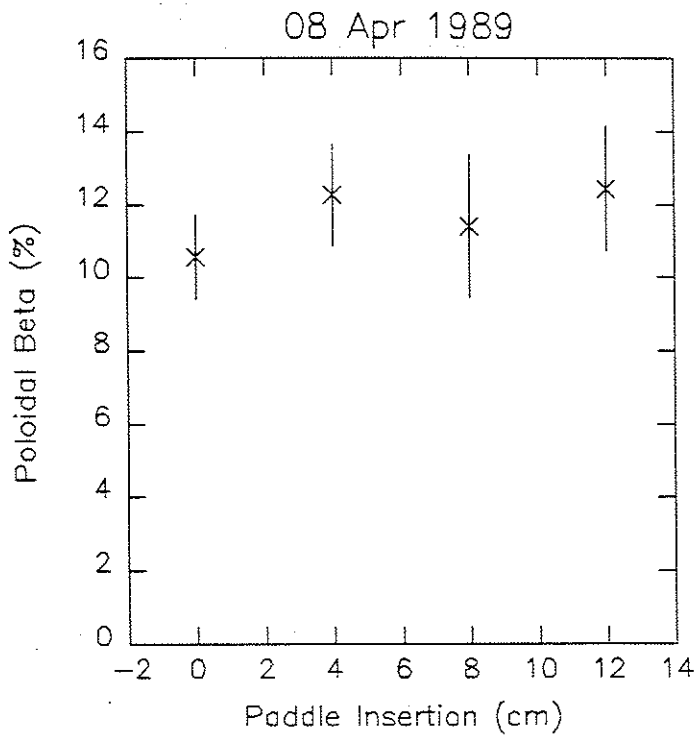


Figure VI.35: Mean $\beta_\theta$ versus paddle insertion from a paddle limiter series.

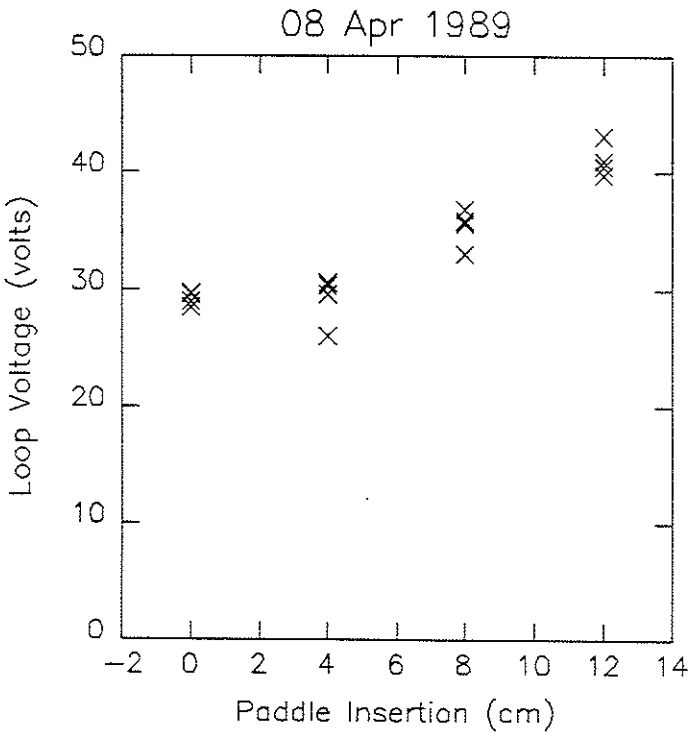


Figure VI.36: $V_\ell$ versus paddle insertion from a paddle limiter series.



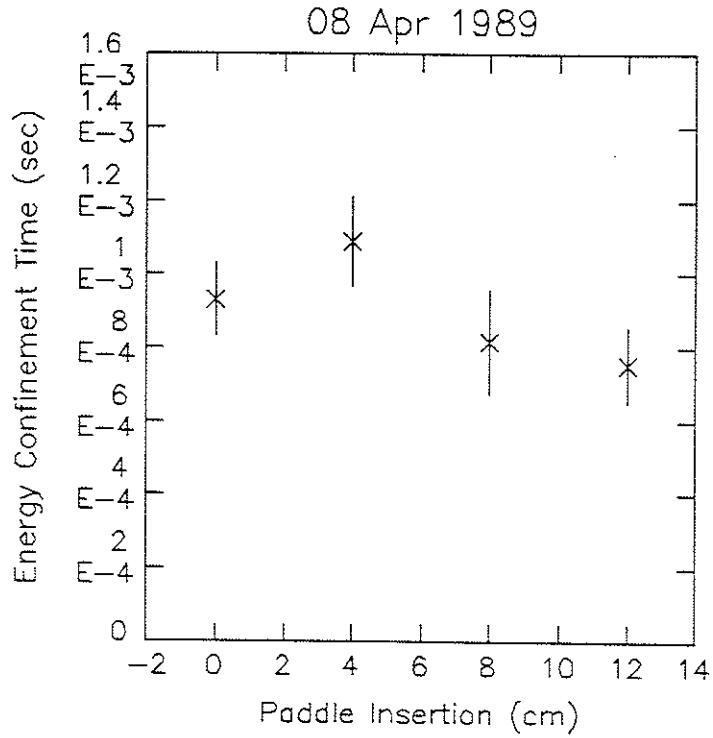


Figure VI.37: Mean $\tau_E$ versus paddle insertion from a paddle limiter series.

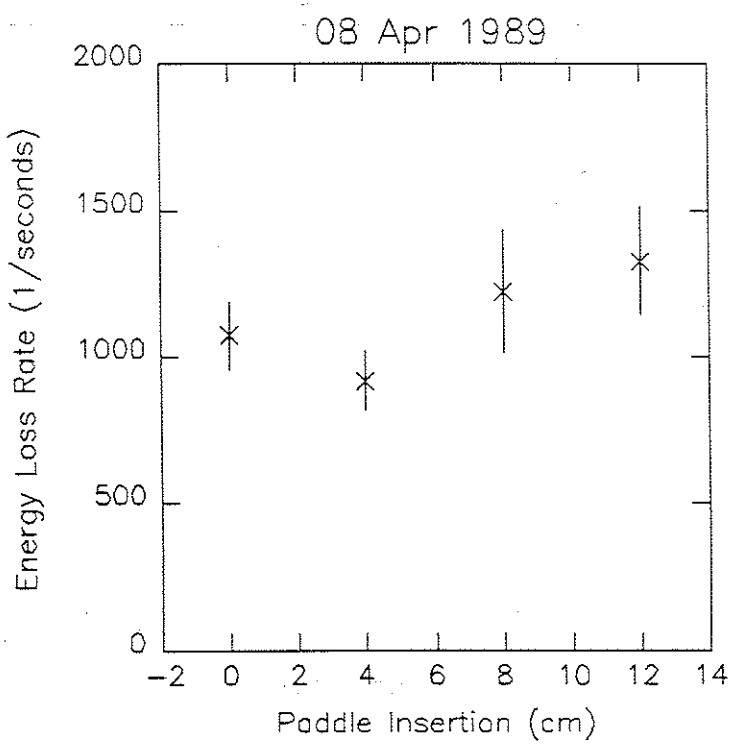


Figure VI.38: Mean $\nu_E$ versus paddle insertion from a paddle limiter series.



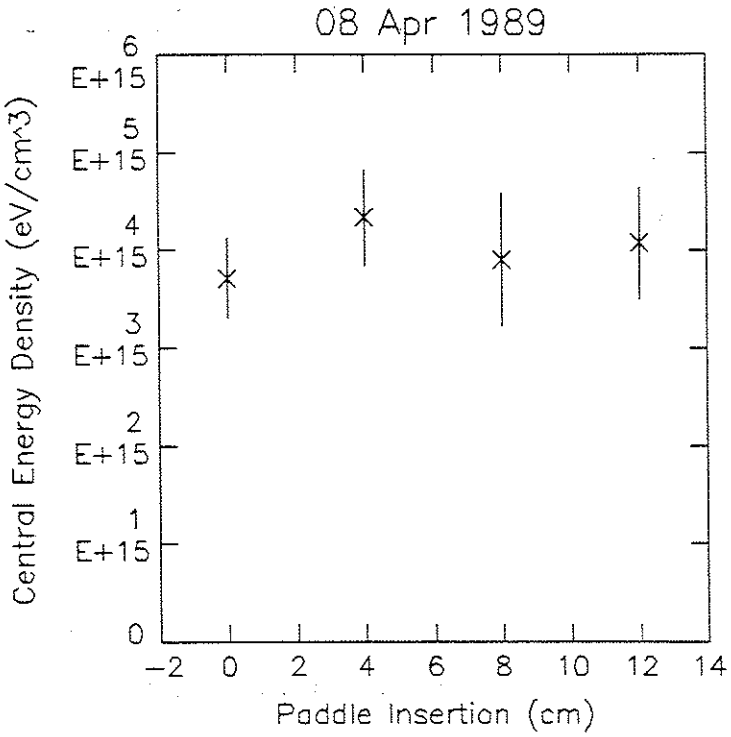


Figure VI.39: Mean $n_e T_e$ product versus paddle insertion from a paddle limiter series.

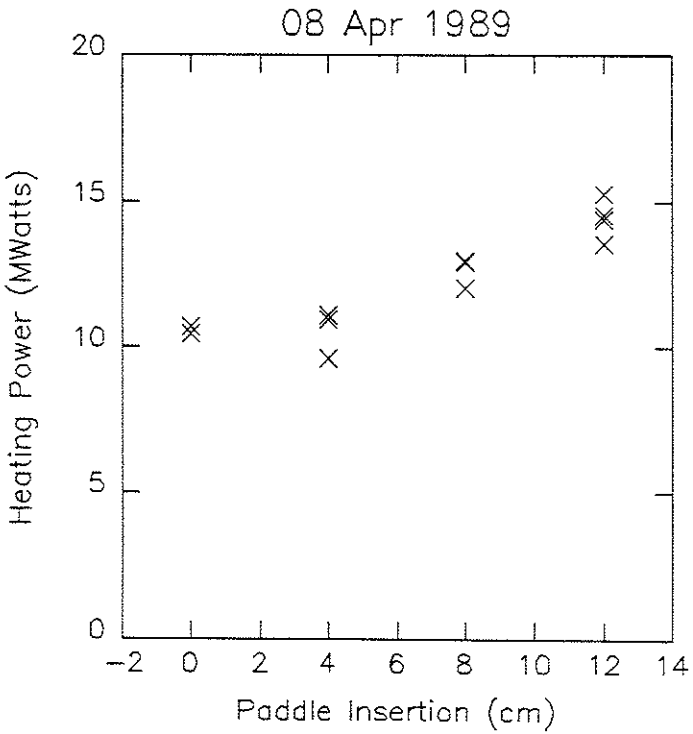


Figure VI.40: Heating power versus paddle insertion from a paddle limiter series.



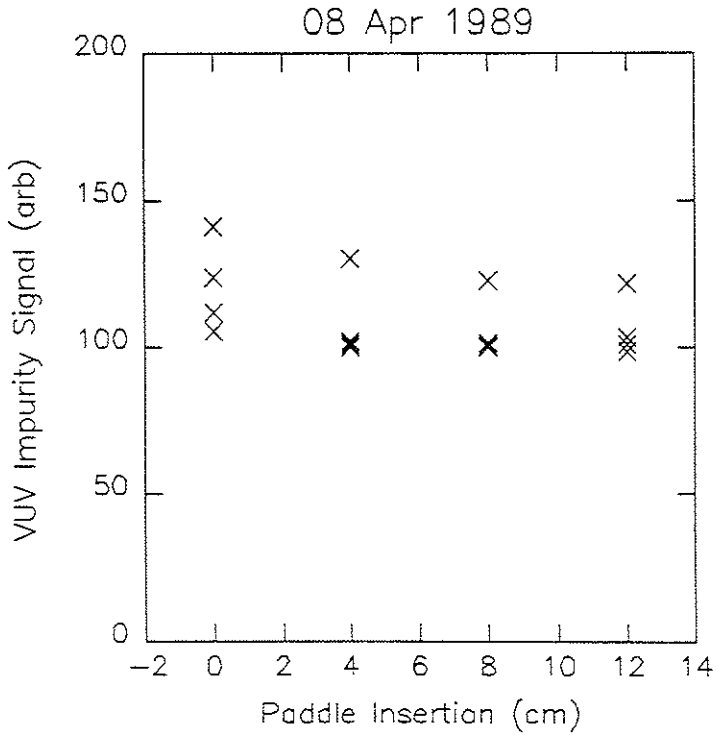


Figure VI.41: VUV impurity signal versus paddle insertion from a paddle limiter series.

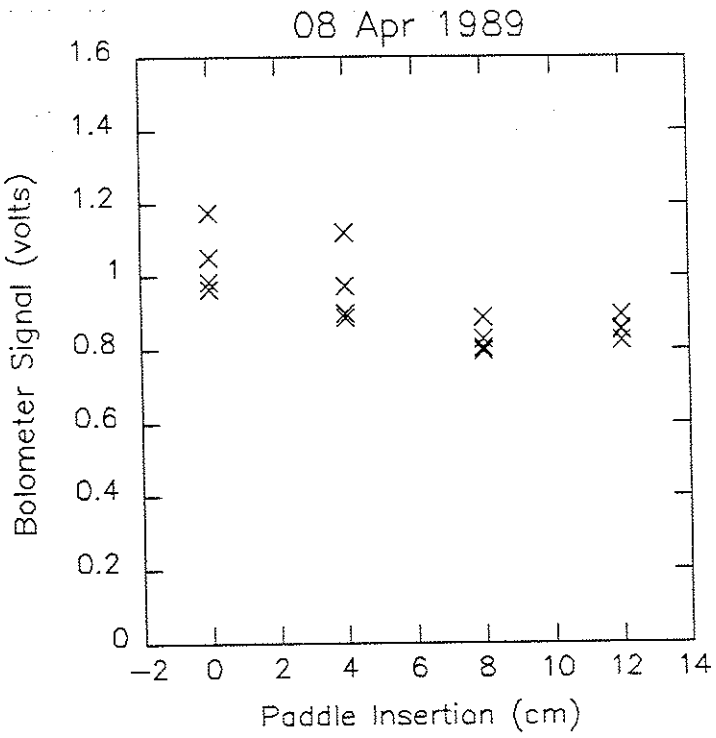


Figure VI.42: Bolometer signal versus paddle insertion from a paddle limiter series.



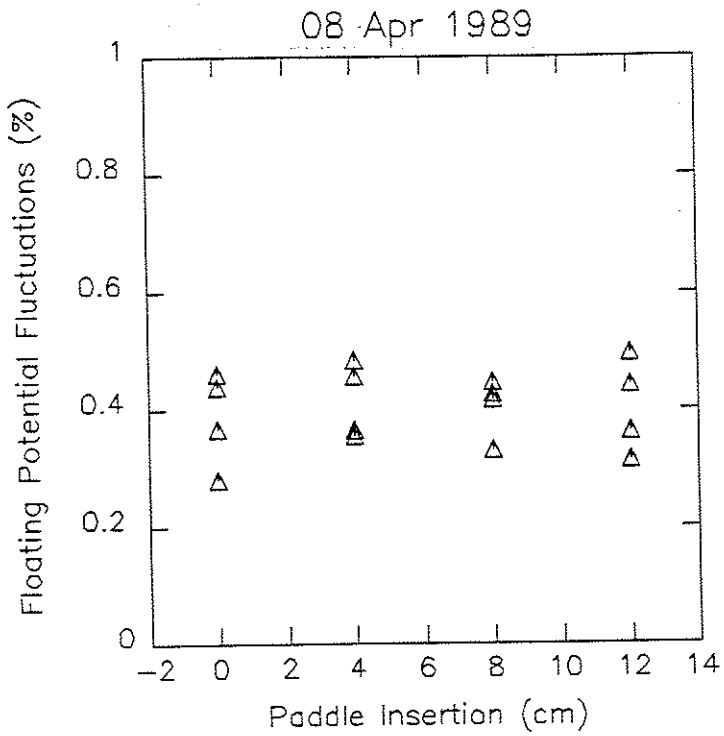


Figure VI.43: $\tilde{\phi}/\phi$ from right probe versus paddle insertion from a paddle limiter series. Right and left electrostatic probes were toroidally separated.

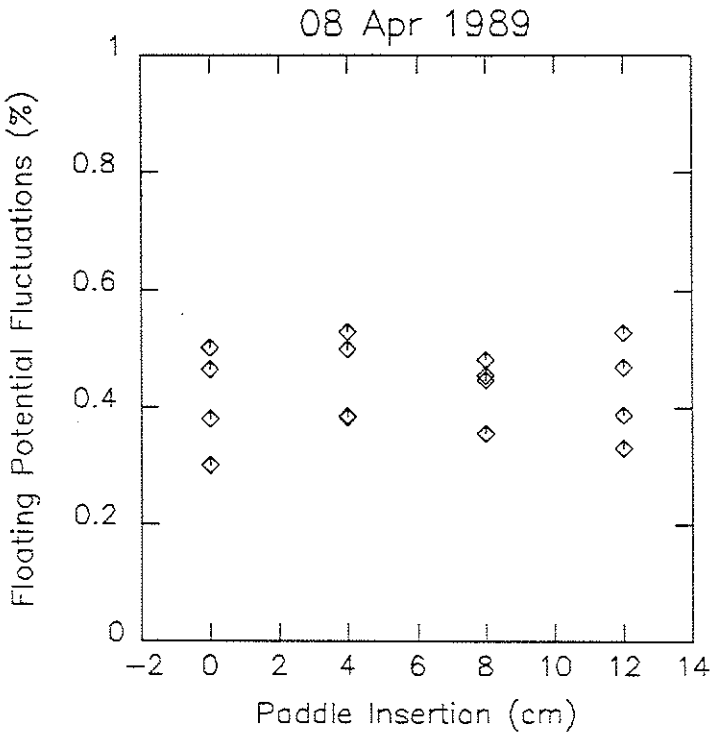


Figure VI.44: $\tilde{\phi}/\phi$ from left probe versus paddle insertion from a paddle limiter series.



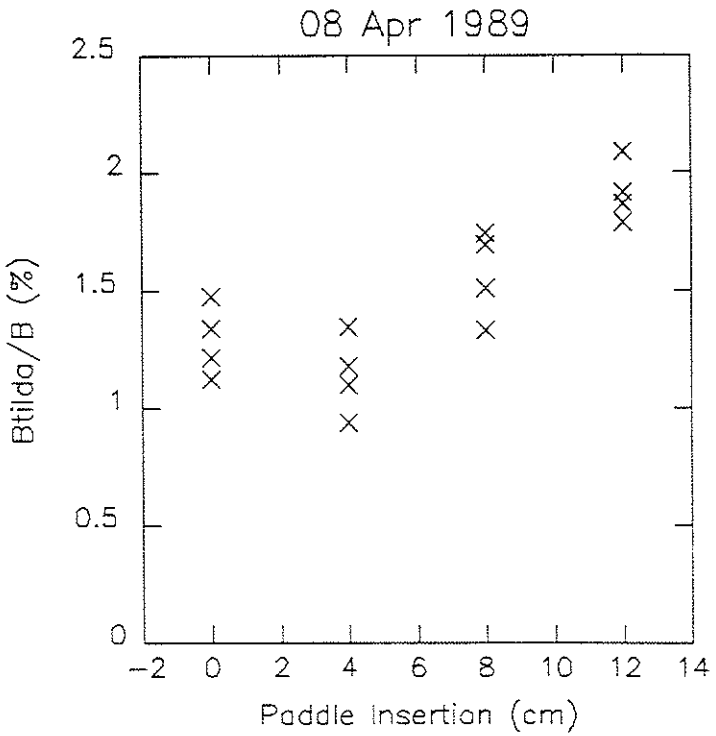


Figure VI.45: $\tilde{B}/B$ versus paddle insertion from a paddle limiter series.

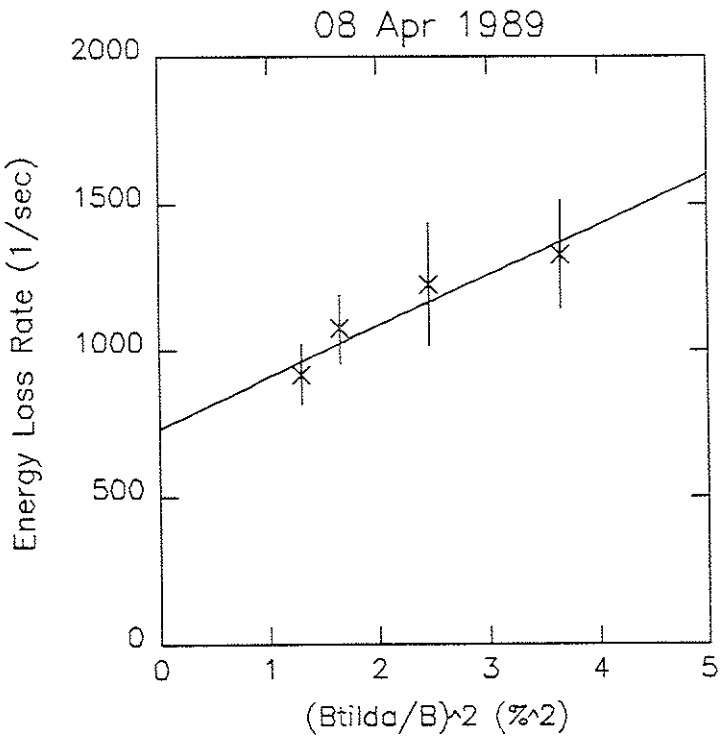


Figure VI.46: Mean $\nu_E$ versus $(\tilde{B}/B)^2$ from a paddle limiter series.



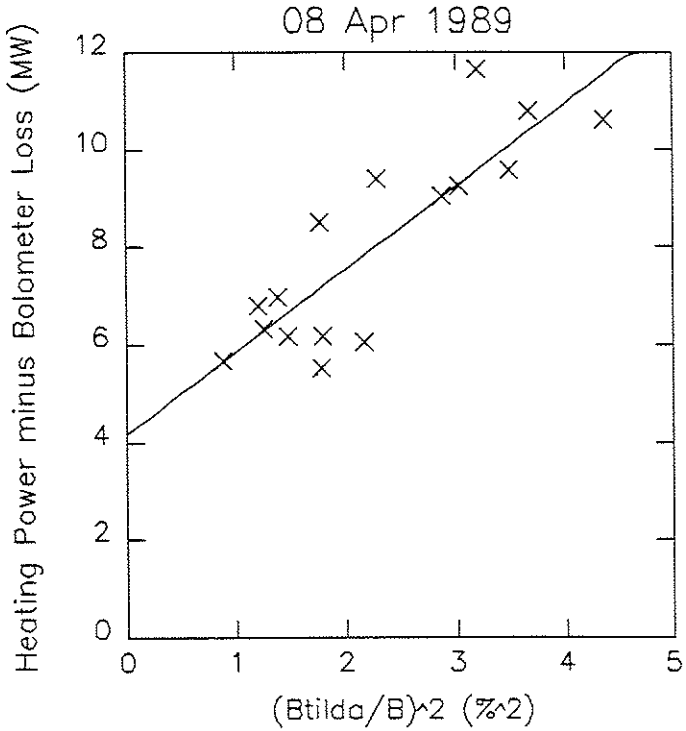


Figure VI.47: Heating power minus bolometer correlated power loss versus $(\tilde{B}/B)^2$ from a paddle insertion series.

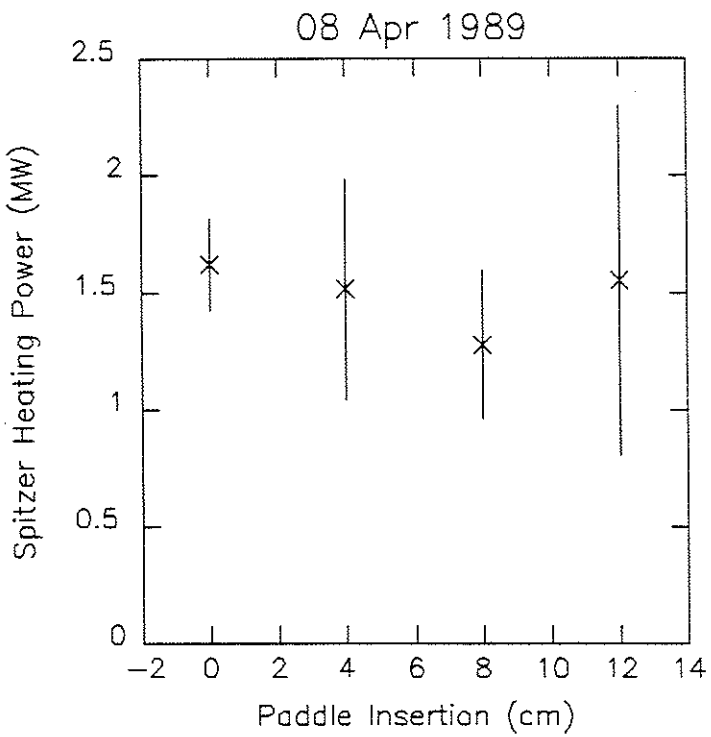


Figure VI.48: Mean Spitzer contribution to the heating power versus paddle insertion from a paddle limiter series.



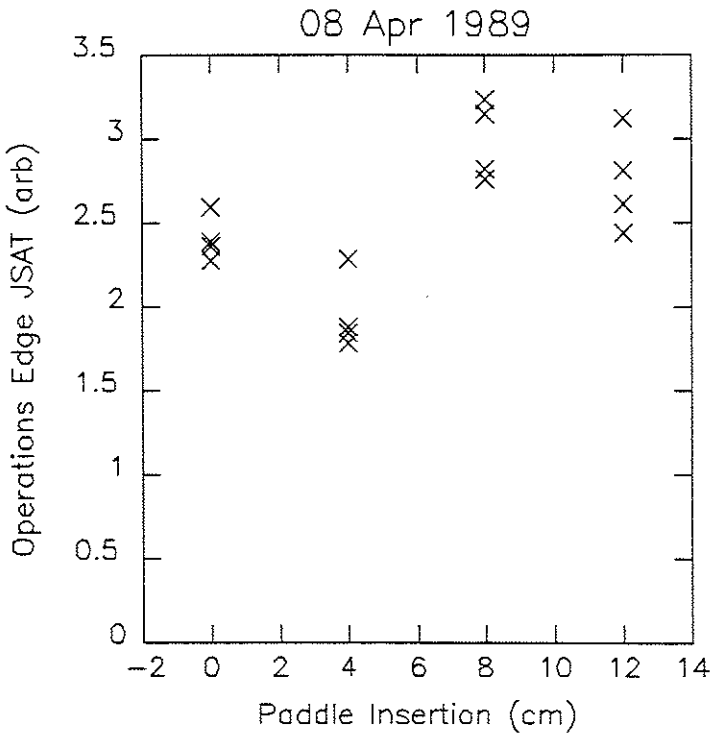


Figure VI.49: Edge saturation current probe signal versus paddle insertion from a paddle limiter series.

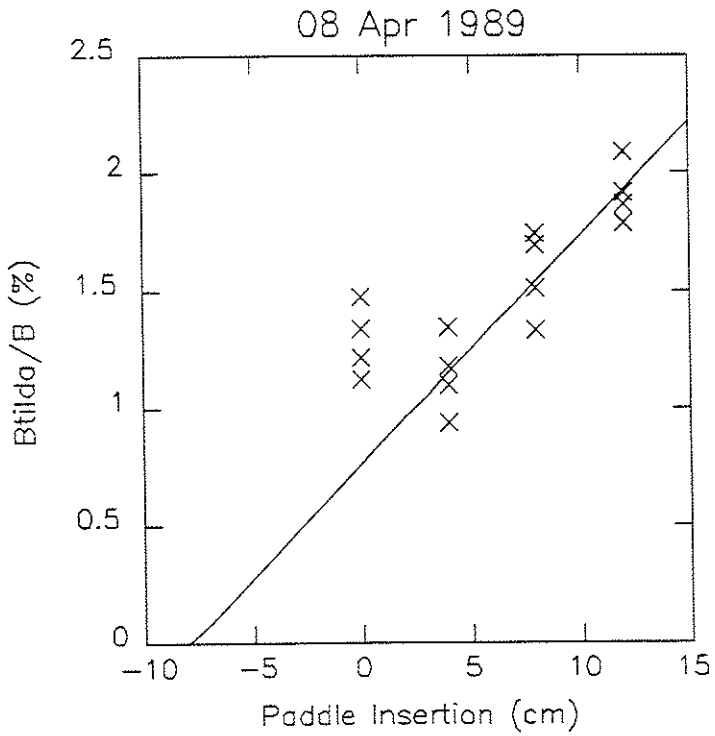


Figure VI.50: $\tilde{B}/B$ versus paddle insertion from a paddle limiter series.



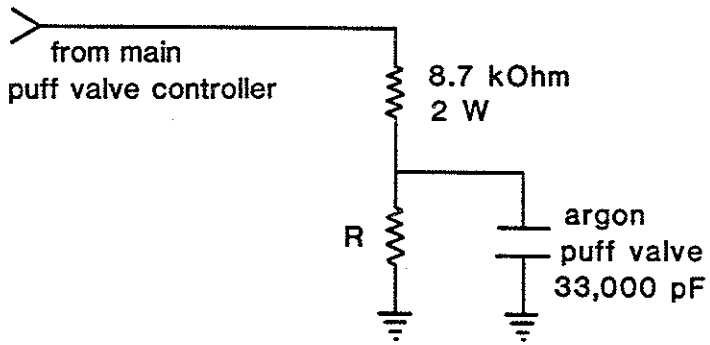


Figure VI.51: Circuit used to control amount of argon puffed into vacuum vessel during argon doping series. Resistor R is a 0 to 100 kΩ resistive divider box.

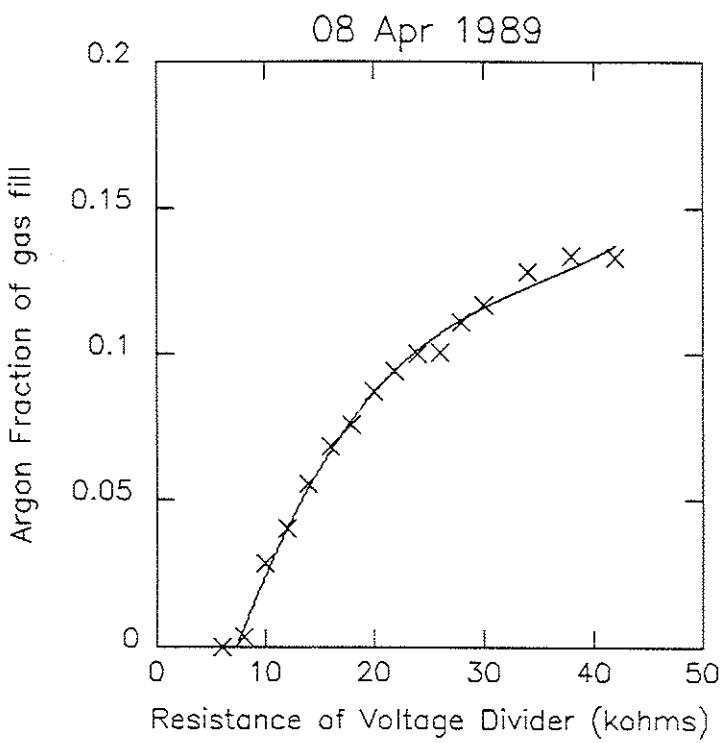


Figure VI.52: Argon fraction of gas fill versus resistance R of resistive divider box.



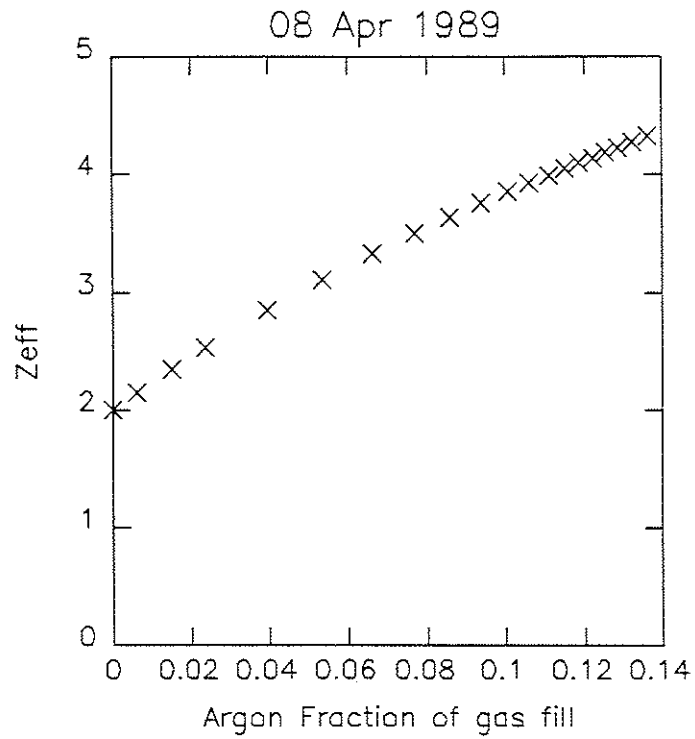


Figure VI.53: $Z_{eff}$ versus argon fraction of gas fill. See text for assumptions behind this calculation.

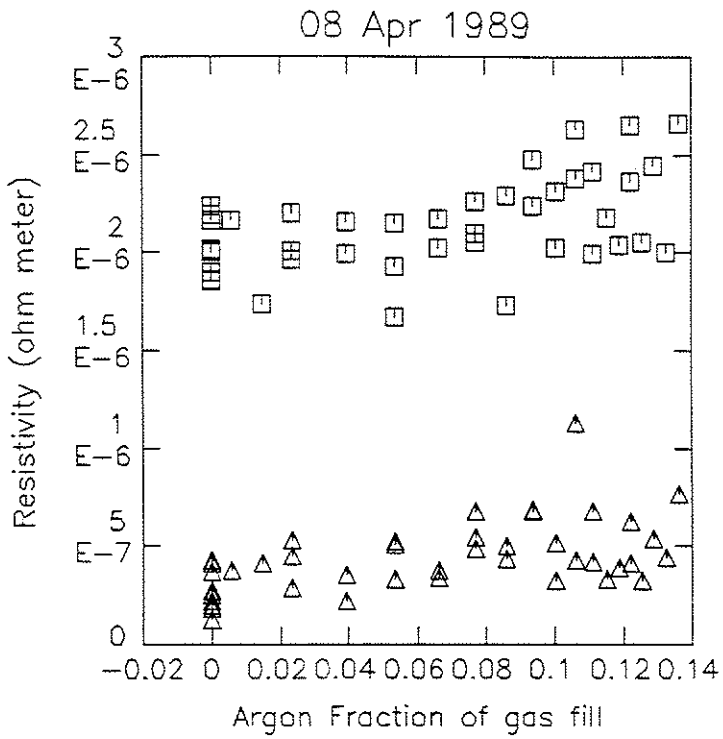


Figure VI.54: Measured parallel resistivity $\eta^*$ (square symbols) and Spitzer resistivity $\eta_{sp}$ (triangle" symbols) versus argon fraction from argon doping series.



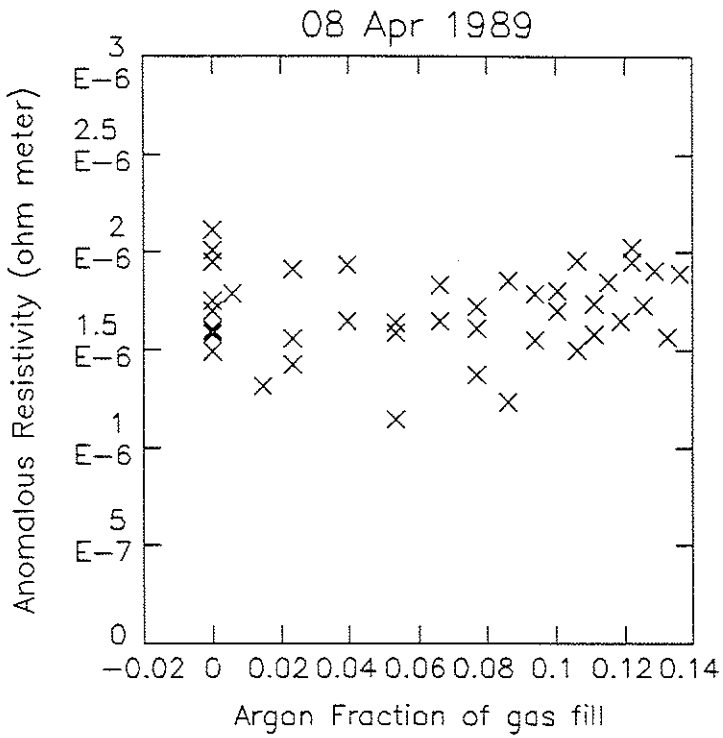


Figure VI.55: Anomalous resistivity ($\eta_{\parallel}^*-\eta_{sp}$) versus argon fraction from argon doping series.

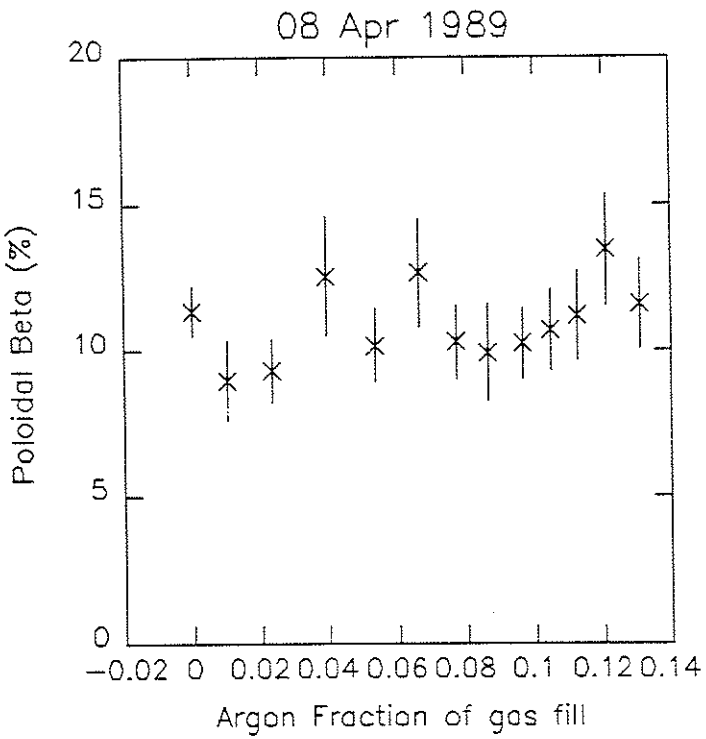


Figure VI.56: Mean $\beta_\theta$ versus argon fraction from argon doping series. The weighted means and associated uncertainties are averages of 2 to 4 individual points.



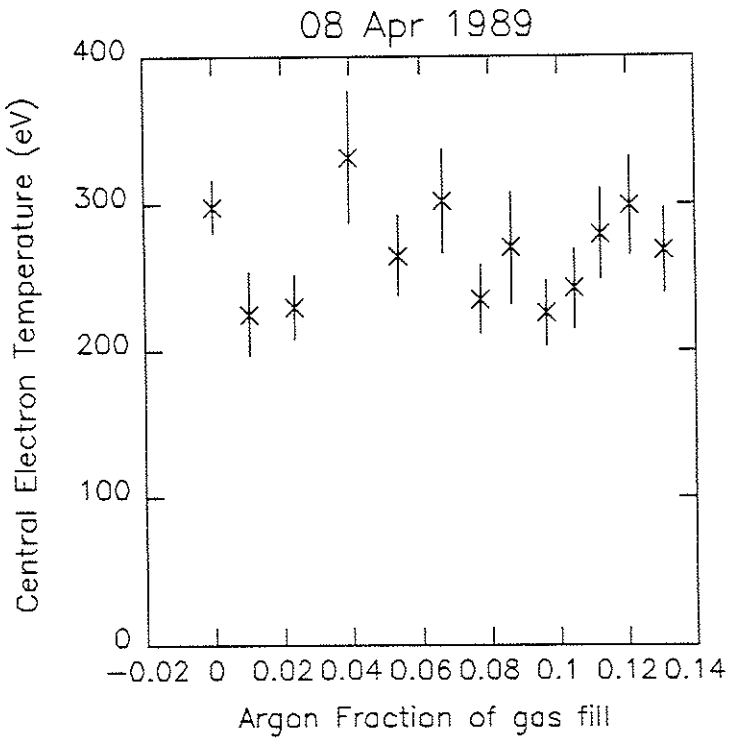


Figure VI.57: Mean central $T_e$ versus argon fraction from argon doping series.

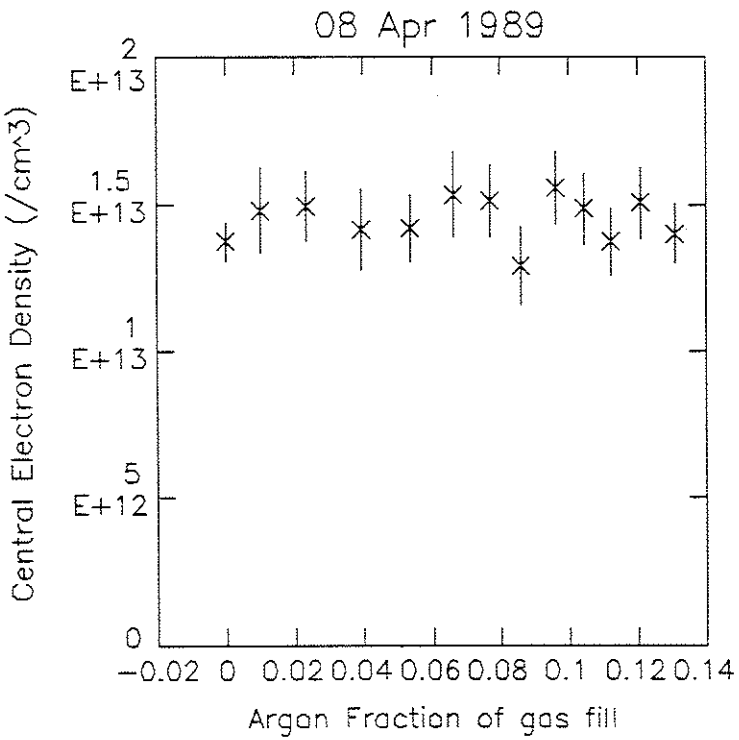


Figure VI.58: Mean central $n_e$ versus argon fraction from argon doping series.



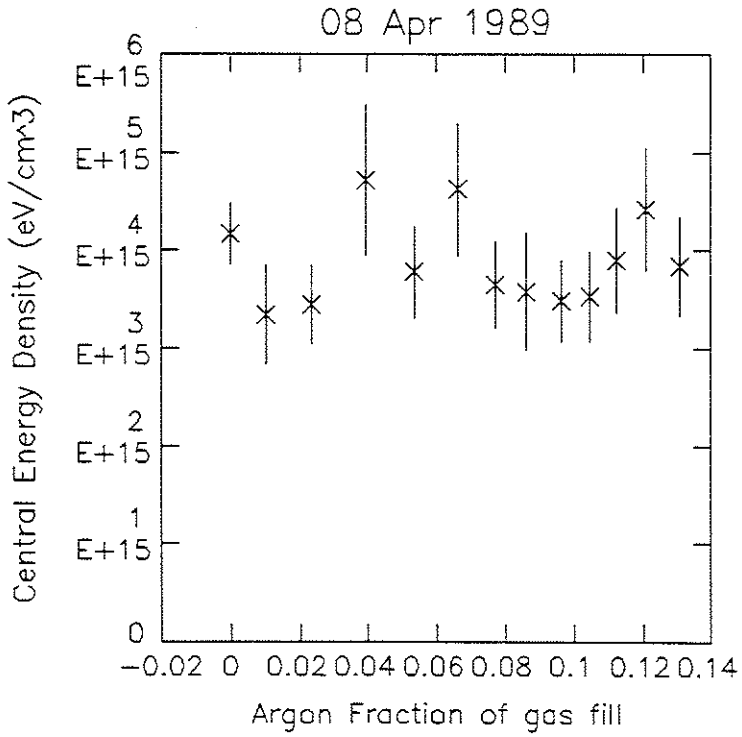


Figure VI.59: Mean central $n_eT_e$ product versus argon fraction from argon doping series.

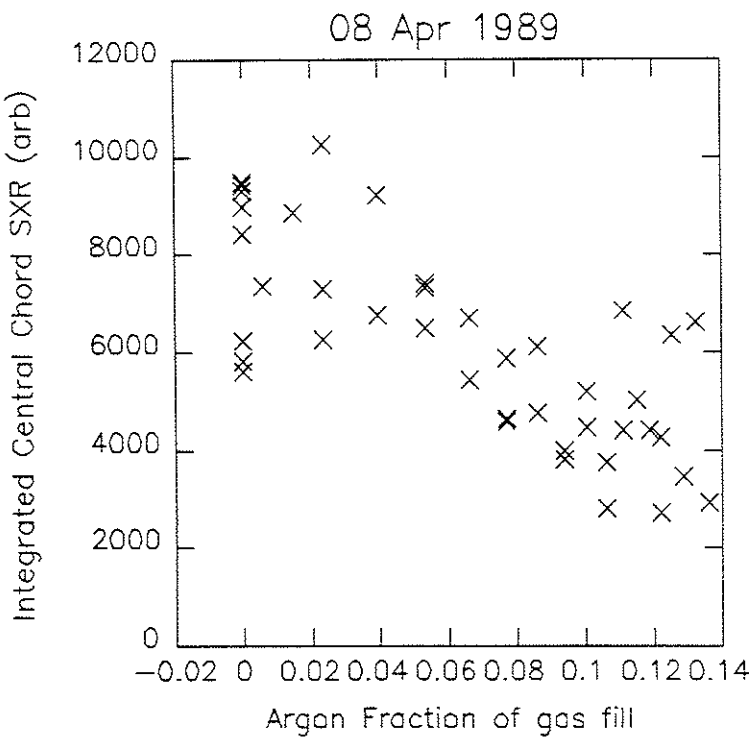


Figure VI.60: Central chord SXR versus argon fraction from argon doping series.



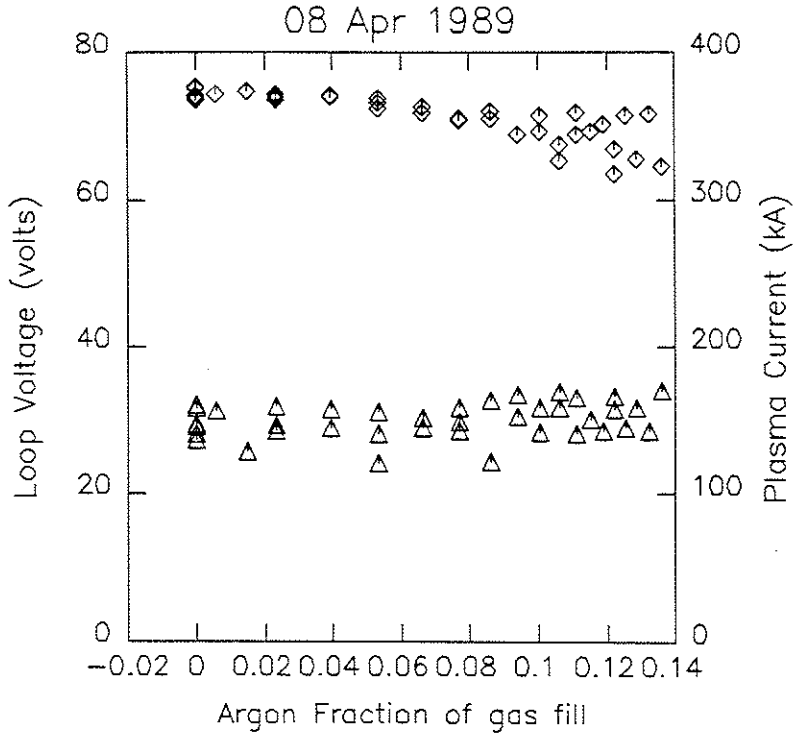


Figure VI.61: $V_\ell$ (triangle symbols) and $I_p$ (diamond symbols) versus argon fraction from argon doping series.

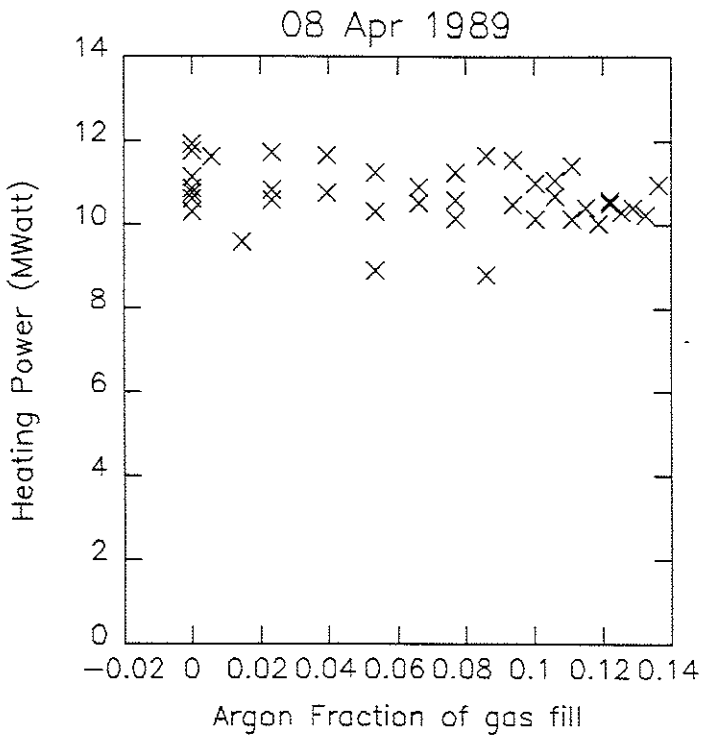


Figure VI.62: Heating power versus argon fraction from argon doping series.



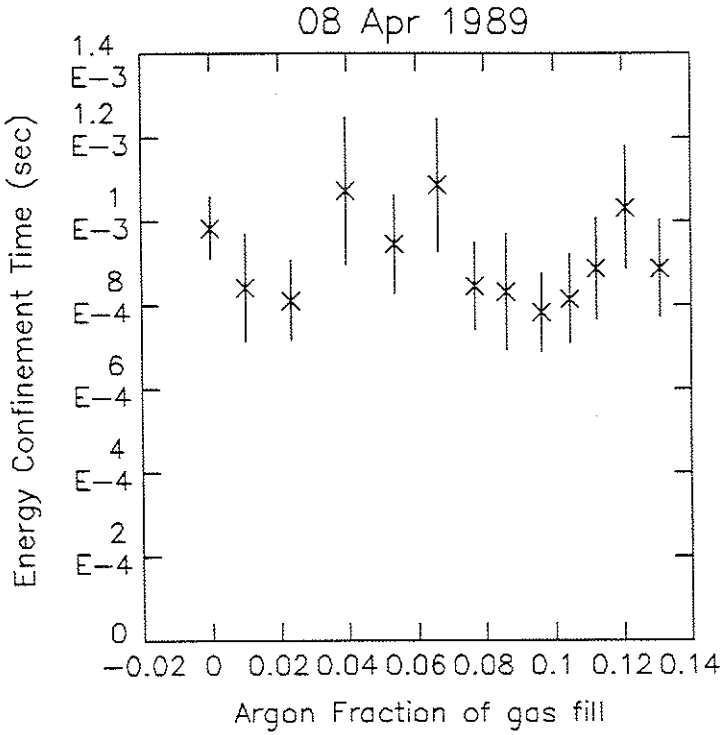


Figure VI.63: Mean $\tau_E$ versus argon fraction from argon doping series.

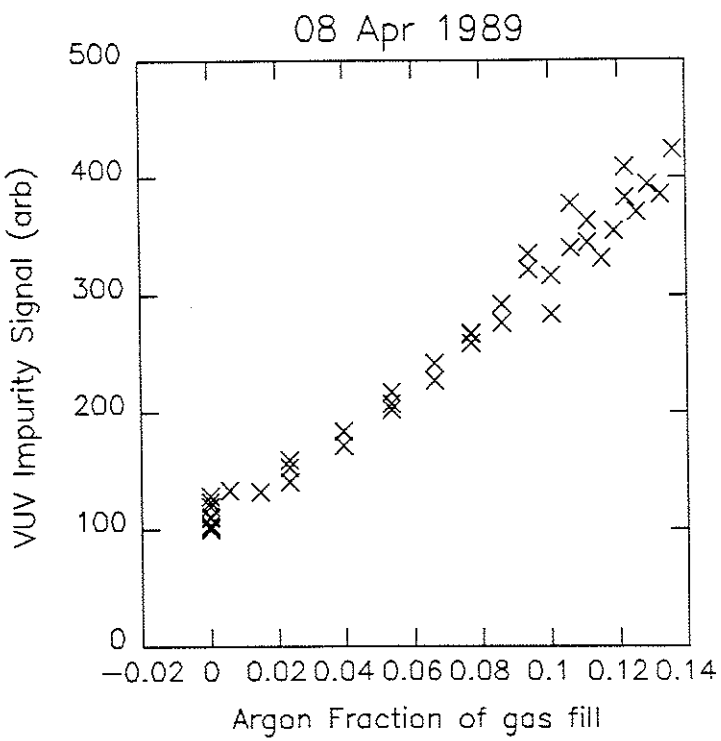


Figure VI.64: VUV impurity signal versus argon fraction from argon doping series.



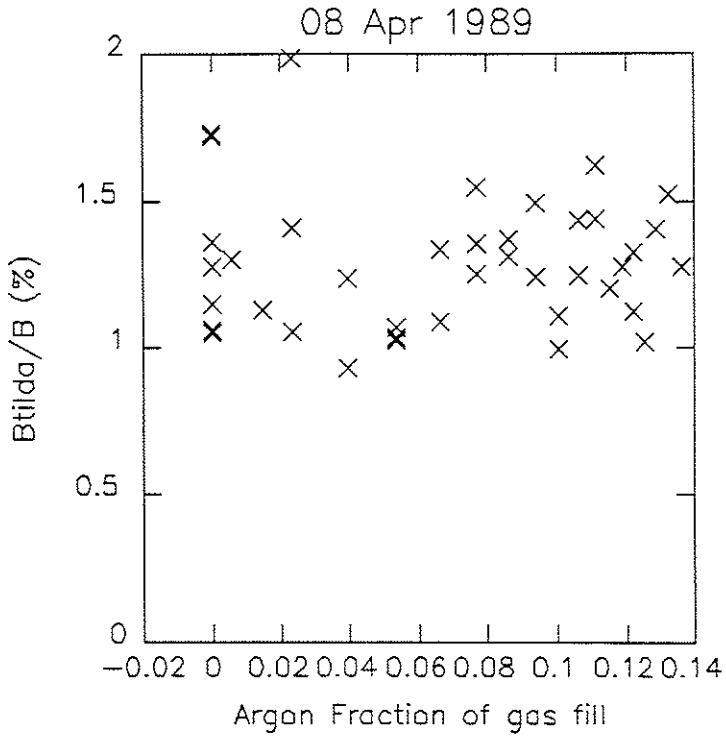


Figure VI.65: $\tilde{B}/B$ versus argon fraction from argon doping series.

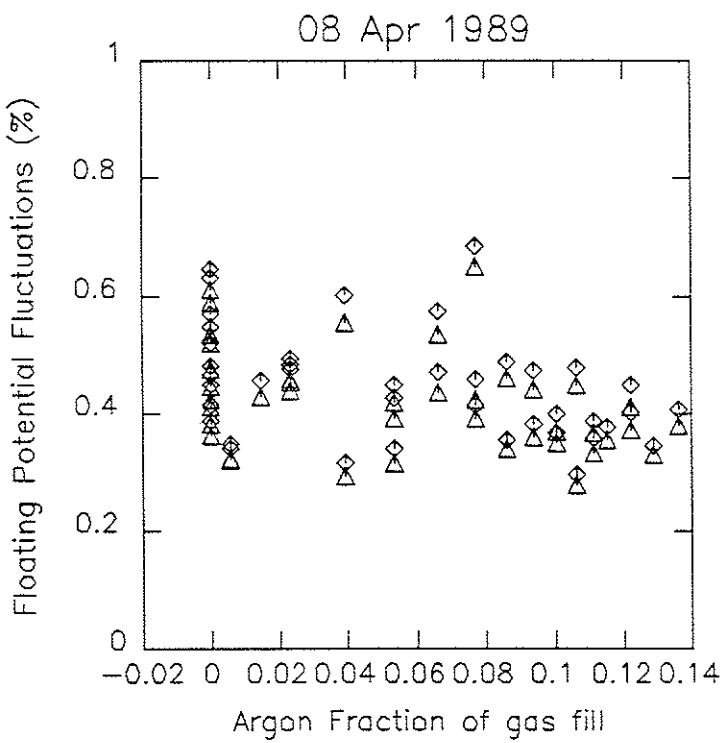


Figure VI.66: $\tilde{\phi}/\phi$ from right and left probes versus argon fraction from argon doping series.



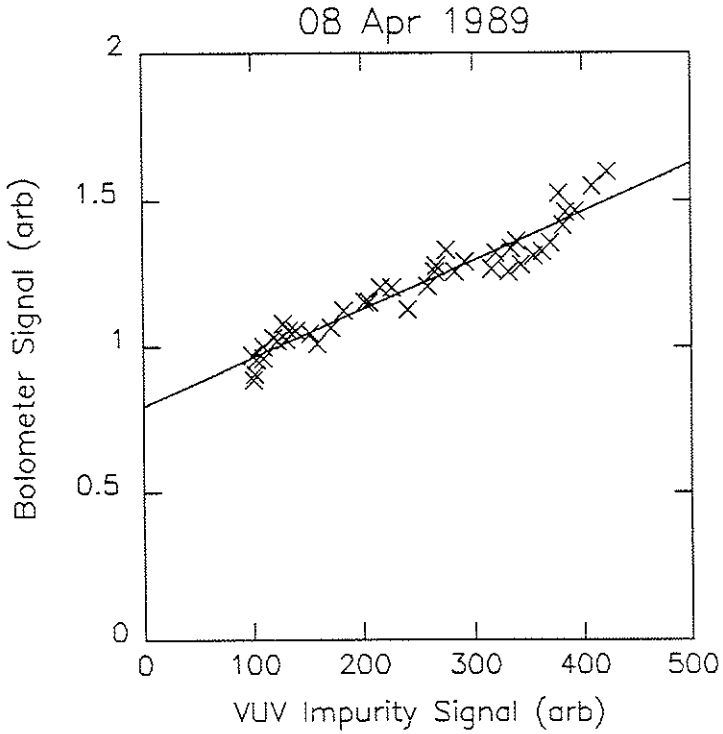


Figure VI.67: Bolometer signal versus VUV impurity signal from argon doping series.

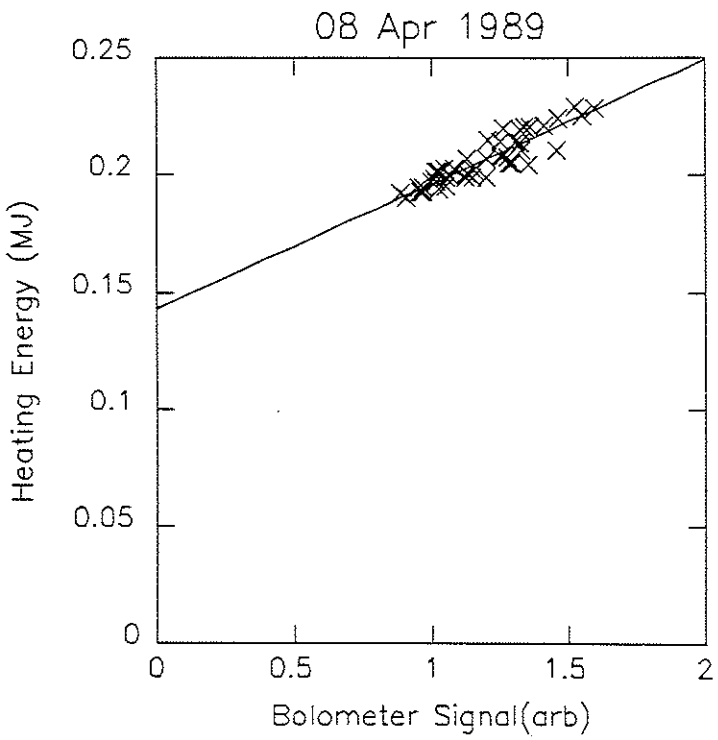


Figure VI.68: Heating energy versus bolometer signal from argon doping series.



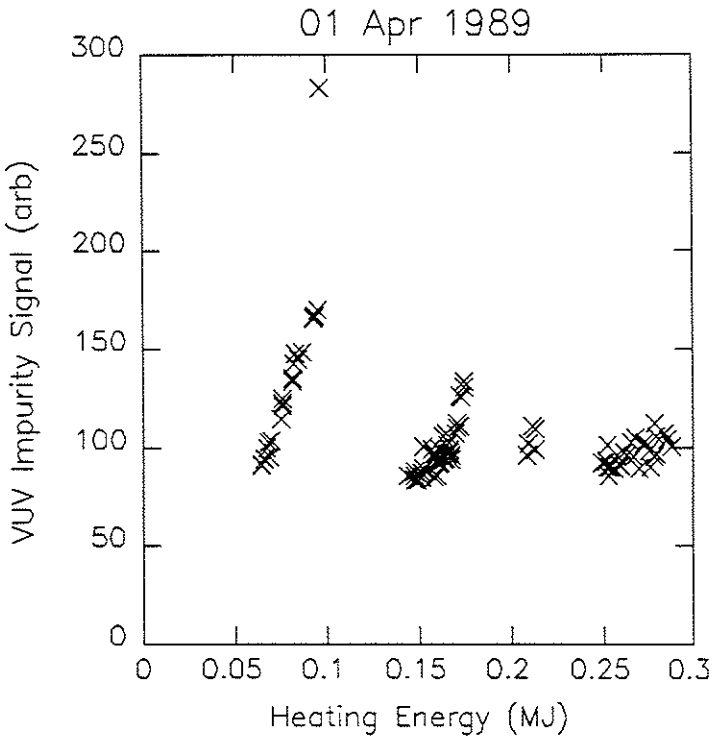


Figure VI.69: VUV impurity signal versus heating energy from plasma current scan series.

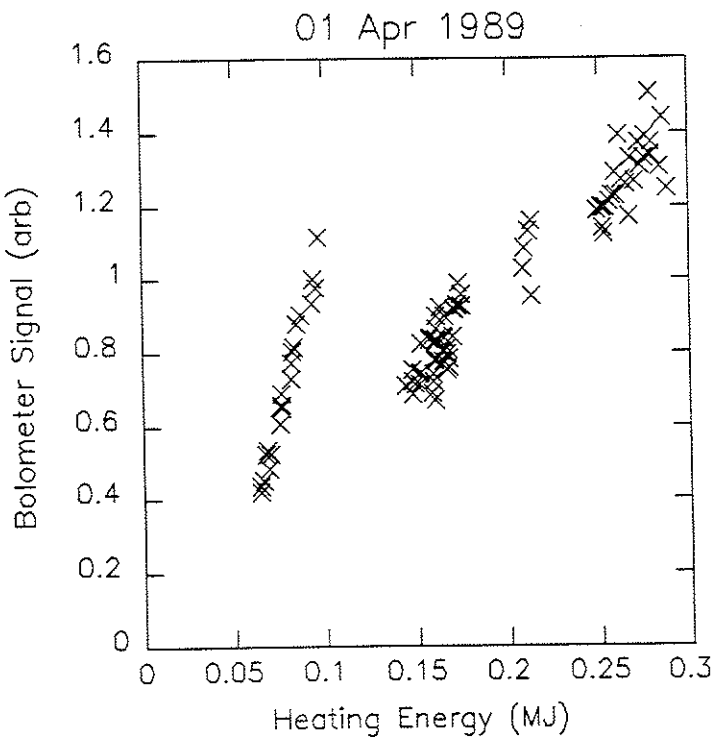


Figure VI.70: Bolometer signal versus heating energy from plasm current scan series.



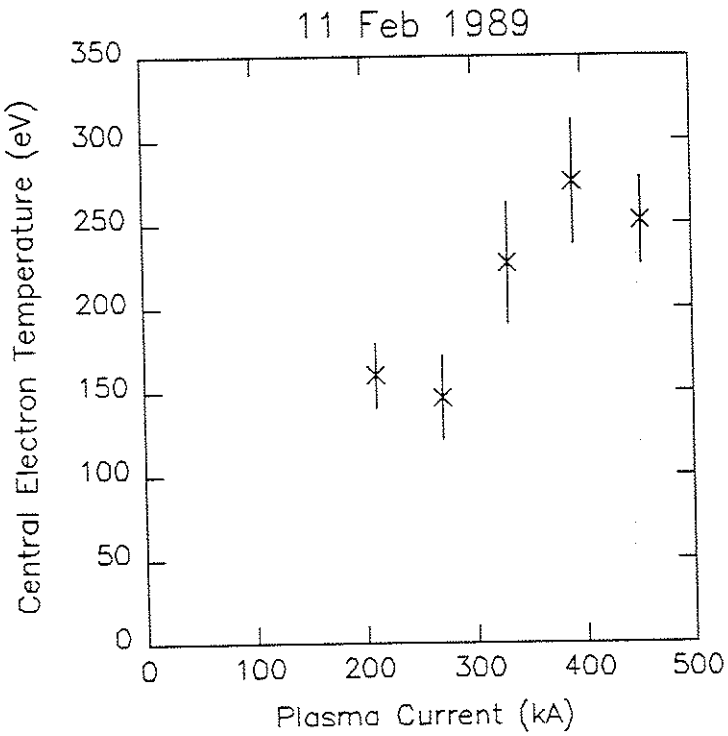


Figure VI.71: Mean central $T_e$ versus $I_p$ from plasma current scan series.

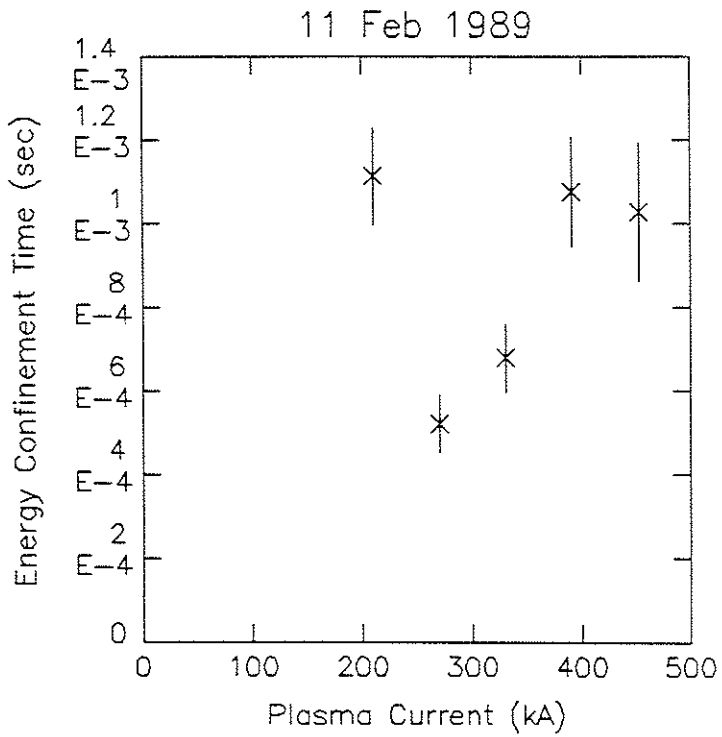


Figure VI.72: Mean $\tau_E$ versus $I_p$ from plasma current scan series.



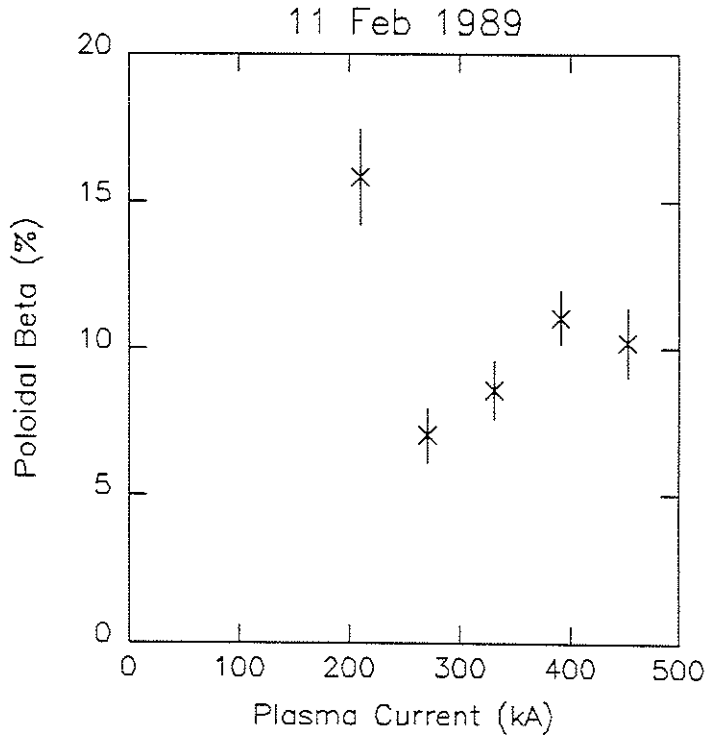


Figure VI.73: Mean $\beta_\theta$ versus $I_p$ from plasma current scan series.

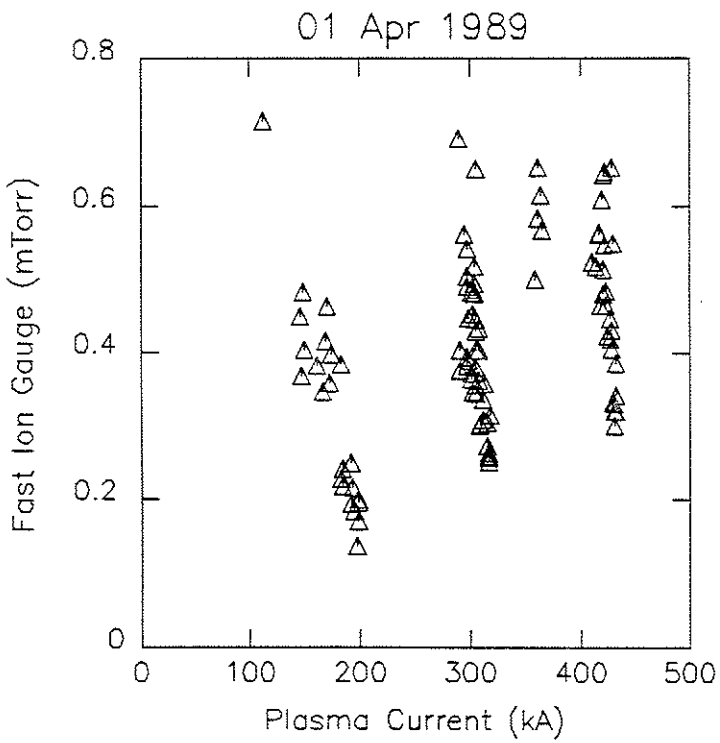


Figure VI.74: Fast ion gauge versus $I_p$ from plasma current scan series.



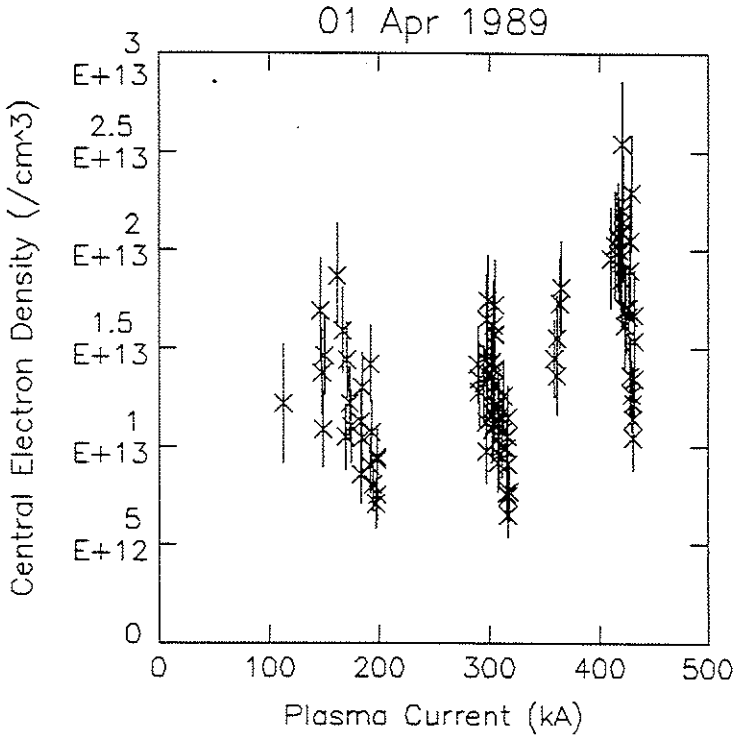


Figure VI.75: Central $n_e$ versus $I_p$ from plasma current scan series.

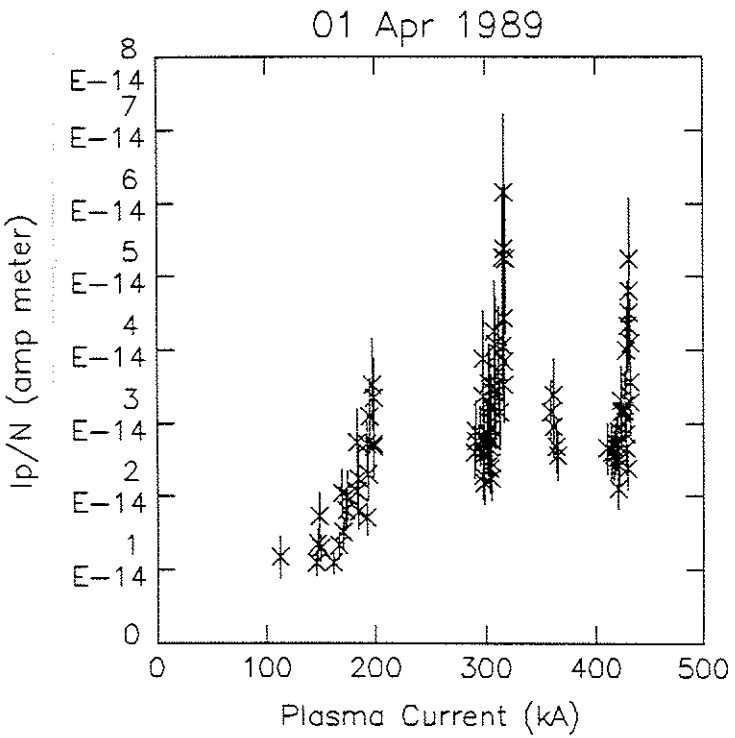


Figure VI.76: $I_p/N$ versus $I_p$ from plasma current scan series.



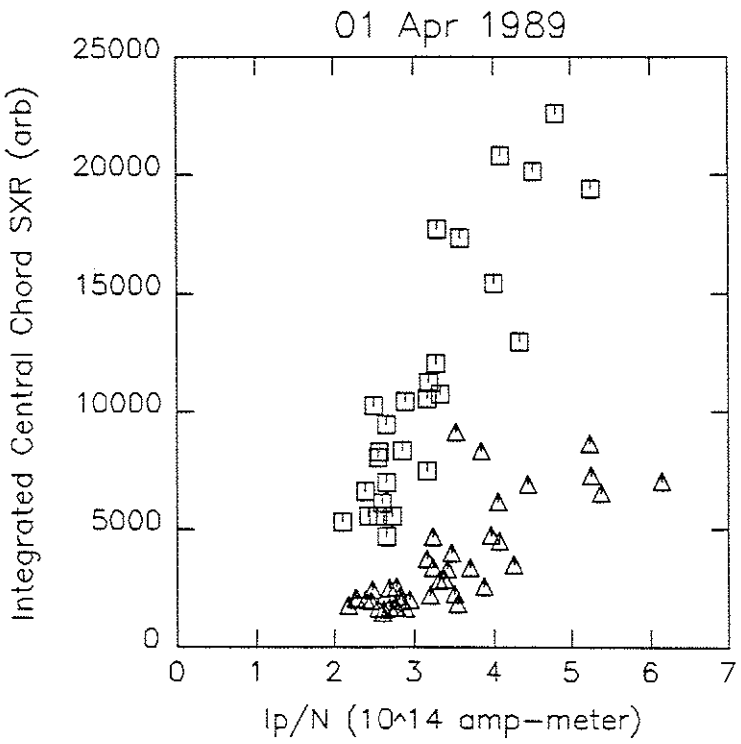


Figure VI.77: Central chord SXR versus $I_p/N$ from plasma current scan series. Square symbols represent ~400 kA discharges, triangle symbols represent ~300 kA discharges.

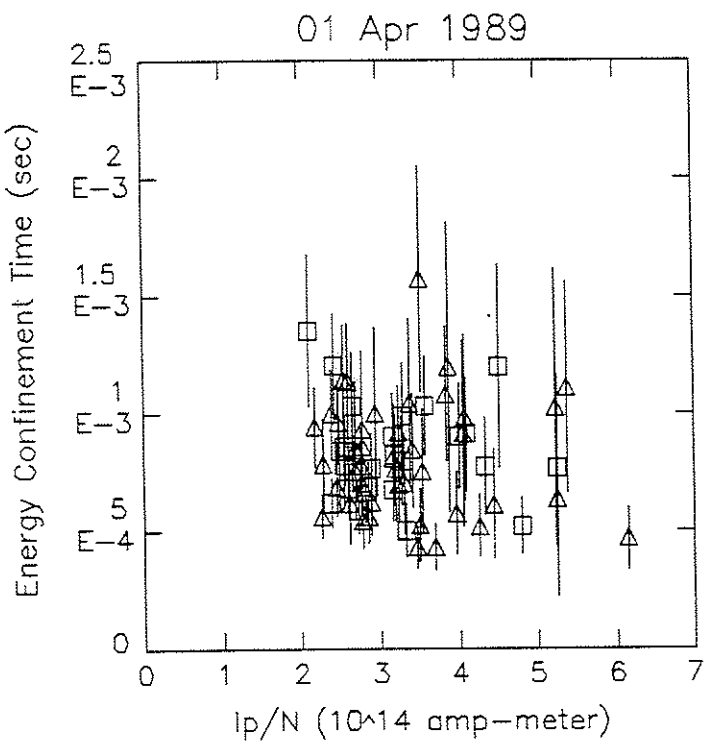


Figure VI.78: $\tau_E$ versus $I_p/N$ for the two groups of discharges plotted in Figure VI.77.



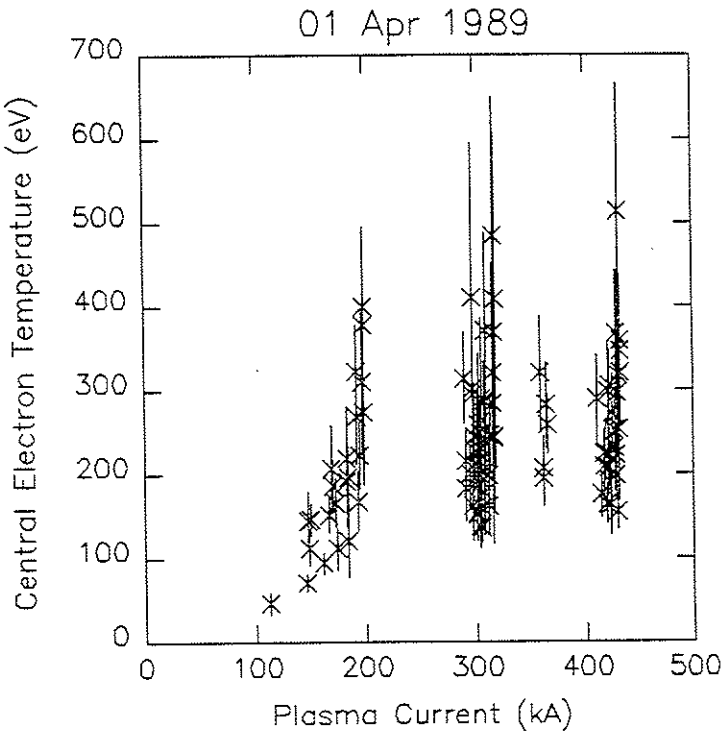


Figure VI.79: Central $T_e$ versus $I_p$ from plasma current scan series.

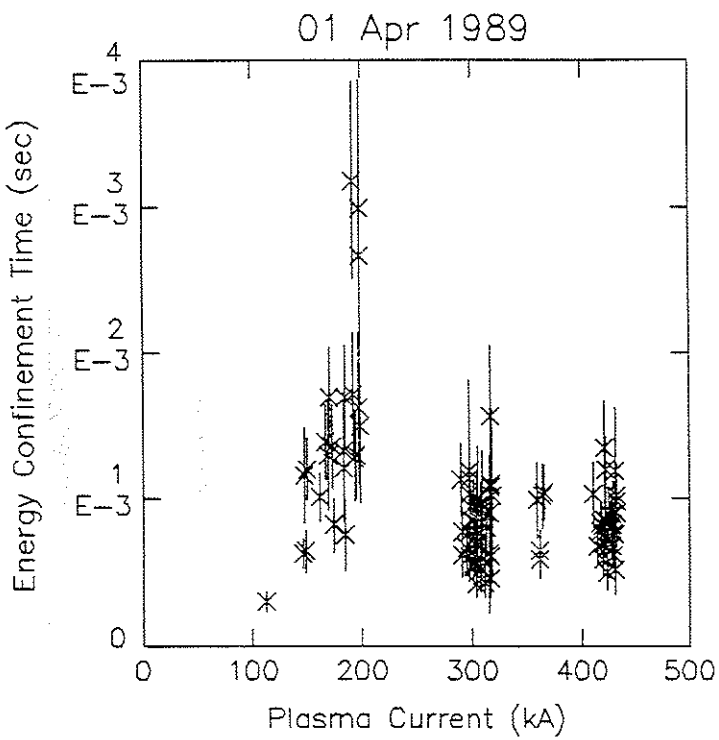


Figure VI.80: $\tau_E$ versus $I_p$ from plasma current scan series.



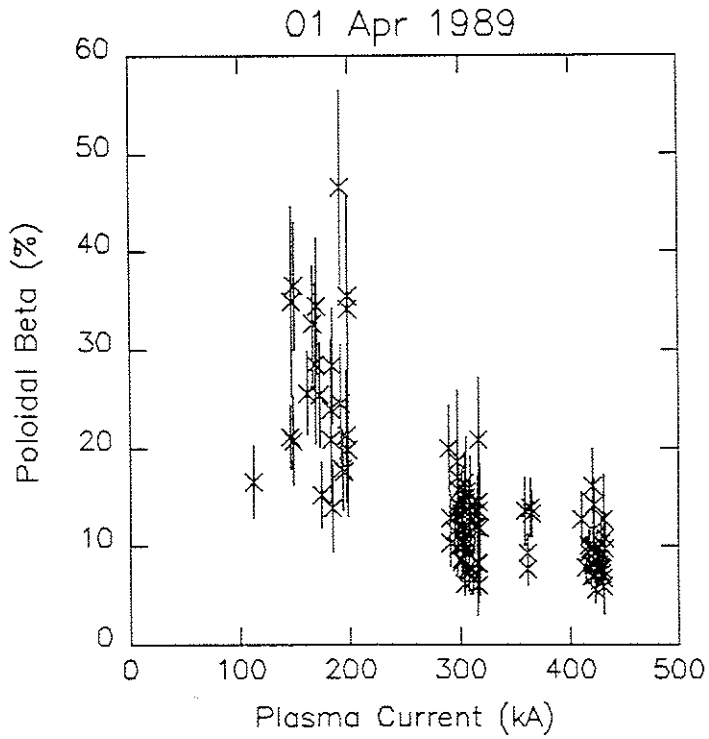


Figure VI.81: $\beta_\theta$ versus $I_p$ from plasma current scan series.

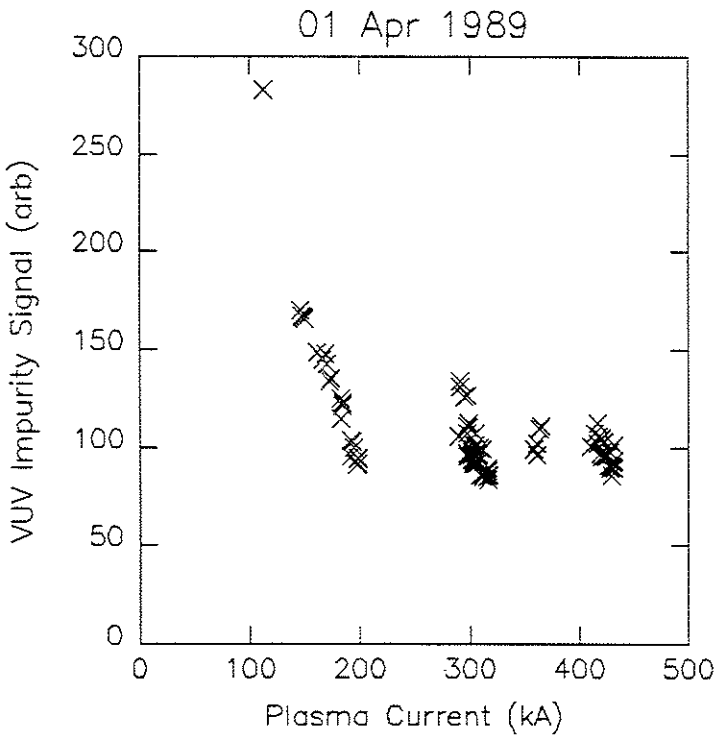


Figure VI.82: VUV impurity signal versus $I_p$ from plasma current scan series.



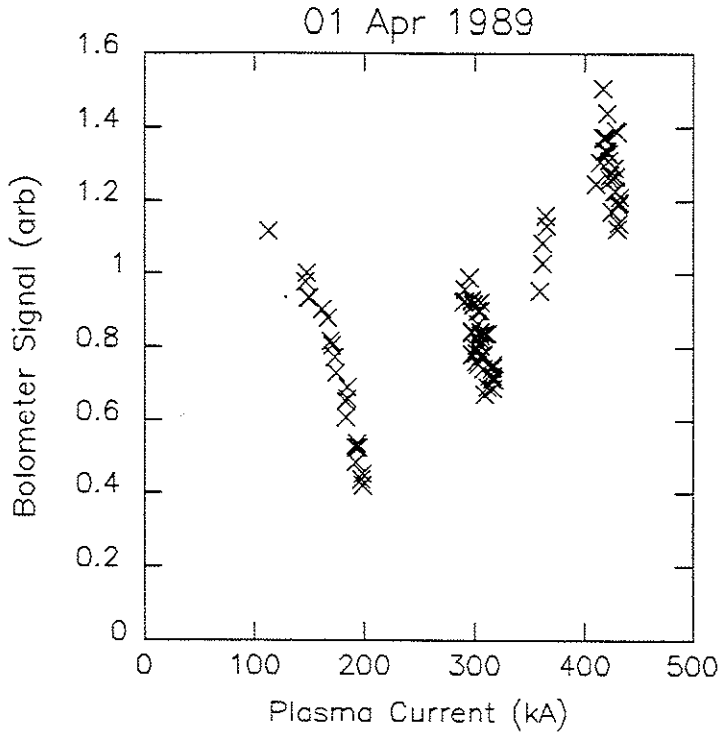


Figure VI.83: Bolometer signal versus $I_p$ from plasma current scan series.

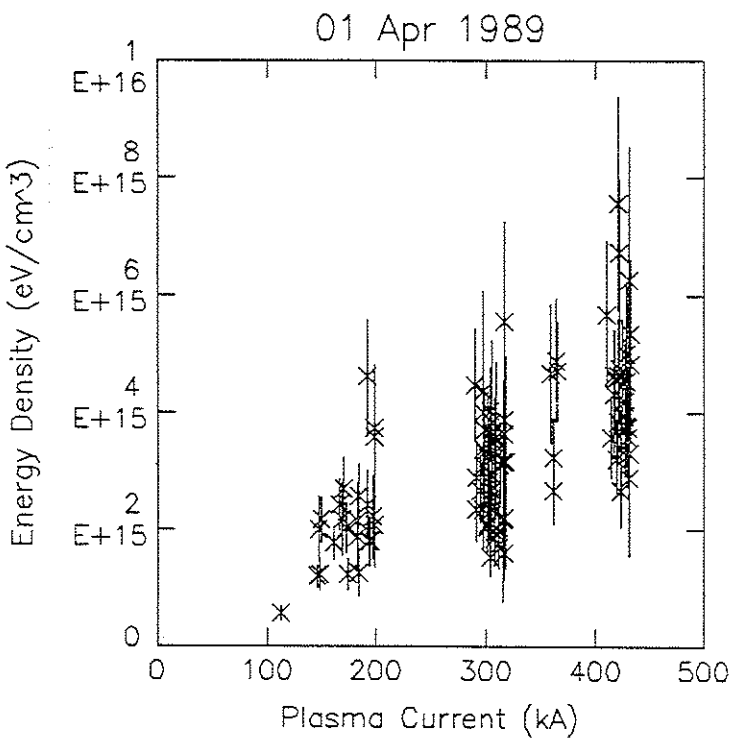


Figure VI.84: Central $n_e T_e$ product versus $I_p$ from plasma current scan series.



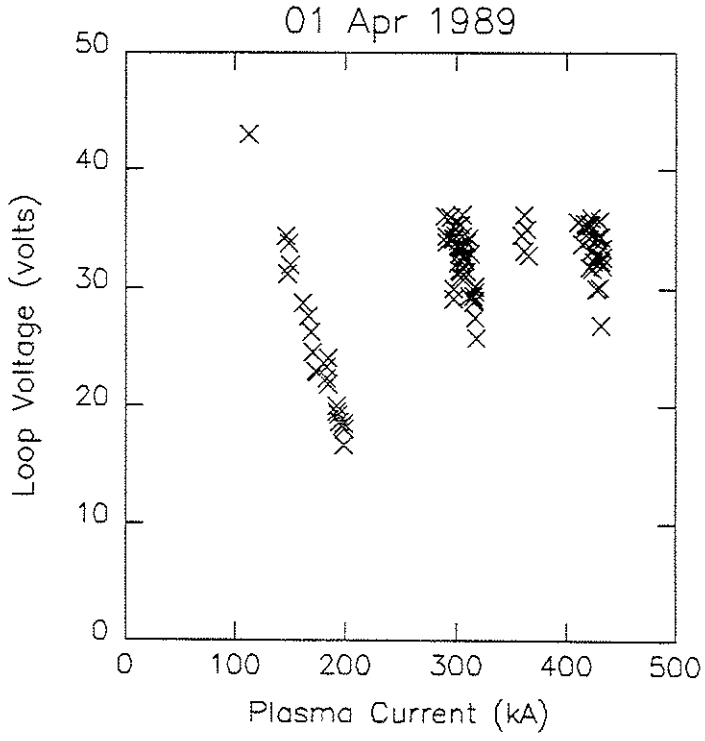


Figure VI.85: $V_\ell$ versus $I_p$ from plasma current scan series.

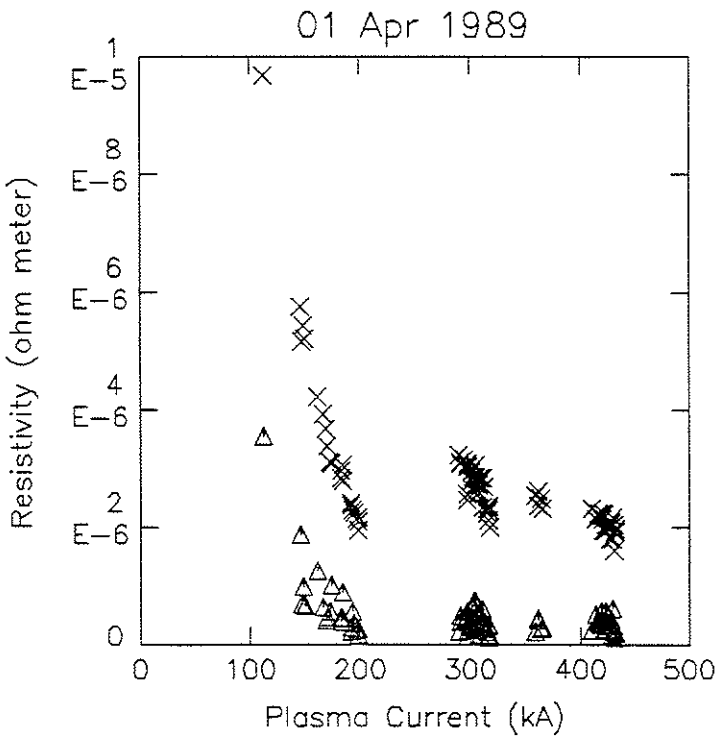


Figure VI.86: Measured parallel resistivity $\eta^*$ (cross symbols) and Spitzer resistivity $\eta_{sp}$ (triangle symbols) versus $I_p$ from plasma current scan series.



# CHAPTER VII: SUMMARY

A Thomson scattering diagnostic has been constructed and used on MST to measure central electron temperature and density during the plasma current peak. Data from this diagnostic has been used to compare the behavior of MST to that of other RFP devices and to study the processes and mechanisms that determine the energy confinement of MST.

Thomson scattering of electromagnetic radiation is, per se, a relatively simple physical process. However, as elsewhere, ease of comprehension does not imply ease of practical implementation. The small size of the Thomson scattering cross section places fundamental limits on the performance of the Thomson scattering diagnostic. Photon statistics dominate the uncertainties of the measurements made with the MST diagnostic.

The Thomson scattering diagnostic is a set of optical and electronic subsystems, each of which has been described in this thesis. Successful operation of this diagnostic requires care and attention to detail. Each subsystem must function almost perfectly if the diagnostic is to provide meaningful data. The alignment and calibration procedures described in this thesis must be thoroughly understood by the operator of this diagnostic. At best, operational shortcuts

lead to meaningless data; usually they result in destruction of some component of the diagnostic system.

During much of the time period this diagnostic was operational on MST it was calibrated to provide absolute measurements of the central electron density. This capability, when combined with profile and other assumptions, allowed calibration of poloidal beta ($\beta_\theta$) and energy confinement time ($\tau_E$). A standard MST discharge with $I_p \approx 400$ kA, $F \approx -0.1$, and $\theta \approx 1.6$ typically exhibited $T_e \approx 275$ eV, $n_e \approx 2.0 \times 10^{13}$ cm$^{-3}$, $\tau_E \leq 1$ ms, and $\beta_\theta \leq 8\%$. MST is indeed a high beta device, but, as in all RFP devices, $\tau_E$ is at least an order of magnitude less than that predicted by classical ion thermal conduction. The limited current scaling studies done on MST suggest that neither $\tau_E$ nor $T_e$ scale in a strong positive fashion with $I_p$. This result may be modified during future operation of MST. The typical "best results" from an RFP device usually come after several years of optimization. Performance of MST with optimized poloidal field windings may substantially improve these results.

The processes responsible for the enhanced energy loss rate of the RFP have not yet been pinpointed, but, within the context of this thesis, the important energy loss channels on MST appear to be



a) thermal transport from stochastic magnetic fields

b) escape of particles from the plasma

c) radiative energy loss

c) an unknown energy loss channel or channels.

This conclusion is indicated by an internally consistent analysis of the results from an F-scan experiment, a paddle limiter insertion experiment, and an argon doping experiment. Application of these perturbations resulted in separable and reversible changes in the plasma energy loss channels. The success of this technique is proportional to the extent to which these changes are monitored. Further development of such diagnostics as a time-resolved bolometer, edge electron energy analyzer, and a charge exchange analyzer should improve knowledge of the means whereby energy leaves the MST plasma. The composition of the particle loss channel is one of the points yet to be resolved.

One of the keys to an explanation of the energy confinement behavior of MST may lie in the observation of a nearly constant poloidal beta during the perturbation experiments. Poloidal beta was constant because $n_e$, $T_e$, and $I_p$ were all individually constant. The results seem to suggest that manipulation of the energy loss rate from one of the energy loss channels results in compensatory changes in

the other loss channels and in power flowing into the plasma, all with result that a constant $\beta_\theta$ is maintained.

Finally, one of the intriguing mysteries yet to be fully investigated is the behavior of the bulk $T_e$ and $n_e$ during a sawtooth-like oscillation. Results from MST indicate that even though the soft x-ray signal (which is presumably generated by energetic tail electrons) is strongly modulated during an oscillation, the bulk $T_e$ and $n_e$ vary only slightly, if at all. Although we know that global energy confinement does degrade during an oscillation, we do not know what role, if any, these suprathermal electrons play in determining confinement and/or the loop voltage of the RFP. In particular, perhaps control or modulation of these suprathermal electrons by operation at the high density limit (low $I_p/N$) may enhance confinement. This is, of course, only one of many questions that needs to be resolved. The energy confinement of the RFP may be intrinsically anomalous and not suitable for a fusion device. However, such a possibility should serve not to discourage research on the RFP, but should spur a desire to understand the physical mechanisms that determine the energy confinement of the RFP.